# Highly Efficient MeO Nanoparticles as Curing Activator for Rubber Composites

Susanna Antonio

XXVIII cycle

Matricola 775134

Tutor Scotti Roberto

**Table of contents**

**Chapter 1: Introduction and aim of the thesis** **1**

1.1. Aim of the thesis 6

1.2. Structure of the thesis 7

**Chapter 2: Nanocomposite vulcanization** **12**

2.1. Historical background 13

2.2.Vulcanization 15

2.2.1. Vulcanization Introduction 15

2.2.2. Vulcanization mechanism 18

2.2.3. Analysis of vulcanized rubber 24

2.3. Silica filler 26

**Chapter 3: Synthesis and characterization of ZnO/$SiO_2$ NPs** **32**

3.1. Sol-gel synthesis of nanostructures 35

3.2.1. Reactants and materials 35

3.2.2. Synthesis procedure 35

3.2.2. Synthesis procedure 35

3.3. Morphological and Structural Characterization of ZnO/$SiO_2$ 37

3.3.1 X-ray Diffraction (XRD) 37

3.3.2 Transmission Electron Microscopy (TEM) 38

3.3.3 UV-Vis analysis 39

3.3.4 Attenuated Total Reflection-Fourier Transform Infrared Spectroscopy (ATR-FTIR) analysis 43

3.3.5. $^{29}$Si MAS, $^{29}$Si CP MAS and $^{1}$H MAS NMR analysis 44

3.3.6 X-ray Photoelectron Spectroscopy (XPS) 50

3.4. Conclusions 53

**Chapter 4: New insights into the catalytic activity of silica anchored ZnO nanoparticles in rubber vulcanization 56**
4.2. Preparation of silica/IR nanocomposites 57
4.2.1. Materials 57
4.2.2. Compounding and vulcanization of silica IR nanocomposites 58
4.3. Results and Discussion 59
4.3.1. Vulcanization of silica IR nanocomposites 59
4.3.2. Cross-linking density of the YZO-IR and M-YZO-IR composite 62
4.3.3. Apparent Activation Energy of curing process from Differential Thermal Analysis 63
4.3.4 Model compound vulcanization 66
4.3.5 FTIR analysis 73
4.4. Conclusions 78

**Chapter 5: Synthesis and characterization of MeO/$SiO_2$ NPs as vulcanization agent in the nanocomposite 81**
5.1. Metal oxides as activator for the rubber vulcanization 82
5.2. Synthesis of CaO and MgO nanoparticles 85
5.3. Preparation of CaO/$SiO_2$ and MgO/$SiO_2$ 88
5.3.1. Reactants and materials 88
5.3.2. Synthesis procedure 88
5.4. Morphological and structural characterization of CaO/$SiO_2$ and MgO/$SiO_2$ 89
5.4.1 Thermogravimetic analysis (TGA) 90
5.4.2. Structural analysis of CSO-X and MSO-8 92
5.4.3. Si-O-Me characterization by ATR-FTIR 93

5.3. Mechanical characterization of the CSO-X/IR and MSO-8/IR nanocomposite 96
5.3.2. Cross-linking density 100
5.4 Model compound vulcanization 101
5.5. Morphological and structural characterization of the CaO NPs 103
5.5.1. Mechanical characterization of the CaO-X/IR nanocomposite 105
5.6. Conclusions 107

**Appendix A: Characterization and Methods 114**
A.1.1. Silica synthesis, state of art 115
A.2.1. Inductively Coupled Plasma (ICP) 116
A.2.2. High-Resolution Transmission Electron Microscopy (HRTEM) 117
A.2.3. X-ray Diffraction (XRD) 119
A.2.4. Reflectance UV–Visible analysis 120
A.2.5. Attenuated Total Reflectance Fourier Transform Infrafed Spectroscopy (ATR-FTIR) 120
A.2.6. Nuclear Magnetic Resonance (NMR) 122
A.2.7. X-ray Photoelectron Spectroscopy (XPS) 123
A.2.8. Thermogravimetirc analysis (TGA) 124
A.2.9. Apparent Activation Energy of curing process from Differential Thermal Analysis 125
A.2.10. The Liquid Chromatography-Mass Spectroscopy (LC/MS) 127
A.3.1. Model compound vulcanization 128
A.4.1. Swelling experiments 128
A.4.2. Moving Die Rheometry (MDR) and curing kinetics 129

# Chapter 1

# Introduction and aim of thesis

The rubbers are fundamental materials largely used in many applications of our everyday life, such as shoes, tyre, pipes. However, for most of these applications their physico-mechanical properties are not sufficient and they need to be reinforced by curing process and by introducing stiff filler nanoparticles (NPs) in the rubber matrix.

The sulfur vulcanization is the most used chemical process in the tyre technology to improve the mechanical properties of unsaturated rubber (e.g. elasticity, tensile strength, abrasion) by a crosslinked polymeric network.

Despite the rubber vulcanization process is known since 1839 and it has been largely used for many years in large scale industrial technological applications, it remains, even today, object of studies and controversies due to the complexity of the system, where many reactions between polymer and curing agents take place simultaneously, consecutively and to the difficulty using common spectroscopic and analytic techniques directly in rubber matrix and in operating conditions [1]. In this contest one of the most important goal in the tyre technology result to achieve a desiderate polymer network structure and distribution through the control of the sulfur crosslinking reactions, so to improve the tyre performance and reduce the energy consumption due to the hysteretic effect of the rolling tyre on the road, that produce an increase of the CO, $NO_x$, $CO_2$ emission to atmosphere [2].

Thus, it appears mandatory to further investigate at molecular level the structure of the intermediate compounds during the sulfur crosslink reactions. Several authors have studied the curing mechanism by different approaches, kinetic [3, 4], thermodynamic [5-7], mechanic [1, 8] and spectroscopic [9-11] in order to find a relation between the steps of

the complex vulcanization process and the chemical structures and physical proprieties of the cured rubber material.

In general it is desirable to enhance the vulcanization rate in order to decrease time and energy used [4, 3, 5]. Over the years different additives acting as accelerators [6] or activators [7, 8] have been employed.

Nowadays there is a good evidence that zinc plays an important role in the curing efficiency, crosslinking, and in the ultimate mechanical proprieties of the composite [12, 13]. Microcrystalline ZnO particles are commonly employed in curing processes, associated with fatty acid, as the stearic acid. Many authors suggested that Zn(II) centers, produced by ZnO interaction with stearic acid, form organometallic derivatives with the accelerator molecules, a class of organic compounds which includes thiurams, dithiocarbamtes, sulfonamides, thiazoles and guanidine [8, 14]. This leads to the formation, with the addition of sulfur, of the so called active sulfurating species, a complex able to form polysulphidic chainsbinding rubber chains [15].

It well know that the lengths of the sulfur bridges are strongly influenced by the kind of curing system. In particular, sulfur bridge length distribution, crosslinking density and *macro*-sulfur network distribution are influenced by the availability of $Zn^{2+}$ ions to form the active complexes in the first part of the curing process [15]. This is the key point of the activation mechanism and strongly depends on the ZnO dispersion in the polymer matrix and on the crystal structure of the metal oxide.

The ability of the $Zn^{2+}$ ion to be a metal center for many catalyst complexes has led this metal to be used in many fields, chemistry, biology, medicine and engineering [16-18]. Anyway, the tyre is main

responsible of zinc dispersion in the environment, despite the amount of zinc oxide used into a tyre compared to other ingredients remains low, between 2-5 phr (part per hundred rubber), but the use of microcrystalline ZnO in the tyre industry still today remain too much elevate. The tyres productions are in constant increase and it was estimated that in 2016 the number of tyres present in the world will be so high that lining up the tyres, it will be possible covering 1,5 times the earth circumference and in 6,5 years the distance between earth and moon [19].

The tyre wear produced 285.000 tons of zinc in the USA highway between 1936 and 1999, just in 1999 around 10.000 tons was released in the USA highway for tyres abrasion. The tyre wear is particularly relevant in urban areas with values 10 times higher than in rural zones. In South San Francisco Bay approximately 60% of the total load of Zn was estimated to derive from tyre [20, 21] .

The ZnO by anthropic origins has reached so high level to be a serious problem of toxicity for the aquatic organisms. The maximum permissible concentration of Zn in water has been set by Environmental Protection Agency (EPA) at 120 µg/L [22]. The European Parliament has legislated the decrease of zinc oxide content within the tyre, opening an urgent task in the tyre research.

The problem can be solved by the total substitution or by reduction of ZnO in curing process but this aspect strongly weights on the vulcanization efficiency and therefore it request research efforts in finding alternative solutions

The problem of the use of ZnO in tyre production is not just related to these environmental issues. Even if largely employed in the production, ZnO gives problems during the mixing process, due its high polarity

which provokes migration phenomena into the unpolar rubber matrix with the formation of not dissolved ZnO clusters. Thus ZnO cannot completely react with the other curing agents, producing not homogeneous vulcanization and different concentration of cured polymer in the matrix, leading to undesired dishomogeneity and poor reproducibility of the composite materials.

Different approaches have been proposed to face this challenge. Among them the use of ZnO NPs has recently received a great deal of interest because of the better dispersion in rubber and the increased of the mechanical proprieties due to their high surface-to-volume ratio [23, 24]. However, the large-scale synthesis of pure ZnO in the form of homogeneous and well dispersed spherical NPs is difficult due to the tendency of this oxide to crystallize in hexagonal phase, growing along selective crystal planes and giving anisotropic crystals [25]. Moreover ZnO NPs generally undergo high growth rate and Ostwald ripening phenomena that increase the particles size, distribution and dishomogeneity.

Many different methods (e.g. solvothermal, hot-injection, miniemulsion) have been proposed to obtain ZnO NPs. However, the morphological control is not always really good and some of these techniques are at high cost, complexes and only sub-gram can be obtained [26].

Possible approaches give the possibility to decrease the amount of metal oxide by the synthesis of nanoparticles metal oxide supported on other metal oxide, with approach has been used with success in different fields of the catalytic chemistry but not yet employed in the vulcanization system in tyre manufactory [27, 28].

Another approach to substitute ZnO as curing accelerator is the use of other metal inorganic activators. Recently has received more interest the

alkaline earth metals, e.g. MgO, CaO, for their large availability low cost and environmental safety. The magnesium (II) and calcium (II) has been already studied as accelerator in the curing process, with good results about their ability to speed up the curing kinetic [29]. Anyway, it is still not clear their ability to form active complex with accelerators and increasing their efficiency.

### 1.1. Aim of the thesis

This study is aimed at investigating new routes for the reduction or the substitution of the amount of ZnO particles commonly used in the industrial curing procedures and at the same time to reach an enhancement of the curing efficiency.

The goal was obtained by using as curing accelerator a novel material constituted by ZnO nanoparticles (NPs) grown on silica filler particles. This allows to utilize $ZnO/SiO_2$ NPs as curing activator and simultaneously reinforcing filler for the rubber nanocomposite (Figure 1.1.).

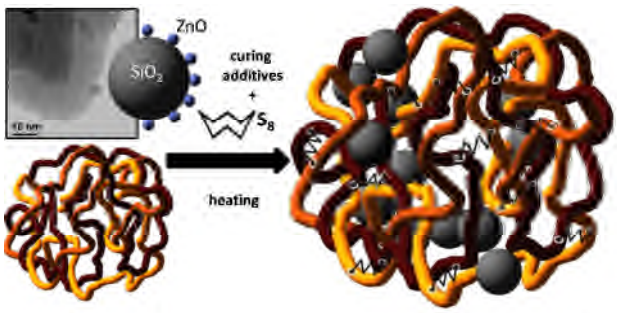


Figure 1.1. Schematic representation of the vulcanization process by $ZnO/SiO_2$ particle.

The focus is an improvement of the curing efficiency and the mechanical properties of the materials through a better control of the crosslink process.
In this thesis will be reported:

- the synthesis of $ZnO/SiO_2$ were synthesized by a novel low temperature sol-gel route based on the hydrolysis of zinc acetate in NaOH ethanol solution and condensation in the presence of silica NPs.

- a deep investigation of the $ZnO/SiO_2$ catalyst and the mechanism in the curing reaction, performed to have a better control of the vulcanization process.

This last objective was reached by the study of the catalytic activity of silica supported ZnO in the sulfur crosslinking of isoprene rubber (IR), particularly in the formation of the sulfuring complexes at the beginning of reaction and of the sulphur network in the final cured material.
Moreover, in a similar $ZnO/SiO_2$ system alkaline-earth metals oxide ($MeO/SiO_2$) were studied in comparison to a classical vulcanization approach.

### 1.2. Structure of the thesis

This thesis is divided into 6 chapters, as outlined:
In **Chapter II** the background on the vulcanization process, with the main focus on the ZnO role and the silica filler characteristics.
In **Chapter III** the preparation of $ZnO/SiO_2$ NPs by sol-gel synthesis with different loading of zinc was reported. The morphology and crystal structure of $ZnO/SiO_2$ NPs were investigated by X-ray Diffraction (XRD)

and Transmission Electron Microscopy (TEM). The nanometric size was assessed by UV reflectance measure, while the Si-O-Zn bond interaction was studied by Solid State Nuclear Magnetic Resonance (NMR), Attenuated Total Reflection-Fourier Transform Infrared Spectroscopy (ATR-FTIR) and X-ray Photoelectron Spectroscopy (XPS) and discussed in relation to the NPs dimensions.

In **Chapter IV** offer a study comparative on behavior and the curing efficiency, dynamic mechanical properties of the nanocomposites vulcanized with $ZnO/SiO_2$ and those obtained by a composite prepared using a conventional microcrystalline ZnO as activator of vulcanization.

The mechanical proprieties were evaluated by dynamic mechanical properties DMA and swelling measurements on the cross-linking density. The curing efficiency of the catalysts being evaluated by apparent activation energy of the different steps in the process, using a kinetic approach at non-isothermal conditions and employing Differential Scanning Calorimetric (DSC) measurements.

The structure of the reaction intermediates in the vulcanization process were investigated by using the Model Compound Vulcanization (MCV) methods and the cured compounds analyzed by Liquid Chromatography – Mass Spectroscopy (LC-MS) chromatography and $^1$H-Nuclear Magnetic Resonance ($^1$H-NMR) spectroscopy. The comparison between the two catalysts have been also discussed on the basis of Fourier-Transform Infrared Spectroscopy (FTIR) investigation.

In **Chapter V** the preparation of activator/filler system, where the ZnO was replaced by MgO and CaO ($MeO/SiO_2$) was described. The $MeO/SiO_2$ was characterized by thermogravimetric analysis (TGA) and the crystallinity analyzed by XRD. The chemical interaction Si-O-Me was investigated by FTIR.

The curing efficiency of the $MeO/SiO_2$ was evaluated by dynamic mechanical proprieties, cross-linking density measurements and MCV then compared respect to system with unsupported crystalline oxides.

The thesis is completed with a general evaluation of the results in: **Chapter VI**.

---

[1] Y. Coran, Eirich, F.R. (Ed.) Science and Technology of rubber, Academic Press, New York Chapter 7 (1978).

[2] H. Hirata, H. Kondo, Y. Ozawa, In Chemistry, Manufacture and Applications of Natural Rubber, Woodhead Publishing: Oxford (2014) 325.

[3] R. Ding, A.I. Leonov, A.Y. Coran, A Study of the Vulcanization Kinetics of an Accelerated-Sulfur SBR Compound, Rubber Chem. Technol. 69 (1996) 81-91.

[4] A.I. Isayev, J.S. Deng, Nonisothermal Vulcanization of Rubber Compounds, Rubber Chem. Technol. 61 (1988) 340-361.

[5] A.P. Mathew, S. Packirisamy, S. Thomas, Studies on the thermal stability of natural rubber/polystyrene interpenetrating polymer networks: thermogravimetric analysis, Polym. Degrad. Stab. 72 (2001) 423-439.

[6] M. Tiwari, J.W.M. Noordermeer, W.K. Dierkes, W.J. van Ooij, Effect of Plasma Polymerization on the Performance of Silica in NBR, EPDM and NBR/EPDM Blends, Rubber Chem. Technol. 81 (2008) 276-296.

[7] N.J. Morrison, M. Porter, Temperature Effects on the Stability of Intermediates and Crosslinks in Sulfur Vulcanization, Rubber Chem. Technol. 57 (1984) 63-85.

[8] A.Y. Coran, Vulcanization. Part V. The Formation of Crosslinks in the System: Natural Rubber-Sulfur-MBT-Zinc Ion, Rubber Chem. Technol. 37 (1964) 679-688.

[9] Y. Ikeda, N. Higashitani, K. Hijikata, Y. Kokubo, Y. Morita, M. Shibayama, N. Osaka, T. Suzuki, H. Endo, S. Kohjiya, Vulcanization: New Focus on a Traditional Technology by Small-Angle Neutron Scattering, Macromol. 42 (2009) 2741-2748.

[10] K. Fujimoto, K. Wataya, The study of polymers by high-temperature ATR spectroscopy, J. Appl. Polym. Sci. 13 (1969) 2513-2526.

[11] J. H. M. Van den Berg, J. W. Beulen, E. F. J. Duynstee, H. L. Nelissen, Model Vulcanization of EPDM Compounds—Part I: Structure Determination of Vulcanization Products from Ethylidene Norbornane, Rubber Chem. Technol. 57 (1984) 265-274.

[12] L. G. Hernandez , A. R. Diaz , J. L. de Benito Gonzales, I. F. Orosa , A. M. Fernandez, Effects of the structure and crosslink distribution on the physical properties of a natural rubber network: Comparison of sulfur, peroxide and benzene-1,3-disulfonylazide crosslinking systems, Kautschuk Gummi Kunststoffe 45 (1992) 1033–1037.
[13] T. A. Vilgis, G. Heinrich, New aspects in rubber elasticity: A challenge for theoretical physics and applied materials sciences, Kautschuk Gummi Kunststoffe 45 (1992) 1006–1014.
[14] Coran, A.Y. Coran, Chemistry of the vulcanization and protection of elastomers: A review of the achievements, J. Appl. Polym. Sci. 87 (2003) 24-30.
[15] Y. Ikeda, Y. Yasuda, T. Ohashi, H. Yokohama, S. Minoda, H. Kobayashi, T. Honma, Dinuclear Bridging Bidentate Zinc/Stearate Complex in Sulfur Cross-Linking of Rubber, Macromol. 48 (2015) 462-475.
[16] D. Endy, Foundations for engineering biology, Nature 438 (2005) 449-453.
[17] A.V. Kachynski, A.N. Kuzmin, M. Nyk, I. Roy, P.N. Prasad, Zinc Oxide Nanocrystals for Nonresonant Nonlinear Optical Microscopy in Biology and Medicine, The Journal of Physical Chemistry C 112 (2008) 10721-10724.
[18] M.L. Maeder, S. Thibodeau-Beganny, A. Osiak, D.A. Wright, R.M. Anthony, M. Eichtinger, T. Jiang, J.E. Foley, R.J. Winfrey, J.A. Townsend, E. Unger-Wallace, J.D. Sander, F. Müller-Lerch, F. Fu, J. Pearlberg, C. Göbel, Justin P. Dassie, S.M. Pruett-Miller, M.H. Porteus, D.C. Sgroi, A.J. Iafrate, D. Dobbs, P.B. McCray Jr, T. Cathomen, D.F. Voytas, J.K. Joung, Rapid "Open-Source" Engineering of Customized Zinc-Finger Nucleases for Highly Efficient Gene Modification, Molecular Cell 31 (2008) 294-301.
[19] V. Herrmann, A. Schulz, Würzburg, The Effect of Recycled Rubber as an Additive for Vulcanisates, International Rubber Conference, Nuremberg (2015).
[20] T.B. Councell, K.U. Duckenfield, E.R. Landa, E. Callender, Tire-Wear Particles as a Source of Zinc to the Environment, Environmental Science & Technology 38 (2004) 4206-4214.
[21] D. Hjortenkrans, G. Bergbäck, V. Agneta, Metal Emissions from Brake Linings and Tires: Case Studies of Stockholm, Sweden 1995/1998 and 2005, Environmental Science & Technology 15 5224-5230.
[22] A.G. Heath, Water pollution and fish physiology, Lewis Publishers, Boca Raton :, 1995.
[23] S. Sahoo, M. Maiti, A. Ganguly, J. J. George, A. K. Bhowmick, Effect of zinc oxide nanoparticles as cure activator on the properites of natural rubber and nitrile rubbe, J. Appl. Polym. Sci. 105 (2007) 2407-2415.
[24] G. Heideman, R.N. Datta, J.W.M. Noordermeer, B.v. Baarle, Influence of zinc oxide during different stages of sulfur vulcanization. Elucidated by model compound studies, J. Appl. Polym. Sci. 95 (2005) 1388-1404.
[25] Y. Chen, M. Kim, G. Lian, M.B. Johnson, X. Peng, Side Reactions in Controlling the Quality, Yield, and Stability of High Quality Colloidal

Nanocrystals, Journal of the American Chemical Society 127 (2005) 13331-13337.
[26] D. Chen, X. Jiao, G. Cheng, Hydrothermal synthesis of zinc oxide powders with different morphologies, Solid State Communications 113 (1999) 363-366.
[27] C. Cannas, M. Casu, A. Lai, A. Musinu, G. Piccaluga, XRD, TEM and 29Si MAS NMR study of sol-gel ZnO-SiO2 nanocomposites, Journal of Materials Chemistry 9 (1999) 1765-1769.
[28] S. Panigrahi, D. Basak, ZnO–SiO2 core–shell nanorod composite: Microstructure, emission and photoconductivity properties, Chemical Physics Letters 511 (2011) 91-96.
[29] V. Ducháček, A. Kuta, P. Přibyl, Efficiency of metal activators of accelerated sulfur vulcanization, J. Appl. Polym. Sci. 47 (1993) 743-746.

# Chapter 2

# Nanocomposite vulcanization

## 2.1. Historical background

The story of the rubber starts between the 6th and 8th centuries when the Aztec population called Cahuchu ("weeping wood") a white fluid extracted from particular trees of the tropical forests. The first notices of this fluid arrived in Europe after the travels of the Italian navigator Cristoforo Colombo and the discovery of the "new world". Returning from his second travel, he reported that the natives of these regions played with "elastic" balls.

The name "rubber" has been introduced just in 1770 when Joseph Priestly accidentally discovered that a piece of caoutchouc is able to erase the pencil's marks [1].

In 1838 Hayward patented a process in which natural rubber mixed with elemental sulfur was exposed to sunlight to obtain a materials with non sticky surface [2]. A year later the American Charles Goodyear noted that natural rubber, sulfur, white lead and oil of turpentine, placed on hot stove, changed its proprieties, becoming an elastic and non-sticky materials. This was the birth of the so called vulcanization (from the pagan roman god of fire, Vulcan) [3]. Goodyears immediately understood the relevance of this process and decided to publish his patent in 1842. The Patent of Charles Goodyear is a method to prevent the stickiness and the low temperature brittleness of the waterproof. It was a very slow process that took many hours to vulcanize. Here below is reported how Charles Goodyear prepared the curing process for rubber:

…..”I take twenty-five parts of india-rubber, five parts of sulfur, and seven parts of white lead… …..the goods are to be subjected to the action of a high degree of temperature, …… for the best effect approaching as nearly as may be to 270 °*Fahrenheit*”…

Patent No. 3,633, dated June 15, 1844

In the same period, the English engineer Tomas Hancock invented a process of mastication of the raw rubber, which permitted to shred the blocks of rubber making them more usable. When he received a piece of Goodyear's vulcanizated rubber, he immediately recognized its importance and he submitted a British patent in 1843 [4].

Some years later, in 1845, R. W. Thompson filed the first patent for a pneumatic tyre constituted mainly of simple tubes [5].

The consumption of caoutchouc started to rise quickly and already in 1856 reach 7000 tons for year. Many societies began to be founded; one of first company was the Italian Pirelli in 1872 in Milan.

The efforts to reach an increase in the vulcanization efficiency started to multiply. In 1881 Rowley observed the acceleration effect of ammonia on the sulfur vulcanization in the natural rubber [6], but this process didn't become popular due the difficulty in using this method. This opened a series of researches focused on new kinds of accelerators, organic molecules able to speed up the slow vulcanization process performed only by sulfur. In 1920 Molony first applied an ultra-accelerator in a compound using the tetramethylthiuram disulfide (TMTD) [7] (figure 2.1. a.).

A further improvement in the vulcanization performance was reached with the introduction of N-cyclohexyl-2-benzothiazole sulfonamide (CBS) (figure 2.1. b.). It resolved most of the problems connected to the TMTD, in particular the problem of toxicity.

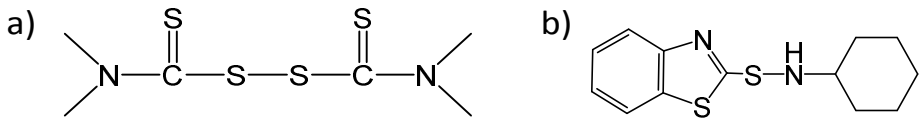


Figure 2.1. a) tetramethylthiuram disulfide (TMTD) and b) N-cyclohexyl-2-benzothiazole sulfonamide (CBS).

Goodyear's original vulcanizated mixing consist in sulfur with lead carbonate, but just at the beginning of 19th century was substituted with lead and zinc oxide. Typically the formulation contained high amount of ZnO (30 phr) as reported by S. B. Molony in 1919 and Norris in 1930 [8], mainly used as filler for its good mechanical propriety and anti-damping effect. However, in the same period, zinc organic complex started to be used as activator in the rubber curing. In 1921, M. M. Harrison published a patent where he experimentally proved that the accelerator worked better in the presence of ZnO (2 %wt) and stearic acid, improving the curing efficiency of the system [9].

## 2.2. Vulcanization

### 2.2.1. Vulcanization introduction

The tyre industries has been always focused on find in new materials and methods able to increase the curing efficiency and reach high mechanical properties of tyre (elasticity, tear resistance, rolling resistance, mileage, wear resistance, anti-ageing etc.).

The study of the vulcanization chemistry has a central position in the research field of the composite in order to obtain better performances by optimization of the curing process, that assumes key role to increase the ultimate mechanical proprieties [10].

In the last years, it has assumed more relevance the decrease of the rolling resistance, without loss of other proprieties as wet grip and wear resistance. The rolling resistance is due to the force resisting to the motion of the tyre on the road, associated to the tyre deformation during the rolling. This produces energy dissipation in the form of heat (hysteresis), responsible of the consumption of the fuel as well as of the tread-wear. It was estimated that 3-4% fuel can be saved with a reduction of rolling resistance of the 20 % [11].

To reach these objectives, the research efforts are focused both on the new curatives able to improve the desired composite properties and on the control of the curing process through a deeper knowledge of the sulfur vulcanization mechanism.

In the curing process, elementary sulfur or sulfur donors added to the double bonds of the polymer leads to the formation of junctions between the rubber chains (cross-linking).

The cross-links can be poly- di- or monosulphides, and depends both from the curing agents and parameters used.

For an effective vulcanization, the desired crosslinking is intermolecular (figure 2.2) (between different polymer chains) without intramolecular links, with polysulfide chain, $-S_y-$ bound to the some polymer).

The different length on the sulphide chains give different properties due to the different bond energy (table 2.1) [12]. The polysulphidic crosslinks are more flexible and less stable at high temperature then mono and disulphidic corsslinks. The low stability of polysulphidic crosslinks at high temperature or for long curing time causes desulfuration reactions, the breakdown of the polysulphidic bridge and the recombination to form

shorter cross-links and pendent groups dangling from the rubber coil [13].

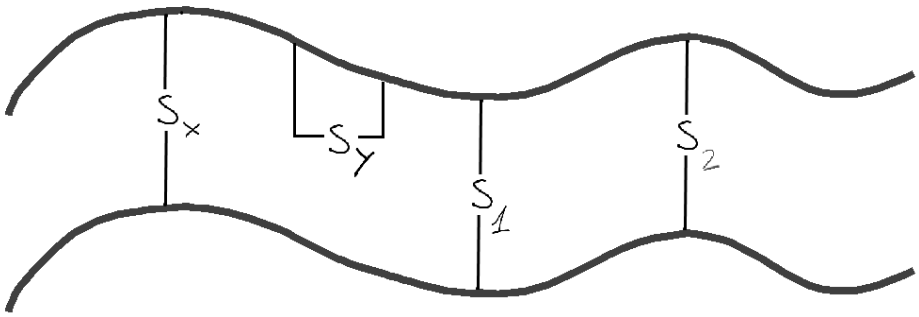


Figure 2.2. sulfur crosslinking representation between rubber coils.

| **Crosslinking type** | **Bond energy (kJ/mole)** |
|---|---|
| **-C-$S_x$-C- (x>2)** | < 268 |
| **-C-$S_2$-C-** | 268 |
| **-C-S-C-** | 285 |
| **-C-C-** | 352 |

Table 2.1. Crosslinking type and the corresponding bond energy [14].

Thus, the type of crosslinking formed largely depend on the vulcanizated system:

1. amount of reagents
2. reactivity of reagents
3. reaction time/temperature

The control of the network structure during the vulcanization is fundamental to obtain the appropriate mechanical proprieties, as friction coefficient, tear strength and a strong decrease of the hysteresis.

### 2.2.2. Vulcanization mechanism

The vulcanization mechanism has been object of studies for many years and still today remains a significant scientific challenge. Modern techniques and advanced models have allowed many progress in the knowledge of the vulcanization but a fundamental understanding is far to be complete.

The vulcanization mechanism depends on the nature of the system employed. Both polar and radical mechanisms have been proposed for unaccelerated sulfur mechanisms [15] and its depends on the kind of rubber [16]. One of the most generally accepted mechanism was proposed by M. J. Morrison and M. Porter (figure 2.3), for the widely used CBS accelerated sulfur vulcanization of isoprene rubber in the presence and without zinc oxide as activator of vulcanization.

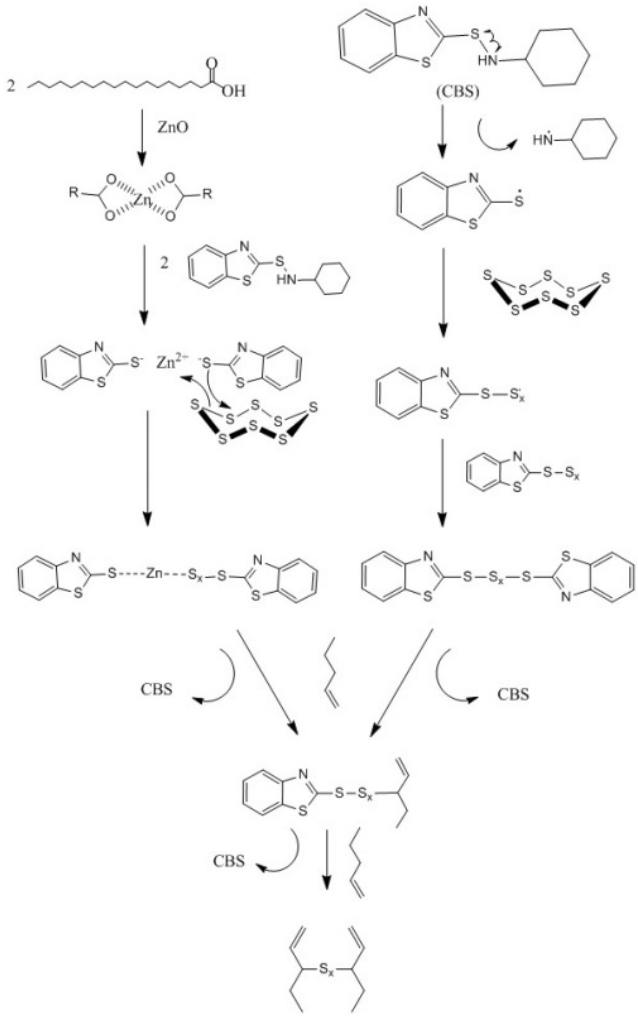


Figure 2.3. Vulcanization mechanism, in presence of ZnO (left) and in absence (right) proposed by M. J. Morrison and M. Porter [13]

Morrison and Porter divided the vulcanization reactions in three sub-categories:

*Precrosslinking reactions:*

There are several doubts about the real role of the ZnO in this first series of reactions. In figure 2.3 the different steps in the presence (left) or in the absence of ZnO (right) are shown. In the presence of ZnO, the

sequence of reactions were characterized by a fast kinetic of reactions and the formation of a series of organometallic complexes coordinated by Zn(II) center [17, 18].

The reaction starts with the metal oxide dissolution by the fatty acid, with the generation of a zinc distearate complex. This complex reacts with the accelerant CBS with the consequent breakdown of the sulfonamide bond to give another Zn(II) complex (see figure 2.4), more reactive than the free activator path [19]. The coordination of this complex with the accelerator is still not definitely clear. Different authors have advanced the hypothesis that the zinc ion complex can be stabilized by ligands, like the amines released from the sulfenamides or with carboxylates as chelates [13, 20, 21].

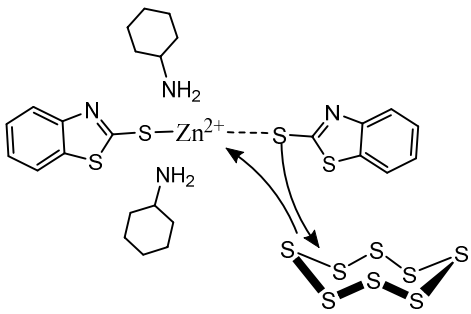


Figure 2.4. sulfurating agent in the presence of CBS as curing accelerator

Successively, the zinc complex forms another complex by opening the elementary sulfur ring and coordinating the polysulfide chains (figure 2.4). The new complex is the so called active sulfuranting agent. The coordination of elementary sulfur occurs more easily in the presence of $Zn^{2+}$ ion than with a radical/ionic process in the absence of ZnO where the accelerant was not completely released as active sulfuring agent.

There are still doubts about the structure of the benzothiazole-zinc-complex (figure 2.5), but the more probably was proposed in figure [13].

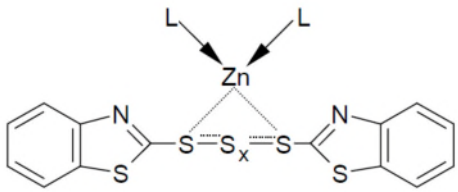


Figure 2.5. Structure of the benzothiazole-zinc-complex.

Several authors have underlined as these series of reactions happed on the surface of the bulk ZnO and it was characterized by a low efficiency of process with a not complete reaction of the ZnO, which remained partially not dissolved into the polymer matrix given origin to particle aggregation and dishomogeneity [22].

*Crosslinking reactions:*

This determining step leads to the formation of a bond between the intermediate complex and the rubber (figure 2.6). The reaction starts from the deprotonation of the rubber chain, in the allylic position, mainly in the position of the α-methyl groups adjacent to the double bonds, corresponding to the lowest deprotonation energy (table 2.2). Then the scission of polysulfide chains of the sulfuring complex occurs and the leaving group goes to bond directly to the rubber chain in the α-methyl group, leading to the formation of a polysulfide pendent group rubber-$S_y$-Accelerator, dangling from the rubber chain [23].

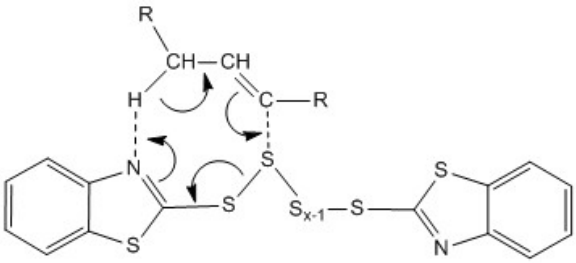


Figure 2.6. Deprotonation and sulfur crosslinks mechanism.

| Group | Deprotonation energy (kcal/mole) |
|---|---|
| **$CH_2CH$-H** | 110 |
| **$CH_3CH_2(CH_3)CH$-H** | 98 |
| **$CH_2CHCH_2$-H** | 89 |

Table 2.2. Molecular bond dissociation energies [24].

A similar scission mechanism of the active sulfurating species occurs also in the presence of $Zn^{2+}$ ions, with the breakdown of the polysulfide chains coordinated to the zinc cation. The presence of $Zn^{2+}$ increased the efficiency in the formation of the rubber bound intermediate, the process is further enforce by coordinative ammine groups of the complex, due to the increase of the nucleophilicity of the leaving sulfuranting complex.

This process prosecutes with a further crosslink precursor scissions (figure 2.7) with a breakdown of the rubber intermediate along the sulfur chain. The position of the chain break is also in this case influenced by the presence of $Zn^{2+}$ ion. Zinc cation improves the fragmentation of the long polysulfidic molecules leaving shorter sulfur chains dangling from the rubber (figure 2.7 right) compared to the process in the absence of zinc (figure 2.7 left) ($S_Z > S_X$ in figure 2.7) [25]. These reactions lead to

an enhancement of the crosslinking density and distribution, improving the efficiency of the curing process.

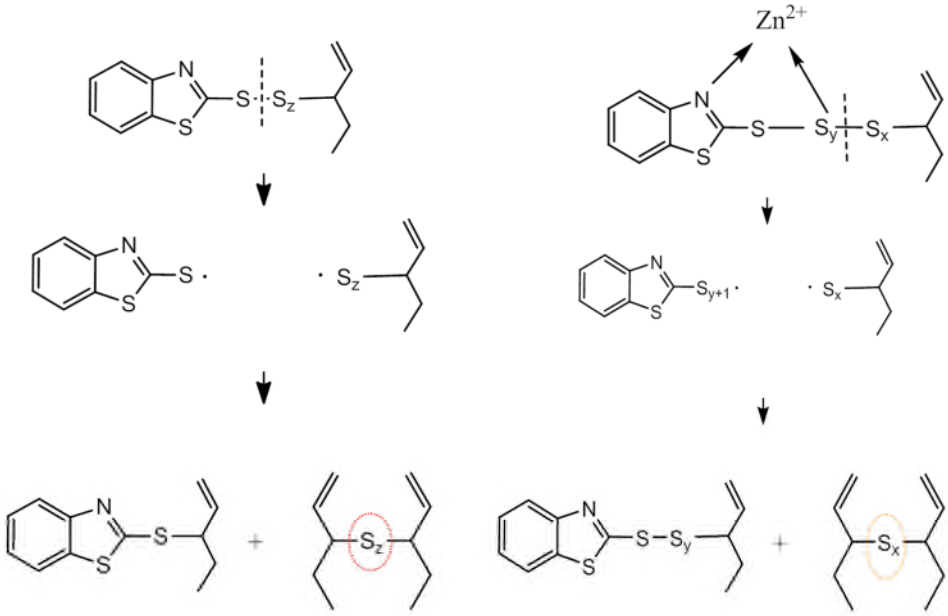


Figure 2.7. Desulfuration mechanism in absence (left) and presence of ZnO (right).

In this step, the presence of fragments of accelerators, 2-mercaptobenzothiazole groups, can be also present as by product. These leaving groups are stabilized by resonance (figure 2.8) and derives from the allylic substitution reactions, where one rubber-$S_y$-Accelerator moiety reacts with one rubber chain, forming the a crosslink and a protonated accelerator fragment [26].

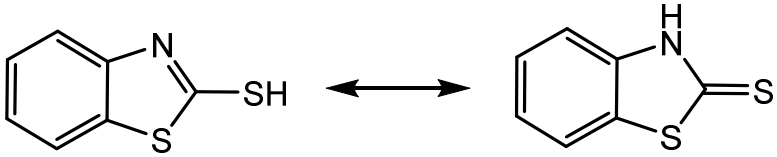


Figure 2.8. 2-mercaptobenzothiazole groups fragment.

*Post-crosslinking reactions*:

The crosslinking reactions are characterized by mono-, di- and polysulphidic chains, but also by sulphidic entanglement pendent from the rubber chains. This sulphidic entanglement is highly inefficient, characterized by low mechanical proprieties and high hysteresis. During the post-crosslinking phase there are a series of reactions leading the polysulphidic and Acc-$S_y$-rubber dangling groups of the network to shorter crosslinks.

Also in this step the presence of $Zn^{2+}$ ions favor these reactions. In fact, the link with the zinc decreases the electron density of the long polysulphidic chain favoring the scission of the chains, increasing the shorter crosslinking formation, and re-obtaining the active sulfuring agent which can give further crosslinks.

### 2.2.3. Analysis of vulcanized rubber

The analysis of viscoelastic material, characterized by low glass transition temperature and high molecular weight, it has been subject of study for many years by several authors and it is still under investigation. Today rehological devices, as oscillating disc rheometer (ODR), moving die rheometer (MDR) or rubber process analyser (RPA) are largely employed to measure the evolution of the crosslinking density as a function of time, in obtaining a sinusoidal curve called “curing curve”.

Others measures of the degree of vulcanization are obtained by swelling at the equilibrium according the Flory-Rhener equation [27].

However these methods are not capable to give reliable information on the network heterogeneity and structure at molecular level.

A deeper investigation on the chemical and physical proprieties cannot be obtained with a single technique due to the significant amount of compounds involved in the process: fillers, plasticizers, oils, curing agents, antioxidants. Moreover, the rubber is extremely viscous, sticky and at high molecular weight, thus not easy to be investigated with many common analytical and spectroscopic methods.

Anyway, the combination of different analysis approaches and the constant technological progress have demonstrated the possibility to give an interpretation to several reactions that enter in the complex vulcanization mechanism.

Kinetic, thermodynamic, macroscopic techniques and methods provide information on molecular level have been taken in consideration [23, 28].

Some authors have studied the curing process *in-situ* the polymer by spectroscopies techniques (photoacustic FT-IR, ATR-FTIR, synchrotron by small angle scattering technique, EPR, NMR relaxation technique and NMR imaging) offer a valid support to the mechanical technique by the individualization of the network structures [20, 22, 29]. In this field great consideration has achieved the Differential Scanning Calorimetric (DSC) that offer a precise analysis on the vulcanization process, thanks the possibility to make an accurate investigation on the kinetic problems also in case of complex reaction system being able to analyze the different steps of the reactions [30].

Other different approaches involve the use of model system. This method has been developed in the course of decade and has received more

interest for the possibility to substitute rubber, difficult to analyses for its high viscosity and molecule weight, with model systems. The model compound vulcanization (MCV) consist in a series of low weight molecules, easily analyzable with the spectroscopy techniques, that offer a crosslinking mechanism comparable with the high molecular weight polymers used in the tyre industries [31].

### 2.3. Silica filler

The first used of silica in rubber was in 1950, with an aluminum silicate, but just in 1992 born the "green tyre" with the used of silica nanoparticles (Appendix A.1.1. reports the synthesis) as active filler in the tyre. The process was developed by Michelin tyre, they provided the use of a special kind molecules able to bounding the silica with the rubber, for this reason it was called coupling agent (compatibilizer). The use of silica filler as substituted of carbon black started to increase, today the use of silica as filler within tyre is the biggest market that cover around 30 % of the world production [32]. The silica offer lower rolling resistance and higher wet performance than carbon black [33].

The silica has, furthermore, the possibility to be product with methods more cleans, given more sustainable production process, lower leaching in the environment and less problematic recycling.

The fillers used in the tyre industry are constitute from primary particles (cross sectional dimension of 5-100 nm) intra-linked by silosane covalent bonds, to give high structured system called aggregate (size around 100-500 nm), which in turn interacting each other via weak hydrogen bonds creating agglomerates (size around 1-40 micrometer).

Anyway, due to the presence of very strong covalent bonds between primary particles, it is not possible to breaking an agglomerate of fillers to further than aggregate level.

The parameters that more influencing the ultimate proprieties of the nanocomposites are primary particle size, specific surface, aggregate and agglomerate structure and surface chemistry.

With the introduction of silica nanoparticle the enhancement on the ultimate mechanical proprieties and in the used of silica has seen a tangible progress. The silica nanoparticle has a high specific surface that confer an improve of the abrasion resistance, tensile strength and tear resistance of the tyre [34].

The surface chemistry plays key role on the nanocomposite proprieties, thought its surface free energy definite as:

$$\gamma = \gamma_d + \gamma_{sp}$$

Where $\gamma$ is the surface free energy, it consists of a dispersive part $\gamma_d$ and a specific part $\gamma_{sp}$. The dispersive part of the surface energy express the interaction between polymer and filler, like van der Waals interaction, and in case of silica particles is low [35].

The specific part of the surface energy express the interaction between the silica particles, it includes hydrogen bonding, polar and acid-base interaction, in case of silica is very high with the consequence that the interaction filler-filler in silica particles is strongly higher than the interaction filler-rubber [36].

The high specific part of the surface energy of silica aggregates or particles is due a covering by silanol groups (-Si-OH) on the surface that is polar and chemically active. There are three kind of silanol groups on the silica surface: isolate (high reactivity), vicinal (low reactivity) or germinal (low concentration, high reactivity) (figure 2.9) [37].

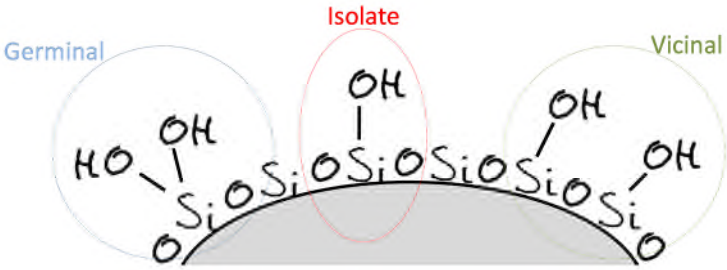


Figure 2.9. Silica surface with germinal, isolated and vicinal silanol groups.

In order to confer appropriates reinforcing proprieties to the silica nanopartilces inside the polymer matrix result fundamental to find compatibilizer molecules able to create a strong chemical interaction between filler and rubber

The more common compatibilizer used are bifunctional organosilanes coupling agent, for their fast kinetic of reaction and ease dispersion and diffusion in the rubber matrix during the mixing. they serve two functions, reacting with the silanol present on the silica particles surface by actives ethoxy groups present in the silane via reactions of hydrolysis and condensation, so called silanization reaction, and then reaction between rubber-reactive groups, constituted by sulfur donors, and the polymer chain [38].

The compatibilization process forms an active reinforcement filler-rubber that with occluded rubber during the mixing into the aggregate structures will go to form a strain-independent reinforcement, the “In-rubber structures”, able to transfer reinforcement proprieties to the nanocomposite as well as the “polymer networks” effect that taking place during the vulcanization. The last strain-independent contribution in a

composite material is called the “hydrodynanmic effect”, based on the viscosity increase of viscous fluids by the addition of particles.

One the proprieties more appreciate of silica is this ability to react efficiently with the compatibilizer decrease so the filler-filler interaction, then decreasing the energy dissipation during repeated destruction and recombination of the filler-filler network, this strain-dependent contribution due to filler-filler interaction is also known as Payne effect, one of the responsible the hysteresis of the nanocomposites (figure 2.10).

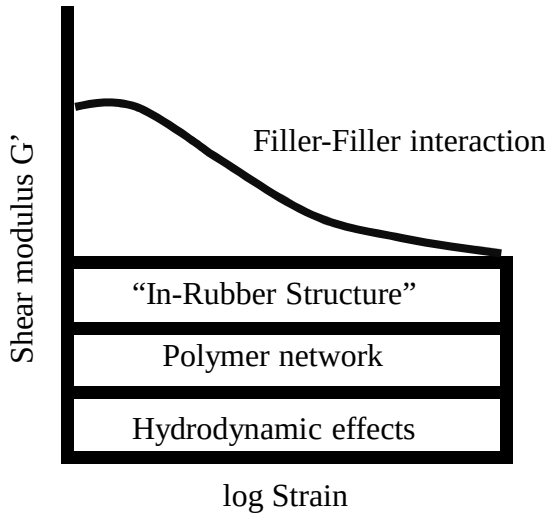


Figure 2.10. Representation of shear modulus modulus *vs* strain in a filler-rubber composite.

---

[1] J. Priestley, A Familiar Introduction to the Study of Electricity, Johnson and Payne (1979).

[2] C.M. Blow, C. Hepburn, Rubber Technology and Manufacture, Butterworth Scientific, London 2nd Ed. (1981).

[3] C. Goodyear, Improvment in the process of divesting caoutchouc, gum-elastic, or india-rubber of its adhesive properties, and also of beleaching the same, and thereby adapting it to various useful purposes., U.S. Patent, 3,633 (1837).
[4] R.B. Prosser, Hancock, Thomas (1786-1865), Dictionary of National Biography 24 (1885-1900).
[5] R.W. Thomson, Improvement in carriage-wheels, U.S. Patent 5,104 (1847).
[6] J. Loasman, F. James, The Hancocks of Marlborough: Rubber, Art and the Industrial Revolution: A Family of Inventive Genius, Oxford University Press (2009).
[7] D.P. Molony, molony, Google Patents, 1922.
[8] Norris, India Rubber World 81 (1930) 55-56.
[9] M. M. Harrison, H.A. Morton, U.S. Patent 1,478,576 (1921).
[10] Y. Coran, Eirich, F.R. (Ed.) Science and Technology of rubber, Academic Press, New York Chapter 7 (1978).
[11] D.J. Schuring, Effect of Tire Rolling Loss on Vehicle Fuel Consumption, Tire Science and Technology 22 (1994) 148-161.
[12] K. C. Baranwal, H.L. Stephens, Basic Elastomer Technology, Rubber Division, American Chemical Society (first edition).
[13] N.J. Morrison, M. Porter, Temperature Effects on the Stability of Intermediates and Crosslinks in Sulfur Vulcanization, Rubber Chem. Technol. 57 (1984) 63-85.
[14] M. Luckmann, W. Steinhoof, Crosslinking of fluoroelastomer and the influence on final properties, Vereniging van Kunststof en Rubber Technologen (February, 13, 2014).
[15] M.R. Krejsa, J.L. Koenig, A Review of Sulfur Crosslinking Fundamentals for Accelerated and Unaccelerated Vulcanization, Rubber Chem. Technol. 66 (1993) 376-410.
[16] P. Versloot, J.G. Haasnoot, P.J. Nieuwenhuizen, J. Reedijk, M. van Duin, J. Put, Sulfur Vulcanization of Simple Model Olefins, Part V: Double Bond Isomerization during Accelerated Sulfur Vulcanization as Studied by Model Olefins, Rubber Chem. Technol. 70 (1997) 106-119.
[17] R. Ding, A.I. Leonov, A.Y. Coran, A Study of the Vulcanization Kinetics of an Accelerated-Sulfur SBR Compound, Rubber Chem. Technol. 69 (1996) 81-91.
[18] R. Damen, P.J. Nieuwenhuizen, J.G. Haasnoot, J. Reedijk, S.M. Couchman, J. Jeffery, J.A. McCleverty, Homogeneous Zinc (II) Catalysis in Accelerated Vulcanization: V. The Prevailing Mechanism of Crosslink Formation in Mercaptobenzothiazole Systems, Rubber Chem. Technol. 76 (2003) 82-100.
[19] Coran, A.Y. Coran, Chemistry of the vulcanization and protection of elastomers: A review of the achievements, J. Appl. Polym. Sci. 87 (2003) 24-30.
[20] Y. Ikeda, Y. Yasuda, T. Ohashi, H. Yokohama, S. Minoda, H. Kobayashi, T. Honma, Dinuclear Bridging Bidentate Zinc/Stearate Complex in Sulfur Cross-Linking of Rubber, Macromol. 48 (2015) 462-475.

[21] M. Geyser, Geyser, W.J. McGill, Thiuram-accelerated sulfur vulcanization. I. The formation of the active sulfurating agent, J. Appl. Polym. Sci. 60 (1996) 425-430.
[22] Y. Ikeda, N. Higashitani, K. Hijikata, Y. Kokubo, Y. Morita, M. Shibayama, N. Osaka, T. Suzuki, H. Endo, S. Kohjiya, Vulcanization: New Focus on a Traditional Technology by Small-Angle Neutron Scattering, Macromol. 42 (2009) 2741-2748.
[23] P. Ghosh, S. Katare, P. Patkar, J.M. Caruthers, V. Venkatasubramanian, K.A. Walker, Sulfur Vulcanization of Natural Rubber for Benzothiazole Accelerated Formulations: From Reaction Mechanisms to a Rational Kinetic Model, Rubber Chem. Technol. 76 (2003) 592-693.
[24] S.J. Blanksby, G.B. Ellison, Bond Dissociation Energies of Organic Molecules, Accounts of Chemical Research 36 (2003) 255-263.
[25] A.A. Watson, Thesis, University of London, (1965).
[26] P.J. Nieuwenhuizen, S. Timal, J.M.v. Veen, J.G. Haasnoot, J. Reedijk, Homogeneous Zinc(II) Catalysis in Accelerated Vulcanization I. Reaction-Stage Modeling and Cross-Link Formation, Rubber Chem. Technol. 71 (1998) 750-765.
[27] P. J. Flory, J. Rehner;, Statistical Mechanics of Crosslinked Polymer Network II. Swelling, J. Chem. Phys. 11 (1943).
[28] S. Rodriguez, C. Masalles, N. Agullo, S. Borros, L. Comellas, F. Broto, Identification of the Intermediates Sulfur Vulcanization of Natural Rubber, Kautschuk Gummi Kunststoffe 52 (1999) 438-445.
[29] G.E. Hammer, X-ray photoelectron spectroscopy of rubber compounds: Temperature dependence and cross-link distribution, Journal of Vacuum Science & Technology A 25 (2007) 1599-1603.
[30] M. Lopez Manchado, M. Lopez, M.A. Lpez-Manchado, M. Arroyo, B. Herrero, J. Biagiotti, Vulcanization kinetics of natural rubber-organoclay nanocomposites, J. Appl. Polym. Sci. 89 (2003) 1-15.
[31] P.J. Nieuwenhuizen, Thesis, University of Leiden, (1998).
[32] A. Blume, Elastomer Technology Course, University of Twente, (2015).
[33] C. Wolf, H.U. Hummel, J. Chem. Soc., Dalton Trans. (1986) 43.
[34] J. Fröhlich, W. Niedermeier, H.D. Luginsland, The effect of filler–filler and filler–elastomer interaction on rubber reinforcement, Composites Part A: Applied Science and Manufacturing 36 (2005) 449-460.
[35] D. R. Bassett, E. A. Boucher, A.C. Zettlemoyer, Adsorption studies on hydrated and dehydrated silicas, J. Colloid Interface Sci. 27 (1968) 649.
[36] A. R. Payne, Low Strain Dynamic Properties of Filled Rubber, Rubber Chem. Technol. 44 (1971) 440-478.
[37] H.D. Luginsland, Am. Chem. Soc., Rubber Div. Meeting, Savannah, Georgia (April 29 - May 1 2002).
[38] A. Hasse, O. Klockmann, Kautsch. Gummi Kunstst. 55 (2002) 5.

# Chapter 3

# Synthesis and characterization of $ZnO/SiO_2$ NPs

The chapter focuses on the preparation of amorphous ZnO NPs grafted on silica particles ($ZnO/SiO_2$) by sol-gel method

$ZnO/SiO_2$ NPs were structurally and morphologically characterized by X-ray Diffraction (XRD) and Transmission Electron Microscopy (TEM), while the nanometricsizes of ZnO were estimated by UV-Vis analysis. The interaction between ZnO and $SiO_2$ was investigated by different spectroscopy techniques as Solid State Nuclear Magnetic Resonance (NMR), Attenuated Total Reflection-Fourier Transform Infrared Spectroscopy (ATR-FTIR) and X-ray Photoelectron Spectroscopy (XPS). The morphological and structural characteristics of $ZnO/SiO_2$ obtained by changing the synthesis conditions were discussed in order to find the better properties of the material as curing accelerator

### 3.1. Sol-gel synthesis of nanostructures

In the tyre technology the syntheses of both bare silica nanoparticles filler and microcrystalline ZnO are well consolidated industrial process.

In these last decades nanomaterials have been largely investigated and applied in many technological and scientific fields due to their peculiar chemical and physical proprieties. This prompt the scientists to develop a wide range of techniques for the synthesis of NPs with different morphology, structure and composition and to propose methods for design nanostructures adapt to high technology applications.

In general, two main approaches for nanomaterials synthesis can be followed: “top-down” or “bottom-up” [1].

The top-down route starts form macroscopic initial structure, which can reduce in nanoscale.

Typical top-down method are lithography and ball-milling synthesis.

The bottom-up approach is constituted by the formation of a solid compound by the aggregation of atomic and molecular constituents. This synthetic route allows to control during the preparation phase the functionalities and the properties of the material through the suitable choice of the precursors and the synthesis parameters.

The synthesis via sol-gel is one of the most appreciated and used bottom-up approaches. The sol-gel method starts form hydrolysis and condensation of the precursors, in same case assisted by a template, for the production of powder, film and monoliths [2]. It is distinguished from the mild reaction conditions which permit to operate on the process characteristics in a way more immediate and precise, it avoids used of high costly devices, it is prefer for its versatility, reproducibility and good quality products.

Sol-gel route has been widely used for the synthesis of differently shaped nanomaterials: spherical, cube, prism, hexagon, octahedron, disk, wire, rod, tube etc. [3].

The sol-gel method allows of synthesizing also oxide NPs grown on particles of metals or oxides Thanks to the high thermal stability and to the better control of the precursors reactivity, this permits to reduce the consumption of precious materials and to have a precise controls of size, shape and crystallinity of the nanosystems [4]. Besides systems with novel properties with respect to the constituent compounds can be obtained

Basing on these considerations, the sol-gel method has been chosen to synthesize ZnO NPs anchored on preformed $SiO_2$ NPs.

In particular, the sol-gel synthesis has revealed to be an useful method to growth the ZnO NPs directly on the surface of the supporting oxide $SiO_2$, allowing to control the surface nucleation and growing processes of ZnO, it prevents the undesired large crystal growth of ZnO through Ostwald-ripening or agglomeration.

The decoration of silica nanoparticles with amorphous ZnO nanoparticles is strategic in order to reach a better distribution in the rubber matrix, an higher reactivity in curing accelerating process and, therefore, to minimize the amount of ZnO employed in the vulcanized silica rubber nanocomposites.

### 3.2. Synthesis of ZnO anchored $SiO_2$ ($ZnO/SiO_2$)

#### 3.2.1. Reactants and materials

$ZnO/SiO_2$ synthesis: precipitated silica Rhodia Zeosil MP1165 (BET specific surface area 160 $m^2$ $g^{-1}$); $Zn(CH3COO)_2 \cdot 2H_2O$ (99.99 %) from Carlo Erba; NaOH (98 %) from Fluka; anhydrous ethanol EtOH (99.9%) from Scharlau used as solvent; Milli-Q water with resistivity > 18.2 MΩ•cm.

#### 3.2.2. Synthesis procedure

ZnO NPs formed on the silica surface were synthesized by a sol-gel procedure at low temperature. Silica Rhodia Zeosil MP1165(0.426 mol) were dispersed in 0.9 l of ethanol by sonication for 10 min (pulses: 1s; 20 kHz). Then suitable amount of $Zn(CH_3COO)_2 \cdot 2H_2O$ precursor (0.96-0.058 Zn/Si molar ratio) and of NaOH (0.23, 0.094, 0.0 NaOH/Si molar ratio) were added under stirring to the $SiO_2$ suspension at 65 °C. (Table 3.1). ZnO NPs formed by hydrolysis and condensation on the silica surface (see paragraph 2.3). $Zn(CH_3COO)_2$ in anhydrous ethanol

promotes the heterogenic nucleation of ZnO due to its capacity to give a batter control of hydrolysis leading to a fast nucleation without growth of crystallization seeds [5].

After 20 minutes $ZnO/SiO_2$ particles were filtered, successively washed four times with ethanol and dried in air at room temperature. In the absence of silica, a stable colloidal solution formed and no precipitation of ZnO NPs occurred.

| **Name** | **$Zn(Ac)_2*2H_2O$ (mol)** | **$SiO_2$ (mol)** | **NaOH (mol)** | **ZnO (wt%) (nominal)** | **ZnO (wt%)** |
|---|---|---|---|---|---|
| **ZSO-50.2** | 0.409 | 0.426 | 0.10 | 56.0 | 50.2 |
| **ZSO-14.2** | 0.205 | 0.426 | 0.10 | 28.0 | 14.2 |
| **ZSO -7.7** | 0.081 | 0.426 | 0.10 | 16.2 | 7.7 |
| **ZSO -4.0** | 0.015 | 0.426 | 0.10 | 4.6 | 4.0 |
| **ZSO -2.9** | 0.015 | 0.426 | 0.04 | 4.6 | 2.9 |
| **ZSO -0.0** | 0.015 | 0.426 | 0.0 | 4.6 | 0.0 |

Table 3.1**.** Synthesis reactants and ZnO content of ZSO-X.

The actual loading of ZnO was evaluated by ICP Zn analysis (see Appendix A.2.1.) and resulted lower than the nominal one (Table 3.1). The sol-gel reaction yield ranged between 50 and 90 % and depended on the basicity of the solution. In fact, by maintaining the same amount of zinc precursor, the ZnO loading increases with the amount of hydroxide and in the absence of hydroxide no ZnO grew on silica particles.

While, when the silica was not present in the solution, the same synthetic approach didn't lead to the formation of single ZnO nanoparticles.

Hereafter ZnO decorated $SiO_2$ NPs will be labeled ZSO-X, where X refers to the actual amount (weight %) of ZnO on $SiO_2$.

### 3.3. Morphological and Structural Characterization of ZnO/$SiO_2$

The morphological and structural characterization of ZnO/$SiO_2$ powder were investigated by TEM, XRD, UV-Vis analysis, to assess the size, shape and crystallinity of the system. The chemical interaction between ZnO and $SiO_2$ was investigated by ATR-FTIR and NMR techniques (see Appendix A.2.6.).

#### 3.3.1 X-ray Diffraction (XRD)

ZSO-X (X<14.2) XRD (Appendix A.2.3.) patterns showed amorphous structure whatever the Zn amount, instead ZSO-14.2 and ZSO-50.2, with higher ZnO loading, showed the reflections of *wurtzite* (JCPDS Card no. 36-1451),

XRD patterns of ZSO-4.0, ZSO-7.7 and ZSO-50.2 are shown in figure 3.2, where the reflections of *wurtzite* are also indicated.

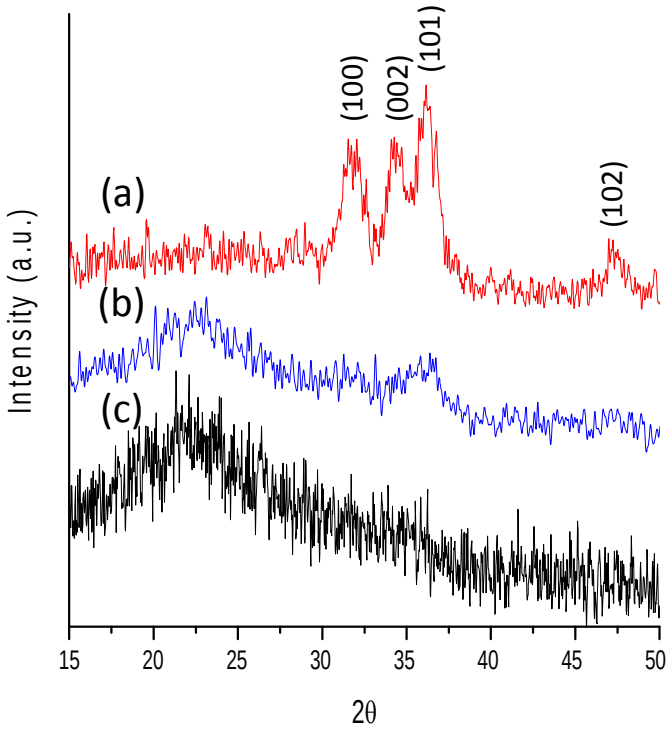


Figure 3.2. XRD patterns of (a) ZSO-50.2, (b) ZSO-14.2 and (c) ZSO-7.7. The reflections of *wurtzite* are indicated.

### 3.3.2 Transmission Electron Microscopy (TEM)

TEM and HRTEM (Appendix A.2.2.) images of ZSO-4.0,ZSO-7.7 and ZSO-50.2are shown in figure 3.3. It appears that silica NPs (average sizes 20-30 nm) are decorated by small spherical ZnO nanoparticles, not highly homogeneously distributed. Their sizes vary with the zinc loading: 4-6 nm in ZSO-4.0 and ZSO-7.7, a larger value, 5-8 nm, in ZSO-50.2. At lower ZnO concentration (figure 3.3 a, b) ZnO NPs are distributed on the surface without significant aggregations while at higher ZnO loading (ZSO-50.2) the particles give rise to surface aggregates (figure 3.3 d, e)

In agreement with the XRD results, HRTEM images demonstrate the presence of amorphous ZnO NPs in ZSO composites with lower Zn loading (figure 3.3 c.), whereas the lattice fringes of the (0002) *wurtzite* planes are easily identified in the case of ZSO-50.2 (figure 3.3 f.).

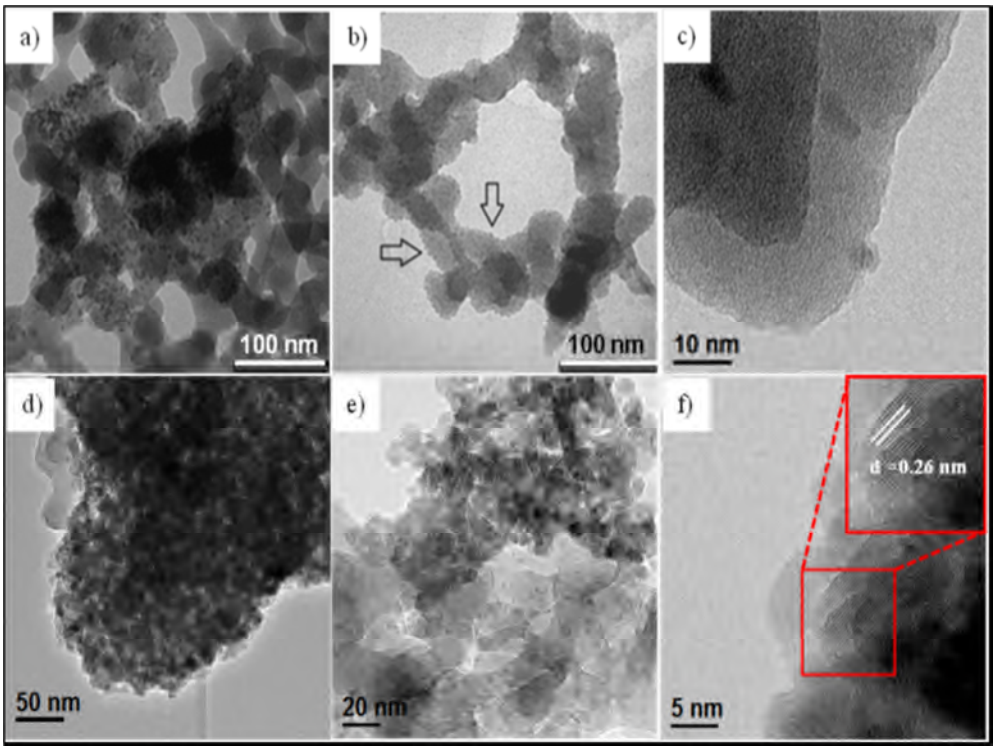


Figure 3.3. TEM and HRTEM images of a) ZSO-4.0; b), c) ZSO-7.7; d), e), f) ZSO-50.2

### 3.3.3 UV-Vis analysis

Nanosized dimensions of ZnO particles as measured by TEM are in accordance with the UV-Vis absorption spectra (Appendix A.2.4.) (figure 3.4). In fact the largest particles ZSO-50.2 showed a band gap (3.29 eV) similar to that of bulk ZnO [6] while a progressive blue shift of the ZnO band gap takes place when the zinc amount decreases in

ZSO-7.7 (3.38 eV), ZSO-2.9 (3.40 eV) and ZSO-4.0 (3.55 eV) due to the smaller ZnO NPs dimension in agreement with the quantum-size effects (the absorption edge lines in Fig. 2.4 have been split to draw the tangents and calculate the band gap energy)

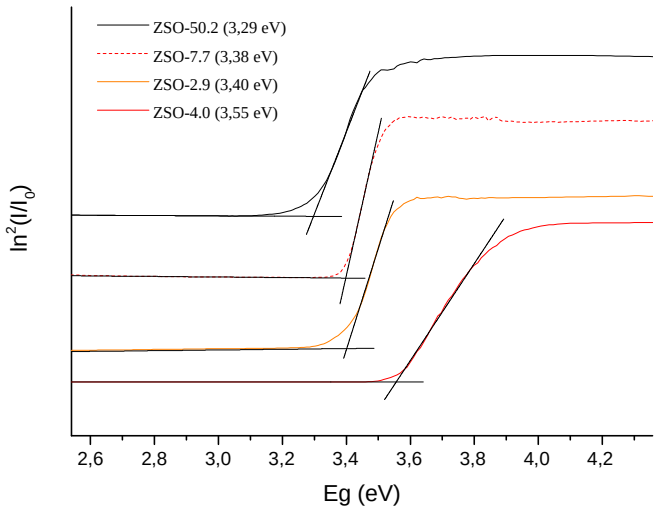


Figure 3.4. UV-Vis spectra of ZSO-50.2, ZSO-7.7, ZSO-2.9, ZSO-4.0

The figure 3.4. showed the correlation between the amount of NaOH and zinc acetate used in the synthesis and the band gap of ZnO NPs. It is evident that increasing the amount of NaOH or decreasing the amount of zinc precursor the ZnO particle sizes decrease, proved by the blue-shift of the absorption spectra due to higher Eg.

The theoretical radius of ZnO spherical nanoparticles (*r*) was calculated from the detected band gap (*Eg*) by Schrodinger equation [6, 7]

$$E_g^{nano} = E_g^{bulk} + \frac{\hbar^2\pi^2}{2Mr^2} (1)$$

where $M = m_e + m_h$, and $m_e$ and $m_h$ are the mass of the electron and of the hole respectively The radius calculated of ZSO-7.7, ZSO-2.9, ZSO-4.0 nanoparticles are reported in table 3.2.

| Name | Eg (eV) | Radius (nm) |
|---|---|---|
| **ZSO-7.7** | 3.38 | 4.5 |
| **ZSO-2.9** | 3.40 | 3.9 |
| **ZSO-4.0** | 3.55 | 2.3 |

Table 3.2. Nanoparticles radius calculated by Schrodinger equation

The average nanoparticles size calculated by Schrodinger equation were in good agreement with the dimension obtained by TEM analysis.

The relation between amount of zinc acetate and sodium hydroxide at the equivalent amount of silica and solvent rate is related to the hydrolysis of $Zn(CH_3COO)_2$ in the presence of NaOH.

The figure 3.6. shows as Zn(II) in water solution form different species by increasing pH, due to the amphoteric behavior of zinc: $Zn^{2+}$(aq.), $Zn(OH)^{+}$(aq.), $Zn(OH)_2$(aq.), $Zn(OH)_3^{-}$(aq.), $Zn(OH)_4^{2-}$(aq.) over the range of pH.

When these hydroxozincate complexes condensate Zn-O-Zn bonds form due to the dehydratation reactions

$$Zn(OH)_n^{2-n} + Zn(OH)_n^{2-n} \leftrightarrow Zn_2O(OH)_{2n-2}^{4-2n} + H_2O$$

Where $n$ = 2 or 4.

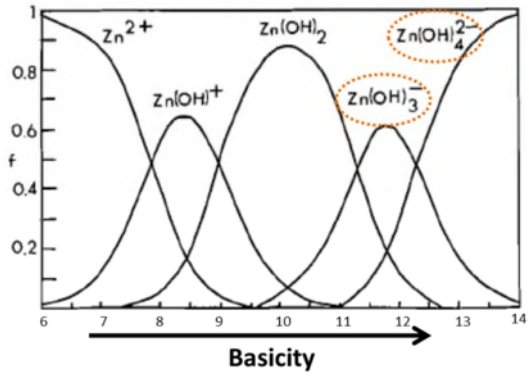


Figure 3.6. Fraction of Zn(II) existing at the equilibrium as $Zn^{2+}$ (aq.), $Zn(OH)^{+}$(aq.), $Zn(OH)_2$(aq.), $Zn(OH)_3^{-}$(aq.), $Zn(OH)_4^{2-}$(aq.) over the range of pH

This equilibrium may be used to explain the small dimension of ZnO NPs growth on silica at relative high amount of NaOH. Increasing the amount of NaOH , in the solution the amount of reactive $Zn(OH)_3^{-}$ and $Zn(OH)_4^{2-}$ species at the equilibrium icrease. These hydroxozincate species have higher affinity with the silanol groups of the silica surface carrying on to the formation of small ZnO nanoparticles.

When the condition are less basic $Zn^{2+}$, $Zn(OH)^{+}$, $Zn(OH)_2$ species are preferentially present at the equilibrium and ZnO nanoparticles do not form at the silica surface.

As an example, it was proved by the comparison between the sample ZSO-4.0 and ZSO-2.9, obtained by the same amount of zinc precursor (Table 3.1) ZSO-4.0 NPs have smaller dimension due to the higher concentration of NaOH than in the ZSO-2.9.

### 3.3.4 Attenuated Total Reflection-Fourier Transform Infrared Spectroscopy (ATR-FTIR) analysis

ATR-FTIR (Appendix A.2.5.) spectra of ZSO-X (figure 3.7) aimed to investigate the bond interaction between ZnO particles and $SiO_2$. In this context, the band at 954 $cm^{-1}$ which in bare $SiO_2$ spectrum was attributed to the –SiOH [8]stretching vibration (figure 3.7. a), in ZSO-4.0 and ZSO-7.7 spectra becomes a shoulder, broadens and gradually shifts to higher frequency, ~ 963-965 $cm^{-1}$ (Figure 3.7. b and c). Basing on the spectra of zincosilicates [9] and $ZnO/SiO_2$ composites [10, 11] reported in the literature, the change may be attributed to the co-presence of –SiOH and of the symmetric Si-O-Zn stretching modes. This suggests the formation of a covalent bond between a number of surface silanol groups and the growing ZnO particles.

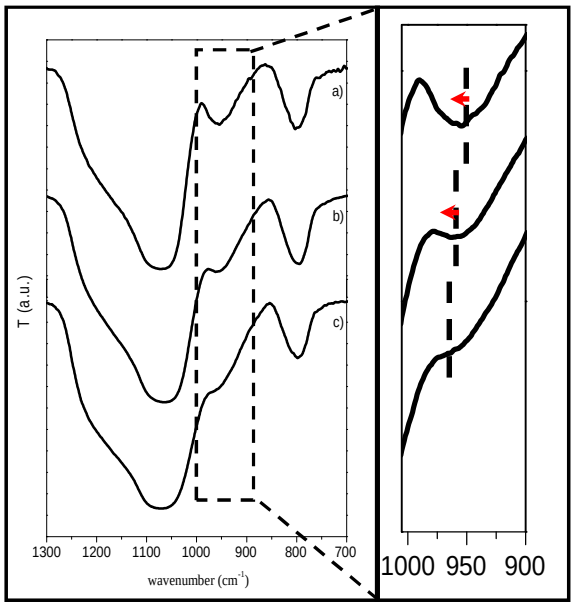


Figure 3.7. ATR-FTIR spectra of (a) $SiO_2$; (b) ZSO-4.0; (c) ZSO-7.7. The shift of the –Si-OH stretching vibration is evidenced.

This evidences that on the silica surface Si-OH groups react by condensation with $Zn(OH)_3^-$ and $Zn(OH)_4^{2-}$ species producing the Si-O-Zn bounds.

Therefore the ZnO NPs start to nucleate on the silica surface through the formation of Zn-O-Zn bonds between the hydroxozincate species and this surface species.

### 3.3.5. $^{29}$Si MAS, $^{29}$Si CP MAS and $^{1}$H MAS NMR analysis

The interaction between $SiO_2$ and ZnO and the Si-O-Zn bond formation were studied also by Solid State $^{29}$Si MAS, $^{29}$Si CP MAS and $^{1}$H MAS NMR.

The $^{29}$Si SP-MAS spectra of ZSO-4.0 and ZSO-7.7 samples show the large signals typical of amorphous structures and are very similar to the spectrum recorded on $SiO_2$ (figure 3.8). The signals attributed to $Q_2$, $Q_3$ and $Q_4$ resonances present a 2-ppm up field shift in comparison with the corresponding resonances in $SiO_2$, without valuable changes in line-width. The spectrum of ZSO-50.2 with the highest loading of crystalline ZnO (see figure 3.2) shows $Q_4$ and $Q_3$ signals, and a broad shoulder in the range -70-100 ppm due to the overlapping of at least four components, suggesting both the presence of pure $SiO_2$ domains and the formation of Zn-O-Si bonds in different substituted Si units [12].

The observed shift of Qn resonances in ZSO-X samples is attributable to the partial substitution of Si-O-Si and Si-OH bonds with Si-O-Zn bonds on the particle surface and to consequent changes in the torsion angles T-Ô-T (T stands for a generic cation). Although Qn shifts were reported for different zincosilicates [12], Cambloret al. [13], also reported that there is not a reliable rule for calculating the downfield shift due to Si

substitution, as in the well-known case of replacement of OH with Al in $SiO_2$-$Al_2O_3$ samples. [14]

Thus, although a univocal identification of the Si-O-Zn signals is not possible, the general behavior of ZSO-4.0 and ZSO-7.7 suggests the interaction between ZnO and $SiO_2$ by means of heterometallic Si-O-Zn bonds.

This conclusion is supported by the results of the quantitative analysis of $^{29}$Si SP MAS NMR spectra reported in Table 3.2..

The amount of $Q_2$ and $Q_3$ units is higher in the ZSO-X samples than in $SiO_2$ (according to $Q_3/Q_4$ and $(Q_2 + Q_3)/Q_4$ ratios in Table 3.2), accounting for the structural changes of the silica surface by interaction with ZnO. $Q_2$ and $Q_3$ content slightly decreases moving from the ZSO-4.0 to the ZSO-7.7 sample. This may be associated to an increased aggregation of ZnO particles in ZSO-7.7, which lowers their condensation ability with silica. On the contrary, the strong increase of $Q_2$ and $Q_3$ units in ZSO-50.2 is a probable consequence of the different zincosilicate structures, accounting for the resonances between -70 and -110 ppm.

The presence of surface sodium silicate due to the synthesis conditions cannot be totally excluded (see XPS analysis. paragraph 2.3.6 ) and its resonances [14] could be hidden under the main peaks of the spectra. The comparison between the SP MAS spectra of bare $SiO_2$ before and after NaOH treatment (not reported) indicates a slight increase in the number of $Q_3$ and $Q_2$ units after the base treatment, without any change in the signal position. Since it is known that the addition of sodium to pure silica leads to a downfield δ shift (e.g. according to [14] the spectrum of sodium silicate produces 4 peaks at -72, -80 -87 and -96 ppm), the

observed upfield shift of $Q_n$ resonances in ZSO-X samples strengthens the above discussion on Zn-O-Si bond formation.

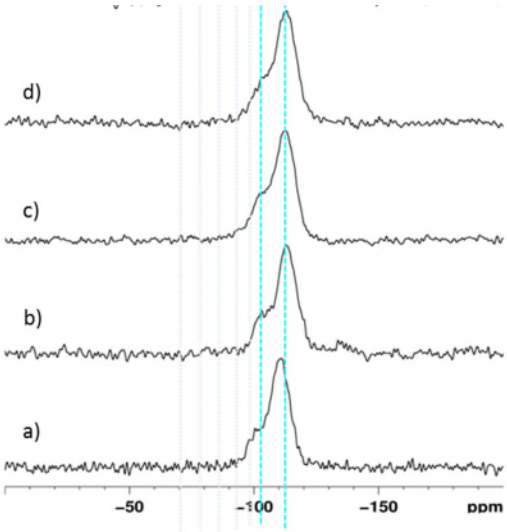


Figure 3.8. $^{29}$Si single pulse MAS NMR spectra of a) $SiO_2$; b) ZSO-4.0 ; c) ZSO-7.7 and d) ZSO-50.

| | | | $Q_2$ | | $Q_3$ | | $Q_4$ | | $Q_3/Q_4$ | $(Q_2+Q_3)/Q_4$ |
|---|---|---|---|---|---|---|---|---|---|---|
| | **δ (ppm)** | **%** | **δ (ppm)** | **%** | **δ (ppm)** | **%** | **δ (ppm)** | **%** | | |
| $SiO_2$ | - | - | -91,6 | 0,6 | -100,5 | 18,2 | -110,5 | 81,3 | 0,22 | 0,23 |
| ZSO-4.0 | - | - | -92,2 | 4,1 | -102,6 | 22,8 | -112,6 | 73,2 | 0,31 | 0,37 |
| ZSO-7.7 | - | - | -92,6 | 3,8 | -102,1 | 19,5 | -112,5 | 76,6 | 0,25 | 0,30 |
| ZSO-50.2 | -77,5 | 4,0 | -87,5 | 12,0 | -98,7 | 27,8 | -111,1 | 56,1 | 0,50 | 0,71 |

Table 3.3. $^{29}$Si single pulse MAS NMR: relative amount and assignment of the main identified units

$^{29}$Si CP-MAS NMR spectra of $SiO_2$ and ZSO-X confirm the previous results (figure 3.9 and Table 3.3).

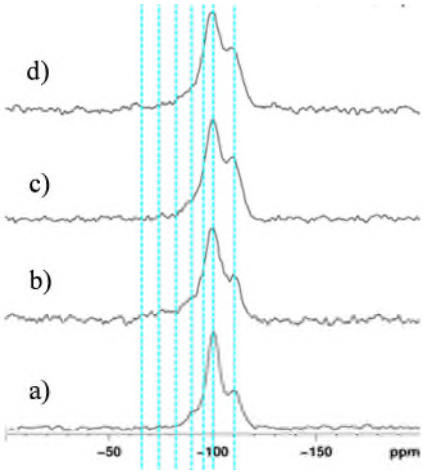


Figure 3.9. $^{29}$Si cross-polarization MAS NMR spectra of a) $SiO_2$; b) ZSO-4.0 ; c) ZSO-7.7 and d) ZSO-50.2

| sample | δ (ppm) | | | | | | | | |
|---|---|---|---|---|---|---|---|---|---|
| | **-90,4** | **-100,1** | **-110,3** | **$Q_3/Q_4$** | | | | | |
| $SiO_2$ | 9,4 | 64,3 | 26,3 | 2,4 | | | | | |
| ZSO-2.5 | 4,4 | 64,2 | 31,4 | 2,0 | | | | | |
| ZSO-4.0 | 7,3 | 57,6 | 35,1 | 1,6 | | | | | |
| ZSO-7.0 | 20,1 | 46,1 | 33,9 | 1,4 | | | | | |
| | | | | **δ (ppm)** | | | | | |
| | **-65,4** | **-73,6** | **-81,7** | **-86,4** | **-91,2** | **-95,7** | **-100,3** | **-105,9** | **-109,6** |
| ZSO-50.2 | 7,3 | 14,5 | 19,1 | 5,7 | 14,6 | 10,8 | 18,2 | 0,9 | 8,8 |

Table 3.3. $^{29}$Si CP-MAS NMR: relative amount and assignment of the main identified units

The $^{29}$Si CP-MAS NMR spectra of $SiO_2$ and ZSO-X confirm the SP MAS results The smaller broadening of ZnS-4.0 and ZSO-7.7 signals compared to $SiO_2$ resonances can be related to the formation of Si-O-Zn bonds and to the changes in the torsion angles T-Ô-T, as already

mentioned above. The semi-quantitative analysis obtained by CP MAS spectra deconvolution (Table 3.3) shows that the $Q_3/Q_4$ ratio decreases significantly from pure $SiO_2$ to ZnS-X samples with increasing the ZnO content. Since the CP-MAS experiment enhances the resonances intensity of Si atoms close to protons, these results suggest a replacement of the surface Si-OH groups with the formation of Zn-O-Si bonds. However, also the $^{29}$Si CP-MAS spectrum recorded on bare $SiO_2$ after NaOH treatment displays an increase of the $Q_4$ units and, consequently, both the effect of Si substitution with Zn and the formation of sodium silicate units must be considered.

The $^{29}$Si CP-MAS spectrum of ZnS-50.2 sample showed (figure 3.9) four new sharp signals in the range -60 – -90 ppm. Moreover, $Q_3/Q_4$ ratio increased due to the strong large signals observed between -90 and -110 ppm. The new signals in the ZnS-50.2 spectrum can account for Si units substituted with a different number of Si-O-Zn bonds and their sharpness is probably due to the ZnO crystalline features (*wurtzite*) that induces the formation of symmetrically inequivalent Si-sites. [15].

$^1$H MAS NMR spectra (figure 3.10) of $SiO_2$ and ZnO-X-$SiO_2$ show peaks due to silanol protons in different hydrogen-bonding environments (Table 3.4)

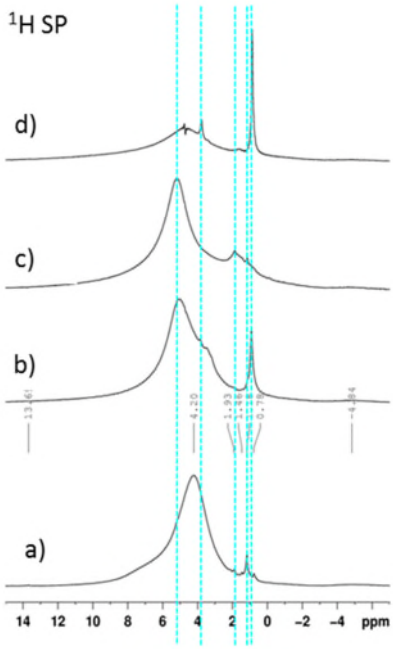


Figure 3.10. $^{1}H$ MAS NMR spectra of a) $SiO_2$; b) $SiO_2/ZnO$-2.9; c) $SiO_2/ZnO$-4.0; d) $SiO_2/ZnO$-7.7; e) $SiO_2/ZnO$-50.2

| | | | $Q_2$ | | $Q_3$ | | $Q_4$ | | $Q_3/Q_4$ | $(Q_2+Q_3)/Q_4$ |
|---|---|---|---|---|---|---|---|---|---|---|
| | **δ (ppm)** | **%** | **δ (ppm)** | **%** | **δ (ppm)** | **%** | **δ (ppm)** | **%** | | |
| $SiO_2$ | - | - | *-91,6* | 0,6 | *-100,5* | 18,2 | *-110,5* | 81,3 | 0,22 | 0,23 |
| ZSO-2.5 | - | - | *-92,2* | 17,5 | *-102,6* | 21,5 | *-112,6* | 60,9 | 0,35 | 0,64 |
| ZSO-4.0 | - | - | *-93,1* | 4,1 | *-102,2* | 22,8 | *-112,5* | 73,2 | 0,31 | 0,37 |
| ZSO-7.7 | - | - | *-92,6* | 3,8 | *-102,1* | 19,5 | *-112,5* | 76,6 | 0,25 | 0,30 |
| ZSO-50.2 | -77,5 | 4,0 | *-87,5* | 12,0 | *-98,7* | 27,8 | *-111,1* | 56,1 | 0,50 | 0,71 |

Table 3.4. Main identified units with relative amounts and assignment [16, 17].

However, the amount of protons is lower in the ZnO/ $SiO_2$ samples and decreases with the amount of ZnO, thus supporting the silanol groups replacement with formation of Si-O-Zn bonds.

### 3.3.6 X-ray Photoelectron Spectroscopy (XPS)

The surface composition of ZSO-X was studied by XPS (Appendix A.2.7.) in comparison with bare $SiO_2$ treated with NaOH under the same conditions of the ZSO-X synthesis procedure.

The survey spectrum of bare $SiO_2$ powders treated with NaOH showed the expected silicon and oxygen lines. The energy position of the Si2p peak is at 103.2 eV, whereas the O1s band is center at 532.5 eV with a small contribution (*ca.* 10% of the total) at 530.7 eV (figure 3.11).

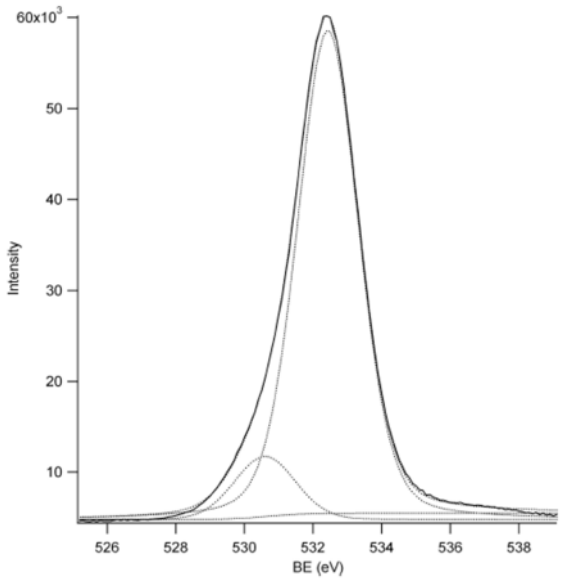


Figure 3.11. XPS O1s peak of $SiO_2$ sample treated with NaOH

This latter component may be likely assigned to the presence of Si-OH and/or Si-$O^-$ groups at the surface of silica particles due to the treatment

with the sodium hydroxide solution. This also agrees with the observation of the Na 1s (BE = 1071.8 eV) line in the spectrum and with NMR results.

In ZSO-4.0 and ZSO-7.7 nanopowders the Si2p and O1s regions showed similar features. Si2p is observed at ~103 eV, whereas the O1s peak displays a slightly asymmetric shape on the low energy side (figure 3.12) . Spectral deconvolution of the O1s region reveals the presence of two components. The main peak is centered at binding energy of 532.5 eV and corresponds to the silicon oxide network; the minor component at lower energy (530.6 – 530.9 eV) is assigned to OH groups as detected in hydroxide or in oxo-hydroxo compounds. Similar binding energy values were also attributed to bridging oxygen atoms in Zn-O-Si units, at the interface between $SiO_2$ and ZnO [18]. Remarkably, we did not observe in these samples a clear oxygen component related to a ZnO network even though the Zn2p line is peaked at a position typical for $Zn^{2+}$ species in an oxide environment ($Zn2p_{3/2}$ = 1021.9 – 1022.0 eV). These findings support the hypothesis that the *wurtzite* crystal phase does not form at low ZnO concentrations and suggest that a strong interfacial interaction is established between silica and the amorphous zinc, oxo-hydroxo particles thus leading to the formation of bridging Si-O-Zn units. Accordingly, the minor oxygen component represents *ca.* 10% and 25% of the total oxygen amount in ZSO-4.0 and ZSO-7.7 samples, respectively.

In the high loaded ZnO decorated silica NPs (ZSO-50.2) the O1s peak band-shape is broader than previously observed, owing to the presence of oxygen species in more different chemical environments. Spectral deconvolution of the peak resulted in three bands centered at 532.3 eV (abundance ~ 40%), 531.1 eV (abundance ~ 30%) and 529.8 eV

(abundance ~ 30%) within experimental uncertainty. Such values account for oxygen atoms in silica, surface hydroxyl and/or oxygen bridging groups, and oxygen in the *wurtzite* network, respectively. The presence of the low energy component is in agreement with the detection of crystalline ZnO in the high loaded samples. Regarding the Zn2p peak, we confirm again the formation of an oxide environment around the $Zn^{2+}$ centers ($Zn2p_{3/2}$ = 1021.1 eV) although we cannot discriminate between the different Zn-O*X* species (*X* = H, Zn, Si).

A final observation concerns the purity of the samples. The carbon amount is always on the order of few at % and is mainly due to adventitious contamination (C1s = 284.9 eV). Only in the high ZnO loaded sample we observe a further component at 289.2 eV associated to carbonate species. Hence, it appears that very small residual traces due to the zinc acetate precursor compound are deposited on the surface of the silica particles.

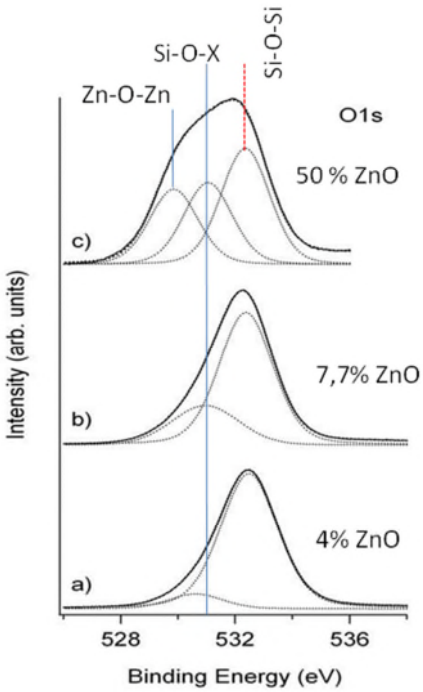

Figure 3.12. XPS O1s peaks of a) ZSO-4.0; b) ZSO-7.7 and c) ZSO-50.2

### 3.4. Conclusions

In this chapter a novel low temperature sol-gel synthesis to produce ZnO NPs anchored to silica filler nanoparticles is reported. $ZnO/SiO_2$ were prepared by hydrolysis and condensation of $Zn(CH_3COO)_2$ in ethanol solution of NaOH in the presence of $SiO_2$ particles

By this way, Zn(II) in basic solution form the hydrolyzed zinc species $Zn(OH)_n^{2-n}$ which interact with the silanol groups at the surface of silica particles, which act as centers of nucleation, and induce the growth of ZnO NPs.

In particular, at lower loading of Zn precursor (<14%), ZnO NPs (4-7 nm) have amorphous structure and spherical shapes. They are distributed on the silica surface and leaving largely exposed silica surface.

At higher ZnO loading (≥14%) the surface of silanol groups are less available, and $Zn(OH)_n^{2-n}$ primarily interact with the Zn-OH surface units condensing in larger and crystalline wurtzite particles.

Amorphous ZnO NPs do not chemisorb on silica surface, but they grow on it, as demonstrated both by the spectroscopic evidences and by their absence in the absence of $SiO_2$. $Zn(OH)_3^-$ and $Zn(OH)_4^2$ species, formed by Zn(II) centers in basic solution, react with the surface silanol groups leading to a preferential formation of Si-O-Zn bounds.

Thus, ZnO particles immobilized by covalent bonds onto the silica surface provides a homogeneous dispersion of zinc minimizing the potential release of ZnO from silica and increases the accessibility of curing reactants to $Zn^{2+}$ ions.

[1] G. A. Ozin, A. C. Arsenault, L. Cademartiri, Nanochemistry: A Chemical Approach to Nanomaterials, Royal Society of Chemistry (2009).
[2] C. Klingshirn, J. Fallert, H. Zhou, J. Sartor, C. Thiele, F. Maier-Flaig, D. Schneider, H. Kalt, 65 years of ZnO research – old and very recent results, physica status solidi (b) 247 (2010) 1424-1447.
[3] C.-H. Lu, C.-H. Yeh, Influence of hydrothermal conditions on the morphology and particle size of zinc oxide powder, Ceramics International 26 (2000) 351-357.
[4] B. Ludi, M. Niederberger, Zinc oxide nanoparticles: chemical mechanisms and classical and non-classical crystallization, Dalton transactions 42 (2013) 12554-12568.
[5] S. Yamabi, H. Imai, Growth conditions for wurtzite zinc oxide films in aqueous solutions, Journal of Materials Chemistry 12 (2002) 3773-3778.
[6] L. Irimpan, V.P.N. Nampoori, P. Radhakrishnan, Visible luminescence mechanism in nano ZnO under weak confinement regime, Journal of Applied Physics 104 (2008) 113112-113115.
[7] Y. Kayanuma, Quantum-size effects of interacting electrons and holes in semiconductor microcrystals with spherical shape, Physical Review B 38 (1988) 9797-9805.
[8] M.G. Fonseca, A.S. Olivera, C. Airoldi, Silylating Agents Grafted onto Silica Derived from Leached Chrysotile, J. Colloid Interface Sci 240 (2001) 533-538.
[9] S.P. A. Roy, S. Rabe, B. Rellinghaus, H. Zähres, F.E. Kruis, M.Driess, First Preparation of Nanocrystalline Zinc Silicate by Chemical Vapor Synthesis Using an Organometallic Single-Source Precursor, Chem. Eur. J. 10 (2004) 1565-1575.
[10] W.V. M. Kotecha, B. Rohe, M. Tausch, NMR investigations of silane-coated nano-sized ZnO particles, Microp. Mesop. Mater 95 (2006) 66-75.
[11] M.E.H. X. Collard, B. L. Su, C. Aprile, Synthesis of novel mesoporous ZnO/SiO2 composites for the photodegradation of organic dyes, Microporous Mesoporous Mater. 184 (2014) 90-96.
[12] C. Cannas, M. Casu, A. Lai, A. Musinu, G. Piccaluga, XRD, TEM and 29Si MAS NMR study of sol-gel ZnO-SiO2 nanocomposites, Journal of Materials Chemistry 9 (1999) 1765-1769.
[13] M.A. Camblor, M.E. Davis, 29Si MAS NMR Spectroscopy of Tectozincosilicates, The Journal of Physical Chemistry 98 (1994) 13151-13156.
[14] L. Martel, S. Cadars, E. Véron, D. Massiot, M. Deschamps, Effects of the orientation of the 23Na–29Si dipolar vector on the dipolar mediated heteronuclear solid state NMR correlation spectrum of crystalline sodium silicates, Solid State Nuclear Magnetic Resonance 45–46 (2012) 1-10.
[15] C. Röhrig, I. Dierdorf, H. Gies, X-ray powder diffraction and NMR-spectroscopic investigations on a porous zincosilicate related to the zeolite VPI-7 (VSV), Journal of Physics and Chemistry of Solids 56 (1995) 1369-1376.

[16] D.R. Kinney, I.S. Chuang, G.E. Maciel, Water and the silica surface as studied by variable-temperature high-resolution proton NMR, Journal of the American Chemical Society 115 (1993) 6786-6794.
[17] J. Brus, Solid-State NMR Study of Phase Separation and Order of Water Molecules and Silanol Groups in Polysiloxane Networks, Journal of Sol-Gel Science and Technology 25 (2002) 17-28.
[18] W.F.S. J.F. Moulder, P.E. Sobol, K.D. Bomben, in: G. Chastain (Ed.), Handbook of X-ray Photoelectron Spectroscopy, Perkin Elmer Corporation, Eden Prairie (Minnesota) (1992).

# Chapter 4

# New insights into the catalytic activity of silica anchored ZnO nanoparticles in rubber vulcanization

The chapter is dedicated to study the catalytic activity of the $ZnO/SiO_2$ in the sulfur crosslinking of isoprene rubber (IR). The study compares the behavior of $ZnO/SiO_2$ NPs with that of conventional microcrystalline ZnO particles. The curing efficiency was evaluated by dynamic mechanical proprieties of vulcanized $ZnO/SiO_2$ nanocomposites. The apparent activation energy of the different steps of the curing process was assessed by using a kinetic approach at non-isothermal conditions [1, 2] and employing Differential Scanning Calorimetric (DSC) measurements.

The structure of the reaction intermediates was investigated and sulfur network in the final cured material as for the length of the polysulfide chains and the cross-linking degree in the final cured material, by using the Model Compound Vulcanization (MCV) method [3, 4]. This consists in the vulcanization of a low molecular weight compound with chemical properties similar to the rubber (2,3-dimethyl-2-butuene, TME, is a model compound for IR), which produces cured compounds easily analyzable by LC-GM chromatography [5, 6] and $^1$H-Nuclear Magnetic Resonance ($^1$H-NMR) spectroscopy [7]. The comparison between the two catalysts has been also discussed on the basis of Fourier-Transform Infrared Spectroscopy FTIR investigation which elucidates some of the intermediate reaction products.

## 4.2. Preparation of silica/IR nanocomposites

### 4.2.1. Materials

Compounding: Cis-1,4-polyisoprene rubber (IR), from Nizhnekamskneftechim Expor; bis(3-triethoxysilylpropyl) disulfide, TESPD, from Aldrich; antioxidant N-(1,3-dimethylbutyl)-N0-phenyl-p-phenylenediamine, 6PPD Santoflex-6PPD from Flexsys; stearic acid

Stearina TP8 from Undesa; N-cyclohexyl-2-benzothiazole sulfenamide, CBS, Vulkacit CZ/C from Lanxess; sulphur Creso from Redball Superfine; ZnO from Zincol Ossidi (wurtzite, BET specific surface area 5 $m^2$ $g^{-1}$).

### 4.2.2. Compounding and vulcanization of silica IR nanocomposites

Nanocomposite materials with different ZnO content (4.6, 2.50, 1.85, 1.20, 0.60, 0.25 parts per hundred rubber, phr), were prepared by mixing IR with suitable ratios of ZSO-7.7 and $SiO_2$ Zeosil MP1165, corresponding to a total amount of 40 phr $SiO_2$, in a Thermo Haake Reomix lab station internal mixer (250 mL mixing chamber, 0.7 filling factor).

Coupling agent TESPD (1.2 phr) and antioxidant 6PDD (0.62 phr) were also mixed. Sheets of about 2 mm thickness were obtained by 2 min mixing in an open two-roll mill. Nanocomposites were cured according to the following procedure. Firstly, stearic acid (0.62 phr) was added to the composite over 2 min and then the sample was mixed for 4 min. at 60 rpm with dumping at 140 °C. Successively, the other vulcanization reactants, i.e. S8 (0.9 phr) and CBS (0.48 phr), were added by mixing at 90 °C for 3 min in a two-roll mill (Table 4.1). Composites were further molded for 2 min to produce sheets of about 2 cm thick, suitable for the vulcanization. Curing profiles were measured with a Moving Die Rheometer (RPA 2000, Alpha Technological) under the following conditions: ±1° oscillation angle, 170 °C temperature, 4.3 bar pressure and 30 min running time. This analysis gave the optimum conditions for the curing. Hereafter, the cured samples will be called YZSO-IR, where Y indicates the ZnO content expressed in phr.

Reference master batches were also prepared following the same conditions reported for YZSO-IR by mixing IR with 40 phr of $SiO_2$ Zeosil MP1165 (Table 4.1). In this case, crystalline ZnO powder was conventionally added in the first step of vulcanization chemical mixing. Conventional cured reference samples will be labeled as M-YZSO-IR, where Y indicates the ZnO content expressed in phr.

The amounts of filler and ZnO utilized in the vulcanization procedure is reported in Table 4.1.

| Samples | IR | $SiO_2$ | ZSO-7.7 | C-ZnO |
|---|---|---|---|---|
| **1.85 ZSO-IR** | 100 | 32.89 | 7.70 | - |
| **1.20 ZSO-IR** | 100 | 35.39 | 4.99 | - |
| **0.60 ZSO-IR** | 100 | 37.69 | 2.50 | - |
| **0.25 ZSO-IR** | 100 | 39.04 | 1.04 | - |
| | | | | |
| **M-4.60 ZSO-IR** | 100 | 40.00 | - | 4.60 |
| **M-1.85 ZSO-R** | 100 | 40.00 | - | 1.85 |
| **M- 0.60 ZSO-IR** | 100 | 40.00 | - | 0.60 |

Table 4.1. Filler and ZnO loading of XZSO-IR and M-XZSO-IR nanocomposites (in phr)

## 4.3. Results and Discussion

### 4.3.1. Vulcanization of silica IR nanocomposites

The vulcanization curves (Appendix A.4.2.) for YZSO-IR nanocomposites, obtained by measuring the variation of viscosity over the time with the torque requested to keep the rotor at a constant rate, are reported in figure 4.1. a) Table 4.1. reports the curing parameters gained

from the vulcanization curves of YZSO-IR nanocomposites and also M-YZSO-IR nanocomposites. The minimum torque **ML** is the torque measured at the scorch time $\mathbf{t_{S1}}$, *i.e.* the time during which it is possible to manipulate the rubber composite before curing; the curing time $\mathbf{t_{MH}}$ is the time needed to achieve the complete curing of the composite; the maximum torque **MH** is the torque measured when the reticulation can be considered complete.

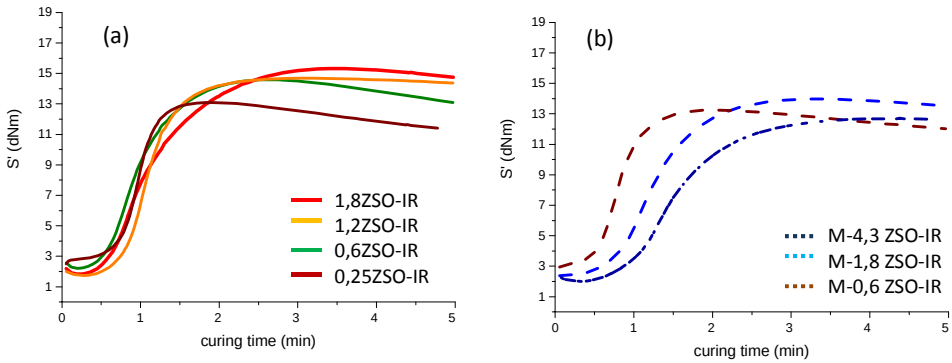


Figure 4.1. Vulcanization curves of a) 0.6ZSO-IR (—); 0.25ZSO-IR (—); 1.2ZSO-IR (—); 1.85ZSO-IR (—) and b) ofM-4,3ZSO-IR (---), M-1.80ZSO-IR(---), and M- 0.6 ZSO- IR(---).

The vulcanization curves of the composites curing with Y-ZSO and M-YZSO-IR were reported in figure 4.1. a) and 3.1. b). Y-ZSO evidence lower $\mathbf{t_{MH}}$ and higher **MH** than M-YZSO-IR though containing the same amount of ZnO. This suggests higher degree of rubber reticulation and more efficient curing mechanism in YZSO-IR composites.

The $\mathbf{t_{MH}}$ and the **MH** values increase with the zinc loading and become highest for the 1.85 ZSO-IR composite (Figure 4.1. a).

| Samples | Min Torque (ML) (kPa) | Curing time ($t_{MH}$) (min) | Max Torque (MH) (kPa) |
|---|---|---|---|
| 1.85 ZSO- IR | 1.7 | 3.2 | 15.3 |
| 1.20 ZSO- IR | 1.8 | 2.8 | 14.5 |
| 0.25 ZSO- IR | 2.2 | 2.5 | 14.5 |
| 0.6 ZSO- IR | 2.8 | 1.8 | 13.2 |
| M- 4.30 ZSO- IR | 2.5 | 5.0 | 14.8 |
| M- 1.80 ZSO- IR | 2.5 | 4.2 | 13.6 |
| M- 0.60 ZSO- IR | 2.5 | 2.3 | 13.1 |

Table 4.2. Curing parameters of YZSO-IR and M-YZSO-IR samples.

These outcomes demonstrate the higher curing efficiency in the presence of ZSO-X NPs. This is due to the better dispersion in the matrix, the small dimensions of particles and the weakening of the Zn-O bond energy due to Si-O-Zn interaction. These characteristics should favour an easier release of $Zn^{2+}$ ions compared to crystalline ZnO and the successive formation of the zinc-stearate complex and further sulfuring zinc-CBS complex formation along the curing process.

The dynamic-mechanical analyses of cured YZSO-IR and M-YZSO-IR composites were carried out in order to study the effect of the different

curing activation on the final properties of the material (Plots of G' *vs.* strain are shown in figure 4.2. a) and b).

The results show that the reinforcing effect of ZSO-X in all YZSO- IR samples is comparable with that in M-YZSO- IR containing the same amount of bare silica (40 phr).

This demonstrates that the amorphous ZnO NPs dispersed on the surface of silica leads to a storage modulus upshift to higher G' in YZSO-IR than in M-Y ZSO-IR composite.

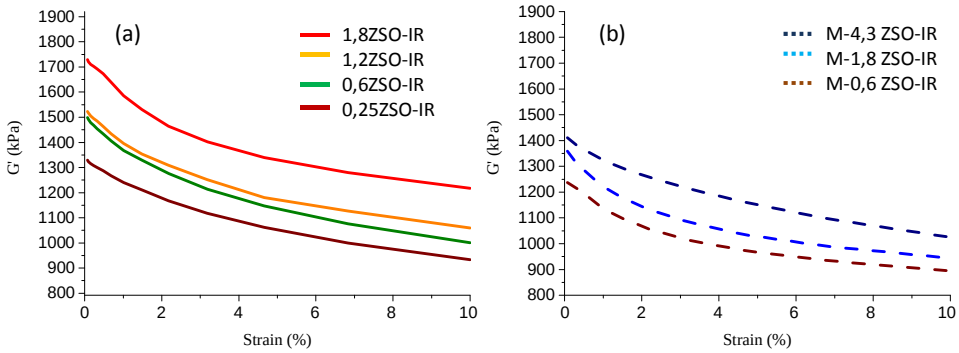


Figure 4.2. Storage modulus G' vs strain of cureda) 0.6ZSO-IR (—); 0.25ZSO-IR (—); 1.2ZSO-IR (—);1.85ZSO-IR (—) and b) ofM-4,3ZSO-IR (---), M-1.80ZSO-IR(---), and M- 0.6 ZSO- IR(---).

### 4.3.2. Cross-linking density of the YZO-IR and M-YZO-IR composite

Swelling experiments were also performed to evaluate the cross-link density of the cured nanocomposites, according the Flory-Rehner equation (2) in the Appendix A.4.1. The values for XZSO-IR and M-XZSO-IR samples are reported in figure 4.3. at different ZnO loading. The results demonstrate that in the investigated range of compositions, the reticulation degree increases with the ZnO content in both series of nanocomposites, until the maximum of 1.85 phr. The decrease at higher

ZnO loading was may be due to an imbalance with the other curing agents. However, XZSO-IR show cross-link densities higher than M-XZSO-IR, in the presence of comparable loading of ZnO. This is in agreement with the better curing efficiency of ZSO-X, compared to C-ZnO.

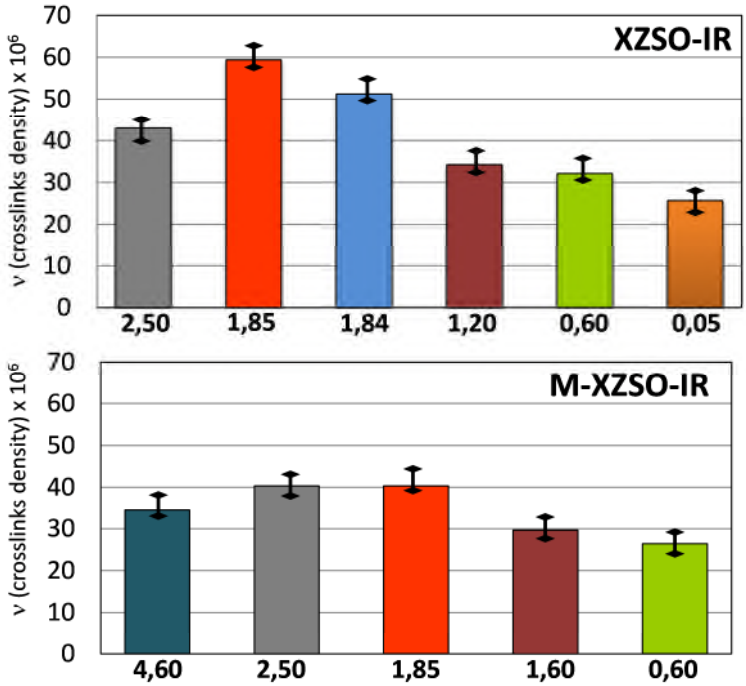


Figure 4.3. Cross-link density of cured XZSO- IR and M- XZSO- IR nanocomposites.

### 4.3.3. Apparent Activation Energy of curing process from Differential Thermal Analysis

The vulcanization processes of XZSO-IR and M-XZSO-IR were studied by a kinetic approach in non-isothermal conditions, using the Differential Scanning Calorimetry (DSC) (Appendix A.2.9.) at different heating rates

(5, 10 and 20 °C/min). DSC profiles of 1.85 ZSO-IR and M-1.85 ZSO-IR at 5 °C/min are shown as examples in figure 4.4.a) and b), respectively.

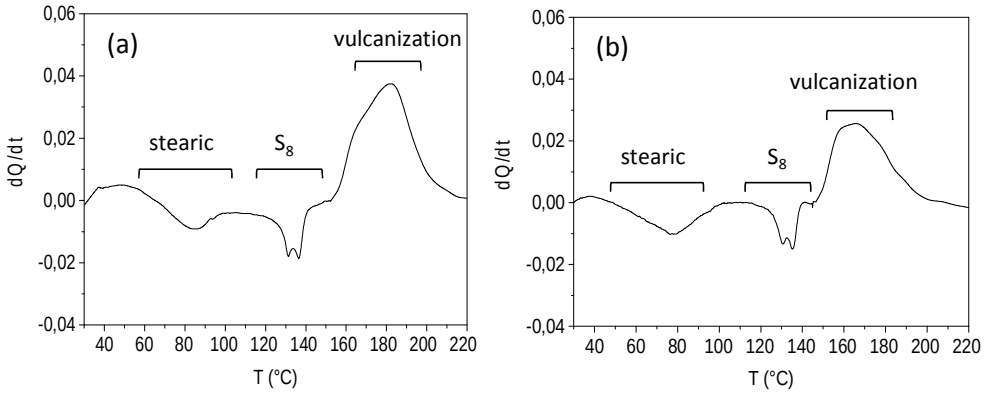


Figure 4.4. DSC profiles of a) 1.85 ZSO-IR and b) M-1.85 ZSO-IR at 5 °C/minheating rate.

DSC profiles of both nanocomposites show three endothermic peaks: at ~ 80 °C (melting of stearic acid), at 130 °C (partial reversion of polymeric sulfur to the molecular form) and at 136°C (melting of polymeric sulfur). Furthermore, it appears at T > 140 °C the exothermic bell-shaped peak due to the vulcanization process.

The vulcanization peak includes the enthalpic contributions of all the reactions involved in the sulfur curing process in the presence of activators and accelerators. Although it is not possible to determine the enthalpy of the single reactions, the peak can be divided in three main regions at increasing values of α[8] (see figure A.4. a) in Appendix A.2.9.): i) the induction period at the beginning of the process, where the activators and the accelerator react with sulfur forming the sulfuring complex and in turn with the rubber chains giving pre-crosslinking groups; ii) the curing period where the effective formation of the

sulphide network takes place and iii) the overcuring range which involves the last vulcanization reactions.

The apparent activation energy $E_\alpha$ of the different curing steps was calculated at different α from the linear plot of $ln\ \beta/T_i^2\ vs\ 1/T$ according to equation (7) in Appendix A.2.9.. The variation of $E_\alpha\ vs\ \alpha$ of all XZSO-IR and M-XZSO-IR samples are reported in figure 4.5. a) and b), respectively.

The trends of $E_\alpha$ are very different in the two cases whatever the ZnO loading. In fact, in the induction period the values of $E_\alpha$ of XZSO-IR are much lower than those of M-XZSO-IR. Along the curing, $E_\alpha$ values remain stable in both cases. In the last curing step the two processes again show an opposite trend, since the $E_\alpha$ values of XZSO-IR strongly increase while those of M-XZSO-IR decrease.

These results demonstrate that in the first step of the curing process, the reaction of ZSO-7.7 with the stearic acid and the successive formation of the sulfuring zinc complex with CBS and sulfur are accelerated compared to the curing with C-ZnO.

Besides the highest $E_\alpha$ in the last stage of XZSO-IR curing suggests that further reactions of the crosslinked rubber (overcuring) are more difficult than in M-XZSO-IR. Both evidences may be related to the more efficient curing mechanism of ZnO-10 and will be further discussed in the following.

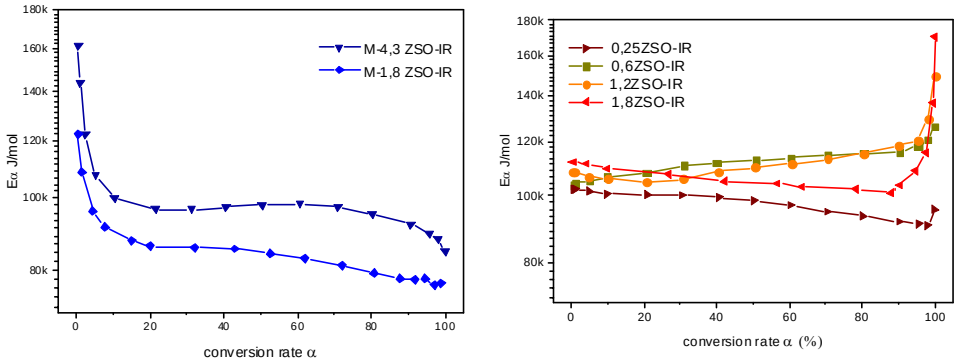


Figure 4.5.Plots of the apparent activation energy $E_\alpha$ *vs* the conversion degree $\alpha$ calculated by equation (7) of a) XZSO-IR and b) M-XZSO-IR nanocomposites.

### 4.3.4 Model compound vulcanization

The catalytic mechanism involving ZnO NPs anchored on silica (ZSO-7.7 sample), and in particular their role in the formation of the sulfur crosslinks, were investigated in the vulcanization of TME as model compound in accord with the procedure reported in appendix A.3.1. and analyzing the reaction products by LC-MS (see Appendix A.2.10.) and $^1$H-NMR. The results have been compared with those obtained using C-ZnO under the same reaction conditions.

The LC-MS analysis of the products obtained for ZSO-TME and C-ZnO-TME at 120°C after 20 minutes of reaction (the optimum curing reaction time) is reported in figure 4.6. a) and b) respectively.

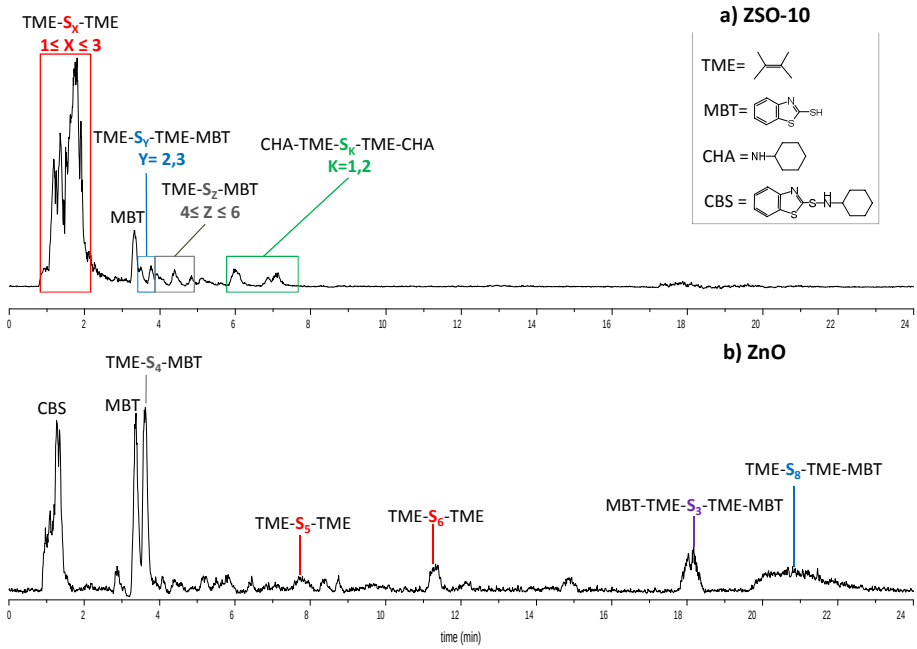


Figure 4.6. LC-MS chromatograms of a) ZSO-TME and b) C-ZnO-TME curing products after 20 minutes of reaction at 120°C.

The chromatogram mainly shows the formation of TME compounds crosslinked by short polysulfide ($S_1$, $S_2$, $S_3$) chains: i) in the range 1-2 minutes, the bad resolved group of peaks attributed to compounds whose molecular weights correspond to species with two crosslinked TME molecules (TME-$S_x$-TME with x=1-3); ii) in the range 3.4-3.8 minutes, the group of peaks due to species with two crosslinked TME molecules bound to mercaptobenzothiazole, MBT, (TME-$S_y$-TME-MBT with y=2-3); iii) at 3.8 and 4.9 minutes, the group of peaks ascribable to polysulphidic TME bound compound that can generate the free MBT; iv) at 5.7 and 7.4 minutes, the two peaks corresponding to species containing two crosslinked TME molecules linked to ciclohexylamine,

CHA, a by-product of CBS reaction (CHA-TME-$S_k$-TME-CHA with k = 1-2).

Species with longer polysulphide chains, which should be expected at longer retention time are instead completely absent at the optimum curing time (Figure 4.6. a).

However, it has to be noted that in the presence of ZSO-7.7, TME species crosslinked by long polysulfidic chains are evident at curing time shorter than the optimum one (< 20 minutes, figure 4.7).

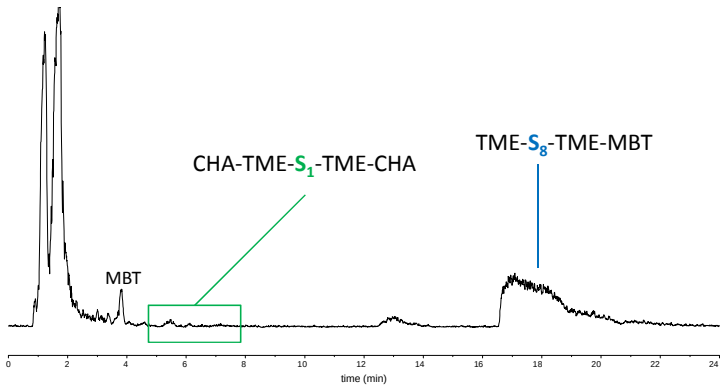


Figure 4.7. LC-MS chromatograms of ZSO-TME curing products after 15 minutes of reaction at 120°C

The analysis also evidences the presence of small amount of TME-$S_z$-MBT units with z = 4-6 between 3.9 and 5 minutes, generated by the reaction of polysulphide chains with MBT [24], which forms by partial degradation of CBS and whose peak is evident at 3.4 minutes. Other peaks between 0.9 and 1.6 min are due to CBS impurities.

The amount of a selected number of cured products using ZSO-TME as catalyst, varying the reaction time, was also determined by calculating the relative peak area of the mass spectra (figure 4.9). The peaks were preferentially selected among those not superimposed with the peaks of

other species. In particular, the amount of CHA-TME-$S_k$-TME-CHA, with k = 1, 2, as representative examples of the products crosslinked by short polysulfide chains, increases with time and reaches the maximum at the optimum curing time, and then it decreases (figure 4.8).

On the other hand, the species TME-$S_8$-TME-MBT, example of species crosslinked by long polysulfide chains evident at lower curing times, reaches the highest concentration after 15 min (figure 4.8) and then completely disappeared. This suggests that the high efficiency of ZSO-7.7 to produce short sulphide chains may involve also a possible breaking down mechanism of the longest polysulphide chains formed at the beginning of the cross-linking reaction [9, 10].

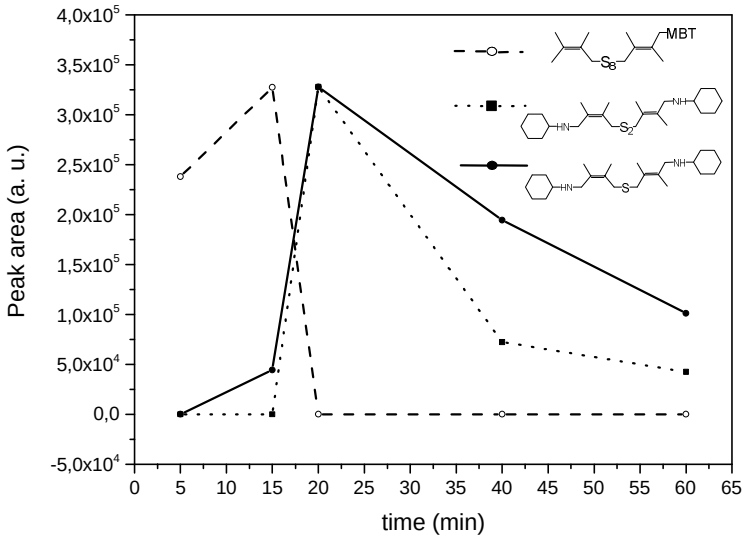


Figure 4.8. Amount of selected products detected by LC-MS as a function of reaction time of ZSO-TME cured at 120°C.

The LC-MS chromatogram of the reaction in the presence of microcrystalline ZnO, C-ZnO-TME, after the optimum curing time of 20 minutes is reported in figure 4.6. b).

The chromatogram showed peaks in the range $22 \geq t \geq 7$ minutes mainly attributable to species with molecular weights corresponding to products crosslinked by long polysulfide chains: TME-$S_5$-TME, TME-$S_6$-TME, TME-$S_8$-TME-MBT. The polysulphide chains are longer than those found in the case of ZSO-7.7 and peaks attributable to species crosslinked by di- and mono-sulphide chains are substantially absent.

The variation in the amount of selected products crosslinked by long polysuphides chains (TME-$S_5$-TME, TME-$S_6$-TME, TME-$S_8$-TME-MBT) *vs* reaction time are reported in figure 4.9. The amount of all selected species increases until 20 minutes, then decreases at longer reaction times, when the sulfide chains breakdown and shorten.

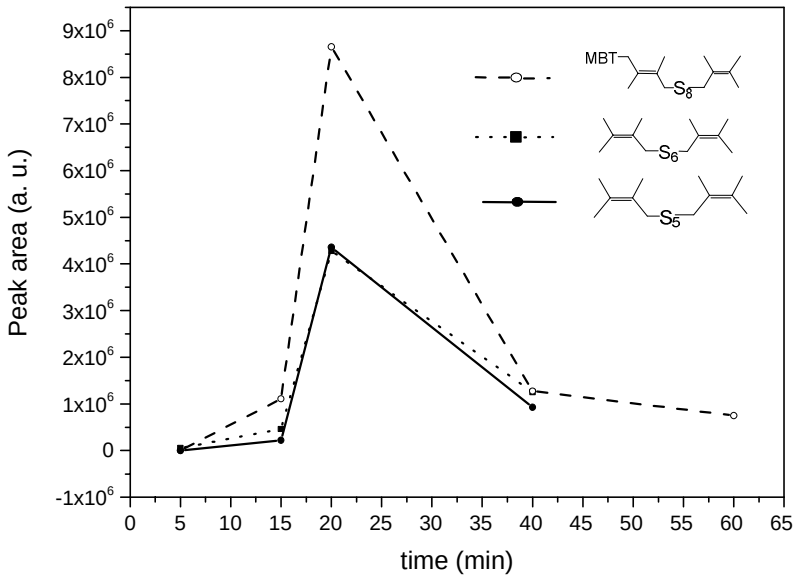


Figure 4.9. Amount of selected products detected by LC-MS as a function of reaction time of C-ZnO-TME cured at 120°C.

The products observed after TME curing in the presence of ZSO-7.7 and C-ZnO were studied by $^{1}H$ NMR spectroscopy, comparing the spectra with those of known reference compounds [7]. Figure 4.11 shows the $^{1}H$ NMR spectra of the ZSO-TME and C-ZnO-TME products obtained at 120 °C after 20 minutes of reaction.

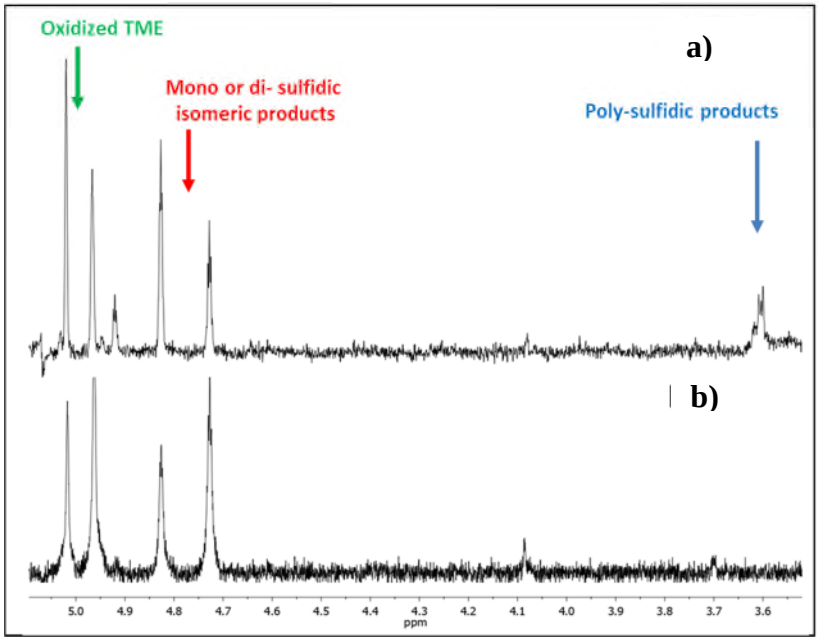


Figure 4.10. $^{1}H$-NMR spectra of a) C-ZnO-TMEand b) ZSO-TME after 20 minutes of reaction at 120 °C.

The $^{1}H$ NMR spectrum of C-ZnO-TME (figure 4.10. a.) shows the presence of polysulphide products. In fact the chemical shifts in the range of 3.7-3.4 ppm correspond to TME-$S_x$-TME products with x > 3; meanwhile no signal of the corresponding monosulphide TME-S-TME at 3.15 ppm is evident. The signals at 4.73 and 4.83 ppm can be related to the formation of isomeric crosslinked TME mono- or di-sulphide products, that arise via allylic substitution reaction during the curing

process [7]. Moreover, signals at 5.07 and 4.97 ppm may be associated to a partial oxidation of TME and to the formation of 2,3-butadiene [11].
C-ZnO-TME display also signals in the range of 8.0 and 7.33 ppm due to the aromatic hydrogen atoms of the MBT moieties linked to TME units, in agreement with the cross-linked products identified by LC-MS (figure 4.11).

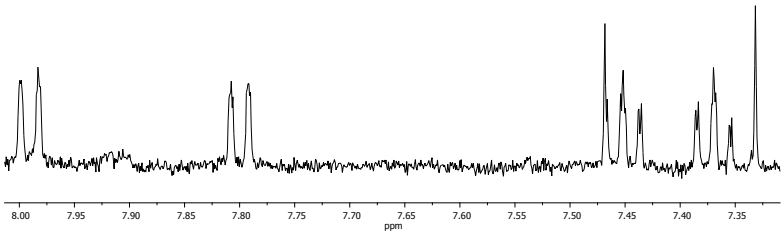


Figure 4.11. $^{1}$H-NMR spectra of C-ZnO-TME after 20 minutes of reaction at 120°C.

The ZSO-TME $^{1}$H NMR spectrum (Figure 4.10. b.) evidences at 4.73 and 4.83 the isomeric crosslinked TME mono- or di-sulphide products at 4.73 and 4.83 in larger amount than in ZSO-TME. Poly TME-$S_x$-TME products are completely absent, as observed in LC-GC.
The results of the MCV highlight that in the presence of ZSO-7.7 short sulphide chains are mainly obtained at the optimum curing time, instead C-ZnO stabilizes longer polysulphide chains ($S_5$,$S_6$, $S_8$). This result is in agreement with the higher crosslinking density calculated by the Flory-Rehner equation and can be related to the kinetics investigation which demonstrates that the $E_\alpha$ values in the induction vulcanization step are lower in the presence of ZSO-7.7 compared to C-ZnO, thus promoting a more efficient vulcanization.
Moreover, the highest $E_\alpha$ value in the last step of ZSO-TME curingsuggests that the more stable mono- and di-sulphide crosslinking

chains obtained in the presence of ZnO-10 make overcuring process more difficult than in the nanocomposites obtained by C-ZnO

### 4.3.5 FTIR analysis

FTIR analysis was performed on ZSO-TME and on C-ZnO-TME to investigate the interaction of ZnO with stearic acid and the successive reaction with CBS.

In figure 4.12., the ATR-FTIR spectra of ZSO-TME before and after the reaction with stearic acid are reported in comparison with the spectra of bare silica, in the range 800-1300 $cm^{-1}$. As discussed in the previous paragraph *2.3.4* the band at 954 $cm^{-1}$ attributed in bare $SiO_2$ to –Si-OH stretching vibration [12] (figure 4.12. c) shifts to higher frequency and becomes a shoulder at ~ 965 $cm^{-1}$ in ZnO-10 (figure 3.12. a), due to the co-presence of –SiOH and of the symmetric Si-O-Zn stretching vibration [20], After reaction with stearic acid the band at 965 $cm^{-1}$ back shifts still to 954 $cm^{-1}$ (figure 4.12. b). This indicates that the surface silanol groups are restored, suggesting that the zinc anchored to silica NPs was released after reaction with stearic acid.

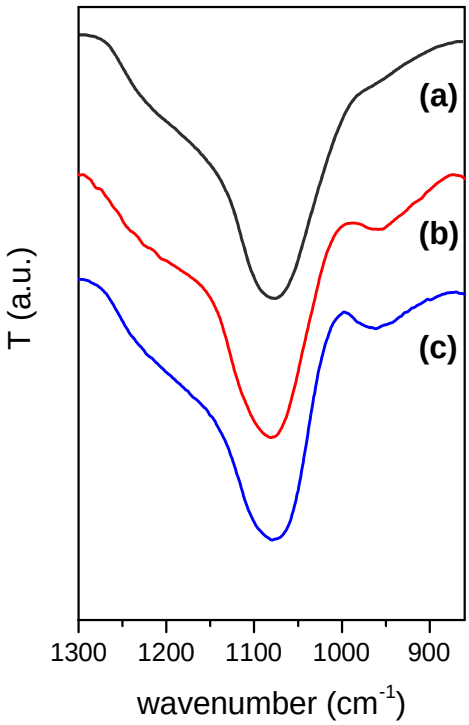


Figure 4.12. ATR-FTIR spectra of ZSO-TME a) before and b) after the reaction with stearic acid at 120°C; c) bare $SiO_2$.

FTIR analysis was performed also to investigate the reactivity of ZnO with the stearic acid and the subsequent reaction with the activator CBS. The reaction was carried out at 120 °C i) in the solid state following the sequence of mixing ZSO-7.7 or C-ZnO with stearic acid, then CBS; ii) in the presence of TME as model compound following the same mixing sequence. The relative amount of reagents is the same reported in the recipe of paragraph 2.6. Samples were put in a closed vessel or in a conical vial heated at 120 °C for 20 minutes, then quenched in liquid nitrogen to stop the reaction before recording FTIR spectra at room temperature.

In figure 4.13., the ATR-FTIR spectra in the range 1300 -1700 $cm^{-1}$ of ZSO-TME before and after the reaction with stearic acid and with CBS, are reported in comparison with those of C-ZnO-TME.

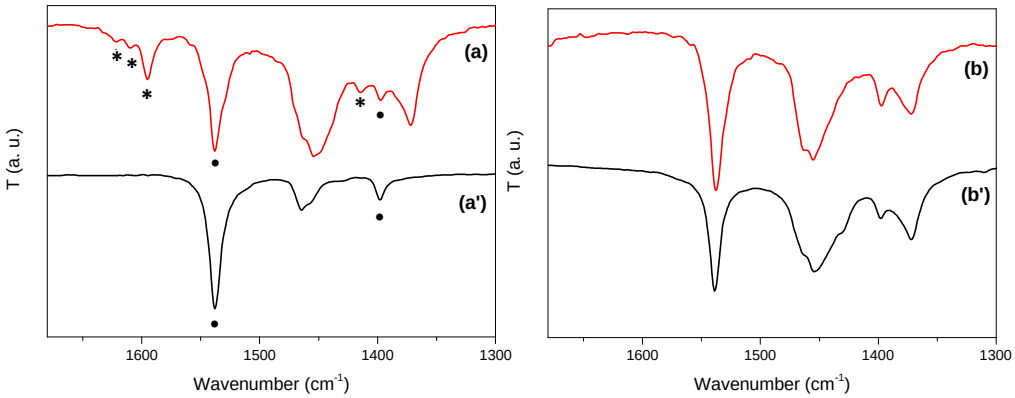


Figure 4.13. ATR-FTIR spectra of ZSO-TME (left) and C-ZnO-TME (right) after reaction with stearic acid at 120°C (a, b) and after the following addition of CBS (a', b').

After reaction with stearic acid, spectra of both ZSO-TME (figure 4.13. a) and C-ZnO-TME (Figure 4.13. b) show at 1538 $cm^{-1}$ and 1398 $cm^{-1}$(●in figure 4.13), the well known stearate antisymmetric and symmetric stretching vibrations [13] attributed to zinc distearate where four bridging carboxylate groups coordinate Zn(II) centers [14]. Surprisingly, ZSO-TME shows additional vibrations both in the region of the antisymmetric carboxylate stretching and of the symmetric ones, respectively at 1596, 1614, 1625 $cm^{-1}$ and at 1416 $cm^{-1}$ (* in figure 4.13). Other possible absorption bands in the region of symmetric vibrations may be hidden by the superimposition of the $-CH_2-$ scissoring vibration at 1464 $cm^{-1}$ and of the $C-H_2$ bending at 1454 $cm^{-1}$. The same carboxylate bands have been observed repeating the experiment in solid ZSO-7.7 without TME, where

in the absence of alkyl groups, another tentative symmetrical stretching band at 1434 $cm^{-1}$ was also observed (Figure 4.13. a).

In a recent work [15], Ikeda et al. deeply investigated the interaction of zinc with stearic acid in vulcanization conditions by experimental and theoretical approaches and demonstrated that at high temperatures, 140°C, a complex $(Zn_2(\mu\text{-}O_2CC_{17}H_{35})_2)^{2+} \cdot 4Y$ generates, having a 1:1 Zn: stearate molar ratio and roughly tetrahedral metal coordination. Its structure was postulated to be a bridging bidentate stearate complex where two carboxylate groups bridge two Zn(II) centers and the groups Y are $OH^-$, water and/or rubber segment (Figure3.14).

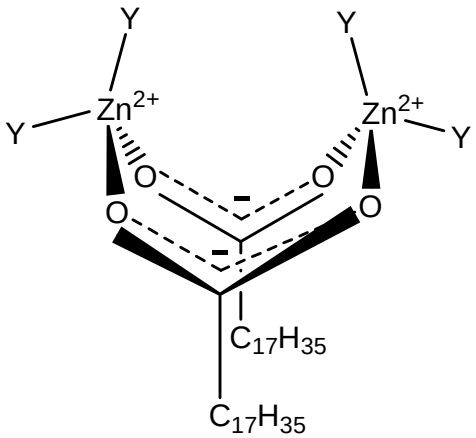


Figure 4.14. structure of the bridging bidentate complex $(Zn_2(\mu\text{-}O_2CC_{17}H_{35})_2)^{2+} \cdot 4Y$.

DFT calculations showed that depending on the different ligands, the complexes present different carboxylate vibrations. In particular the most stable species identified by Ikeda should have antysimmetrical stretching at 1596 $cm^{-1}$ and symmetrical one at 1434 $cm^{-1}$. This complex was suggested to be the most active intermediate in accelerating the sulfur cross-linking reaction of rubber.

The vibrational bands 1596 and 1434 $cm^{-1}$ observed in ZSO-TME after the reaction with stearic acid, perfectly agree with those of the stearate bridged species suggested by Ikeda [43]. The other less intense bands at 1614, 1625 and 1416 $cm^{-1}$ are more likely due to similar zinc stearate bridging complexes with different *Y* ligands [43].

It is noteworthy that these bridging bidentate complexes remain stable after quenching at room temperature the reaction of ZSO-TME with stearic acid performed at 140°C, and that they are absent if the reaction is performed in the presence of C-ZnO-TME.

Thus it may be suggested that the zinc centers of the amorphous ZnO NPs supported on silica in ZSO-7.7 favor the formation of the bridging bidentate complex. It can be suggested that since many surface zinc centers of these NPs are linked to silica through Si-O-Zn chemical bonds, Zn centers are hindered to coordinate four stearate ligands to assume the tetrahedral coordination. Instead, the bridging coordination of two zinc centers with two stearate is more favored. In this complexes Zn centers lie at a distance of about 4 nm [16], very similar to that of the well known active sites of several metalloenzymes containing Zn centers [17, 18].

ATR-FTIR spectra of ZSO-TME (figure 4.12. a') and C-ZnO-TME (figure 4.12. b') successively treated with the accelerator CBS at 120°C still showed the presence of the zinc stearate bands at 1538 $cm^{-1}$ and 1398 $cm^{-1}$ in both samples but no vibrational modes related to the stearate bridged bidentate zinc complex were observed. This clearly indicate that the bridging Zn compound reacts with the accelerator faster than the zinc stearate confirming the Ikeda hypothesis that this complex may play a role as an active intermediate to accelerate the cross-linking reaction [15].

This results suggest that the formation of this highly reactive zinc complex in the presence of ZSO-7.7 may explain the lower apparent activation energy of the induction stage of the vulcanization compared to C-ZnO.

### 4.4. Partial Conclusions

In this chapter the catalytic activity of silica anchored ZnO, ZSO-7.7, as curing activator in the sulfur crosslinking of IR was investigated in comparison with that of conventional microcrystalline C-ZnO. It has been demonstrated that it improves the curing efficiency compared to C-ZnO.

The high curing efficiency of ZSO-7.7 was explained by its ability to form sulfurating complexes at the beginning of reaction and the sulfur network in the final cured material. In fact, the values of the apparent activation energy $E_\alpha$ of the different steps of the vulcanization process, evaluated from differential thermal analysis measurements, demonstrated that in the induction period of curing the reaction of ZnO with the stearic acid and the successive reactions with the other curatives are kinetically favoured in the presence of ZSO-7.7 compared to the curing with C-ZnO.

Regarding the sulfur network formation, investigated by a MCV approach (Appendix A.2.10.), short crosslinking sulphide chains are mainly obtained in the presence of ZSO-7.7 unlike with C-ZnO which gives longer polysulphide chains ($S_5$, $S_6$, $S_8$). This explains the higher crosslinking density, calculated by the Flory-Rehner equation, in the XZSO-IR composites and their better curing efficiency. Moreover, the highest $E_\alpha$ in the last step of curing evidence that further reactions of the crosslinked rubber are more difficult in XZSO-IR than in YZnO-IR due

to the larger amount of more stable mono- and di-sulphide crosslinking chains.

In the first step of the curing reaction FTIR analysis suggests the formation of a stearate bridged bidentate zinc complex ($Zn_2(\mu\text{-}O_2CC_{17}H_{35})_2)^{2+}$.4Y. This is mainly promoted by ZSO-7.7 NPs and is highly reactive towards CBS and sulfur. In the presence of C-ZnO only a chelated stearate zinc complex was detected. $(Zn_2(\mu\text{-}O_2CC_{17}H_{35})_2)^{2+}$.4Y seems to be a possible effective intermediate in accelerating the cross-linking reaction and its formation in the presence of ZSO-7.7 NPs was associated to the constrain of tetrahedral geometry around the Zn when bound to silica.

---


[1] S.V. Vyazovkin, A.I. Lesnikovich, An Approach to the solution of the inverse kinetic problem in the case of complex process. Part I methods employing a series of thermoanalytycal curves, Thermochim. Acta 165 (1990) 273-280.

[2] S.V. Vyazokin, V.I. Goryachko, A.I. Lesnikovich, An approach to the solution of the inverse kinetic problem in the case of complex processes: Part III Parallel indipendent reactions, Thermochim. Acta 197 (1992) 41-45.

[3] Lautenschlaeger, F.K. Lautenschlaeger, K. Edwards, Model Compound Vulcanization—Part V. The Effect of Chemical Additives and Fillers, Rubber Chem. Technol. 53 (1980) 27-47.

[4] S. Rodriguez, C. Masalles, N. Agullo, S. Borros, L. Comellas, F. Broto, Identification of the Intermediates Sulfur Vulcanization of Natural Rubber, Kautschuk Gummi Kunststoffe 52 (1999) 438-445.

[5] M. Geyser, Geyser, W.J. McGill, Thiuram-accelerated sulfur vulcanization. II. The formation of crosslink precursors, J. Appl. Polym. Sci. 60 (1996) 431-437.

[6] M. Geyser, Geyser, W.J. McGill, Thiuram-accelerated sulfur vulcanization. I. The formation of the active sulfurating agent, J. Appl. Polym. Sci. 60 (1996) 425-430.

[7] P.J. Nieuwenhuizen, S. Timal, J.M.v. Veen, J.G. Haasnoot, J. Reedijk, Homogeneous Zinc(II) Catalysis in Accelerated Vulcanization I. Reaction-Stage Modeling and Cross-Link Formation, Rubber Chem. Technol. 71 (1998) 750-765.

[8] M. Lopez Manchado, M. Lopez, M.A. Lpez-Manchado, M. Arroyo, B. Herrero, J. Biagiotti, Vulcanization kinetics of natural rubber-organoclay nanocomposites, J. Appl. Polym. Sci. 89 (2003) 1-15.
[9] F.P. Baldwin, EPDM Vulcanization and High Temperature Compression Set, Rubber Chem. Technol. 43 (1970) 1040-1054.
[10] J. Hahn, Hahn, P. Palloch, N. Thelen, H.J. Weidenhaupt, Reversion Stable Networks with Polysulfide Polymers as Vulcanization Agents, Rubber Chem. Technol. 74 (2001) 28-43.
[11] P.J. Nieuwenhuizen, J.G. Haasnoot, J. Reedijk, Homogeneous Zinc(II) Catalysis in Accelerated Vulcanization II. (Poly)Olefin Oxidation, Dehydration, and Reaction with Anti-Reversion Coagents, Rubber Chem. Technol. 72 (1999) 15-26.
[12] M.G. Fonseca, A.S. Olivera, C. Airoldi, Silylating Agents Grafted onto Silica Derived from Leached Chrysotile, J. Colloid Interface Sci 240 (2001) 533-538.
[13] T. Ishioka, Y. Shibata, M. Takahashi, I. Kanesaka, Vibrational spectra and structures of zinc carboxylates II. Anhydrous zinc acetate and zinc stearate, Spectrochim. acta. Part A 54A (1998) 1811-1818.
[14] V. Zelenak, Zelenak, V. Zeleňák, Z. Vargová, K. Györyová, Correlation of infrared spectra of zinc(II) carboxylates with their structures, Spectrochim. acta. Part A 66A (2007) 262-272.
[15] Y. Ikeda, Y. Yasuda, T. Ohashi, H. Yokohama, S. Minoda, H. Kobayashi, T. Honma, Dinuclear Bridging Bidentate Zinc/Stearate Complex in Sulfur Cross-Linking of Rubber, Macromol. 48 (2015) 462-475.
[16] A. Susanna, L. Armelao, E. Callone, S. Dirè, M. D'Arienzo, B. Di Credico, L. Giannini, T. Hanel, F. Morazzoni, R. Scotti, ZnO nanoparticles anchored to silica filler. A curing accelerator for isoprene rubber composites, Chem. Eng. J. 275 (2015) 245-252.
[17] G. Schürer, T. Clark, R.v. Eldik, In The Chemistry of Organozinc Compounds; Rappoport, Z., Marek, I., Eds.; John Wiley Sons Ltd.: London, 2006; p 1.
[18] D. Dutta, S. Mishra, The structural and energetic aspects of substrate binding and the mechanism of action of the DapE-encoded N-succinyl-l,l-diaminopimelic acid desuccinylase (DapE) investigated using a hybrid QM/MM method, PCCP. Phys. Chem. Chem. Phys. 16 (2014) 26348-26358.

# Chapter 5

# Synthesis and characterization of MeO/$SiO_2$ NPs as vulcanization agent in the nanocomposite

The Chapter reports the synthesis and the catalytic activity of vulcanization activator as CaO and MgO NPs when are dispersed on the silica surface to obtain $MeO/SiO_2$ NPs (Me = Ca, Mg). The new two alkaline's double function fillers were prepared via hot-injection route and characterized by TGA and XRD. The chemical interaction between the metal oxide NPs and the silica was investigated by ATR-FTIR.

The curing efficiency was evaluated by dynamic mechanical proprieties of vulcanized $MeO/SiO_2$ nanocomposite and it was compared to those obtained by using powdered of microcrystalline CaO as activator in the curing process.

### 5.1. Metal oxides as activator for the rubber vulcanization

The possibility to use different metals oxide as curing activatorswere investigate in the course of time in order to find possible substitutes to zinc oxide. These metal oxides should have the capability to give an efficient vulcanization and to be easily available from the soil, and to be a low cost. Several authors tested different transition metals and alkaline earth metals in composite materials as curing activators. Among them copper, mercury, nickel, zinc, cadmium, indium, magnesium and calcium [1].

In the Chapter IV the importance of zinc(II) cations on the formation of stable complexes with the curing agents and the coordination between the cations and the ligands, during vulcanization were showed to have a direct influence on curing efficiency.

The ability of metal dication to form stable complexes was investigated by Irving and Williams in an experimental study. They

found that the stability order for the metal complexes formed by bivalent ions with organic ligands was[2] are :

$Cu^{2+}$, $Hg^{2+}$> $Ni^{2+}$, $Zn^{2+}$, $Cd^{2+}$, $In^{2+}$>$Mg^{2+}$, $Ca^{2+}$

The stability order was hold for nearly the same independently of the nature of the co-ordinate ligands or of the number of ligand molecules involved [2].

The Authors showedas the copper and mercury has strong coordinate ability to form organometallic-complex which decrease with the transition metal Ni, Zn, Cd and In, while the alkaline earth metal magnesium and calcium have slight tendency to form the same complexes.

The role of the formation of divalent cation complexes with curing agents was investigated by Ducháček [1]. He studied their activity of metallic stearates salts and their affinities with sulfur in natural rubber. Other authors proposed to study the affinity of metal oxides with the curing agents by model compound vulcanization and they correlate the ability of the metal dication to form stable complexes to the increase of the ultimate mechanical proprieties of the cured composites [3].

Where more stable metals dication given a vulcanization more efficent and kinetic favorable.

The ability of earth alkaline metals to form complexes and the disposition of the ligands around the metal center has been widely studied [2, 4-6].

Generally theyhave a redox-inactive propriety, so the bonding is essentially ionic without any directional interactions between the metal and the ligands[4].

The literature reports that Mg(II) shows well-defined octahedral coordination in aqueous solution, while calcium(II) has a much broader coordination number distribution with appreciable concentrations of $Ca^{2+}$ cations with six, seven, and even eight ligands at equilibrium. $Ca^{2+}$ is more influenced by the nature of ligands, with a coordinative bond distance much more variable around calcium(II) than magnesium (II). Analogous trends for the coordination geometry were observed with amids and carboxylates ligands. Therefore, a significantly greater variability in the ligand bond lengths and geometry of Ca(II) compared to Mg (II) occur [7, 8].

This behaviorhas been further investigated by V. Ducháček, which underlined that the comparable induction vulcanization time of calcium and magnesium stearate with the zinc stearate in natural rubber suggesting a fast vulcanization kinetic of the $Ca^{2+}$ and $Mg^{2+}$ as active vulcanization species[1].
Since the alkaline earth metals are not toxic several authors proposed them as alternative to zinc or in compresence with zinc in the vulcanization process, with particular attention to this possible capacity to decrease the curing time [3, 9].

Same Authors have proposed the synergic effect of hetero-activators coupling, between the alkaline earth metal with the zinc dication [9]. In particular, the combination of MgO-ZnO in a model compound

vulcanization showed as the magnesium activator has an apparent higher affinity forsulfur than Zn, but at the same time a decrease of the crosslinking density of the cured material with a prevalent formation of polysulfidic species was observed [3].

Magnesium and zinc cations have a similar charge/radius, smaller than calcium, but a different enthalpy of hydration for the $Zn^{2+}$ compared to the two alkaline earth metals. Thus, the zinc and magnesium has similar Lewis acid but different ability toform metal-hydroxide complexes[10].

In any case, it is not clear how the alkaline earth metals can form accelerator-activator complex during the curing time, due to their weak and predominantly ionic bonds. The same authors have partially explained this with the synthetic difficulties encountered in calcium and magnesium thiolate chemistry [11].

In this scenario, to create double filler function system, as well as in $ZnO/SiO_2$ NPs case, able to improve the dispersion in the rubber matrix of nanoparticles and increase the kinetic reactivity of the alkaline earth metal as curing activator of the calcium and magnesium can improve their low curing efficiency.

## 5.2. Synthesis of CaO and MgO nanoparticles

Alkaline earth metals have different chemistry compared to zinc, they are not amphoteric and it is not possible to obtain tri and tetrahydroxy species in basic solution, as reported in the Chapter III for zinc. Thus, asynthetic approach different from the sol-gel method must be considered able to give Ca and Mg nanoparticles anchored on bare silica nanoparticles.

In supersaturation synthesis condition the formation of small nanoparticles is supported by the decrease of the nucleation limits with the consequent growth of nanoparticles [12].

The principle of the supersaturation is based on the Gibbs-Thomson effect which considers that particles with radius smaller than the critical radius dissolve because they are thermodynamically instable [13]. When the nanoparticles radius is lower than the critical radius ($r_c$), the growth rate is stable enough to increasethe particles dimension (see figure. 4.1) [14].

In a diffusion controlled process, the surface reaction rate is acceleratedand consequentially maximum growth rate ($r_{max}$) shift to smaller particles radius:

$$r_c = \frac{2\gamma V_m}{RTlnS} \qquad (1)$$

where $\gamma$ is the surface free energy per unit area, $Vm$ is the molar volume of the monomer in particles, $S$ is the concentration level of supersaturation, $T$ the temperature and $R$ is the gas constant.

The most important factors of a colloidal synthesis are the size distribution the nucleation and diffusion.

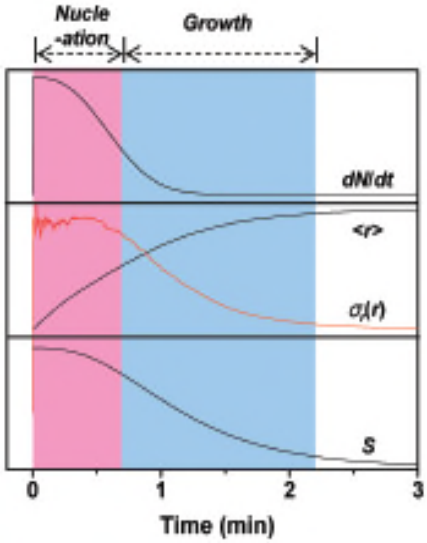


Figure 5.1. *N, σ* r (r*)*, <*r* >, and *dN*/*dt* are the number concentration of the nucleated nanoparticles, relative standard deviation of their radii, the mean radius, and the nucleation rate, respectively. Areas colored with red and blue. Correspond to the nucleation and the growth periods, respectively

Thus, in the supersaturation conditions it is possible to obtain low critical radius and high surface energy.

The high supersaturation level promotes both homogeneous nucleation and nanoparticles growth. The hot-injection approach works in supersaturation condition, thus permitting to obtain high controlled nanoparticles size and shape. In this thesis, this method is proposed as a synthetic route for the formation of metal oxide NPs grown on silica surface by hydrolysis and condensation reactions [15].

## 5.3. Preparation of $CaO/SiO_2$ and $MgO/SiO_2$

### 5.3.1. Reactants and materials

$MeO/SiO_2$ synthesis: precipitated silica Rhodia Zeosil MP1165 (BET specific surface area 160 $m^2$ $g^{-1}$); $Ca(NO_3)_2 4H_2O$ (99.99 %) and $Mg(NO_3)_2 4H_2O$ (99.99 %) from sigma-aldrich; NaOH (98 %) from Fluka; anhydrous ethylene glycol (99.8%) from sigma-aldrich.

### 5.3.2. Synthesis procedure

The hot-injection synthesis of $CaO/SiO_2$ and $MgO/SiO_2$ follow similar procedures.

Suitable amount of calcium or magnesium nitrate tetrahydrate precursor (see Table 5.1) was introduced in 125 ml of ethylene glycol under $N_2$ (g) bubbling in order to remove the undesired gas as $CO_2$.

When all the metal nitrate precursor was dissolved, 3 g of silica was introduced in the reaction mixture and the temperature increased at 150 °C. Then 10 ml of a 5.17 M NaOH solution in water was rapidly injected by syringe in the solution containing silica. The final solution was immediately pumped in a ceramic membrane filtered and washed several times by ethanol (figure 5.2).

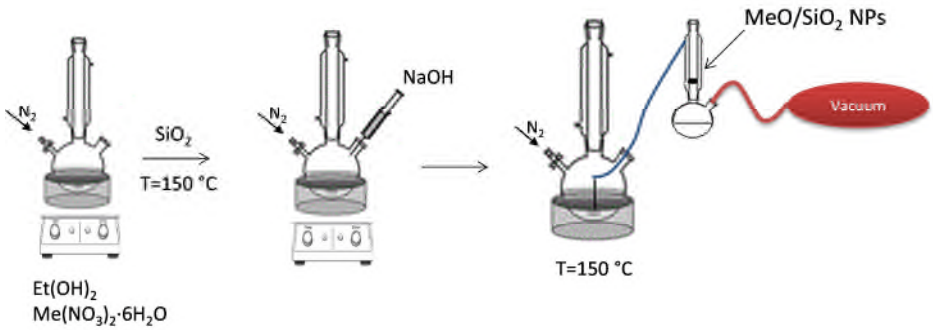


Figure 5.2. Experimental set-up for the synthesis of $MeO/SiO_2$ NPs by hot-injection route.

Different loading of MeO has been grown on the silica nanoparticles (Table 5.1). They will be labeled CSO-X and MSO-X respectively for calcium and magnesium, where X refers to the actual amount of MeO on $SiO_2$ in wt%.

| **Sample name** | **$Ca(NO_3)_2 4H_2O$ (mmol)** | **$SiO_2$ (mmol)** | **NaOH (mmol)** | **CaO (wt%)** |
|---|---|---|---|---|
| **CSO-73** | 74,10 | 24,96 | 51,75 | 73 |
| **CSO-25** | 9,26 | 24,96 | 51,75 | 25 |
| **CSO-14** | 4,63 | 24,96 | 51,75 | 14 |
| **CSO-4** | 1,15 | 24,96 | 51,75 | 14 |
| **Sample name** | **$Mg(NO_3)_2 4H_2O$ (mmol)** | **$SiO_2$ (mmol)** | **NaOH (mmol)** | **MgO (wt%)** |
| **MSO-8** | 2,3 | 24,96 | 51,75 | 7,9 |
| **MSO-4** | 1,15 | 24,96 | 51,75 | 4.0 |

Table 5.1.Synthesis of MeO NPs grown on silica, CSO-X and MSO-8.

### 5.4. Morphological and structural characterization of $CaO/SiO_2$ and $MgO/SiO_2$

The chemical and structural characterization of $CaO/SiO_2$ and $MgO/SiO_2$ powders were investigated by TGA and XRD, in connection with chemical phases and structure. While the chemical interaction between the alkaline earth metals and $SiO_2$ was investigated by ATR-FTIR and NMR techniques.

### 5.4.1 Thermogravimetic analysis (TGA)

TGA analysisof the CSO-X and MSO-8 powder is aim to evaluate the effective amount of $Me(OH)_2$ and $MeCO_3$ grown on the $MeO/SiO_2$ nanoparticles, the analysis was performed at the temperature range of 25 – 800 °C with a heating rate of 10 °C/min (Appendix A.2.8.).

The weight losses are in accordance with the dishydratation of $Ca(OH)_2$, in the temperature range 410-440 °C, and decarboxylation of $CaCO_3$, temperature range 600-700 °C (See figure 5.3).

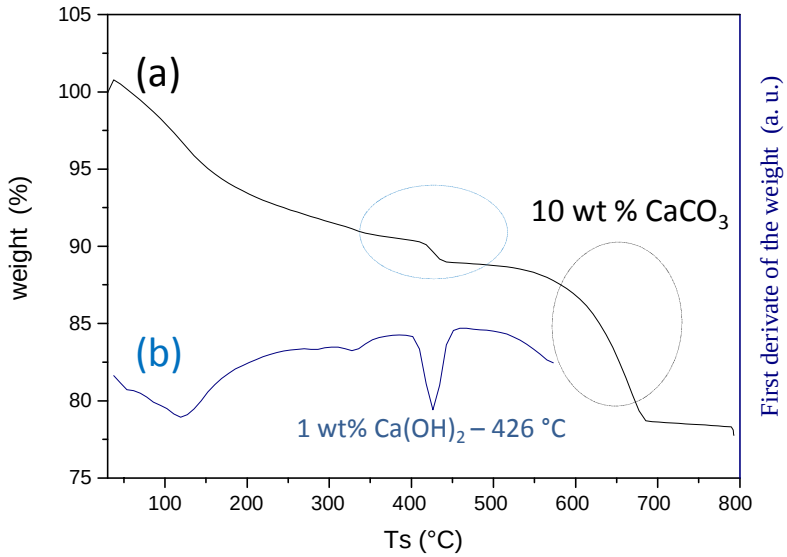


Figure 5.3.TGA (a) and first derivate of TGA (b) analysis of CSO-25 sample evidences the dishydratation and decarboxylation process.

The TGA analysis permit to identified the contribution of $Ca(OH)_2$, that correspond to a weight loss between 410-440 °C (figure 5.3. a), with the first derivate of the TGA (figure 5.3. b) indicates a maximumat 426 °C, with a weighting loss of 1 wt%. By the TGA

profile was also possible to recognize the $CaCO_3$ decarboxylation between 580 °C and 680 °C, with a weighting loss of the 10 wt%.
The synthesis of pure calciumoxide and hydroxide is difficult due the energetic favorable formation of carbonate phases [16].

$$Ca(OH)_2 + CO_2 \rightarrow CaCO_3 + H_2O + 74\ kJ/mol$$

The sample CSO-75, CSO-25, CSO-14, CSO-2 showed a presence of $Ca(OH)_2$ with a weight loss between 3 and 1 %, while the amount of $CaCO_3$ was 10, 9 and 5 % respectively, while the sample CSO-2 didn't showed presence of carbonates (Table 5.2).
The TGA of the MSO-8 showed a main contributions of $Mg(OH)_2$, the DTA underline the maximum peak at 430 °C (figure 5.4. b.) with a weighting loss of the 5 wt% due to the sample dishydratation, and without presence of the carbonate phase (See figure 5.4. a.).

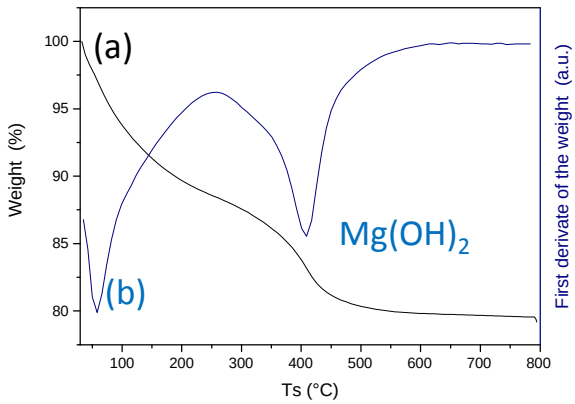


Figure 5.4.TGA (a) and first derivate of TGA (b) analysis of the MSO-8 sample. The first derivate with the peak at 430 °C due to $Mg(OH)_2$ dishydratation.

Both the TGA profile of the samples CSO-X and MSO-8 showed slight weighting decrease for all the heating profile, this is due to the dishydratation of the silica nanoparticles.

The table 5.2. reported the weight losses of the simples analyzed.

| Sample name | Dishydratation loss range | Dishydratation weight losses | Carboxylate loss range | Carboxylate weight losses |
|---|---|---|---|---|
| **CSO-73** | 25-200 | 3 | 320-610 | 10 |
| **CSO-25** | 410-440 | 1 | 580-680 | 9 |
| **CSO-14** | 340-360 | 1 | 590-690 | 5 |
| **CSO-4** | 450-650 | 2 | -- | -- |
| **MSO-8** | 380-500 | 5 | -- | -- |

Table 5.2. TGA analysis on the samples CSO-X and MSO-8

The TGA results were in good accordance with the amount of calcium and magnesium anchored on silica nanoparticles detected by ICP analysis (not reported).

### 5.4.2. Structural analysis of CSO-X and MSO-8

The XRD analysis showed an amorphous structure for all the CSO-X independent of Ca loading on the bare silica (not reported), except for the CSO-73 with the more high CaO loading, it showed a slight reflections of the calcium hydroxide phase, with the characteristic signals of the calcium hydroxide crystal with the lattice fringes of the (001) and (101) at 2θ of18° and 33°respectively [17] (figure 5.5).

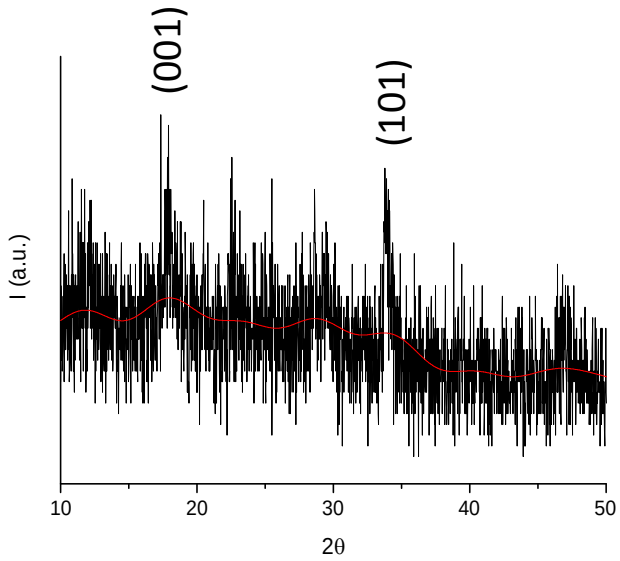


Figure 5.5. The XRD patterns of the amorphous CSO-73 sample.

While, the MSO-8 sample showed an amorphous phase with the presence of the broad peak of the $SiO_2$ (not reported).

### 5.4.3. Si-O-Me characterization by ATR-FTIR

The bond interaction between $SiO_2$ and CaO in CSO-X was studied by ATR-FTIR with the same methodology reported in paragraph 3.3.4. The CSO-X spectra (figure 5.6) reporting the broadening of the Si-O-Si asymmetrical (1072 $cm^{-1}$) and symmetrical (804 $cm^{-1}$) stretching vibrational modes. In the CSO-X sample the asymmetrical and symmetrical stretching shift to lower energy, 1055 $cm^{-1}$and 794 $cm^{-1}$ respectively, this is associated to a partial substitution of Si-O-Si group with a Si-O-Ca covalent bond. That was also proved by the band at 954 $cm^{-1}$ which in bare $SiO_2$ spectrum was the –Si-OH

stretching vibration, this group given a gradually the formation of Si-O-NBO groups, non-bridging oxygen (NBO), with an equivalent shift of the Si-OH peak to higher energy (CSO-4 to 961 $cm^{-1}$, CSO-14 to 969 $cm^{-1}$ and CSO-25 to 968 $cm^{-1}$). The calcium is incorporated easily in the silica with the formation of $Ca^{2+}$ ions groups contained in the silica structure, as proved by several authors in the glass layers [18, 19].

In this scenario, the ATR-FTIR analysis of the samples CSO-4, CSO-14 and CSO-15 reported also the gradual increase of the signals at 873 $cm^{-1}$, in figure 5.6. (●), and at 1410 $cm^{-1}$ proportional to the rise of the calcium loading, with a splitting in two bands at 1465 and 1409 $cm^{-1}$ in CSO-25 sample, attributed to the formation of calcium carbonate and hydroxide phases.

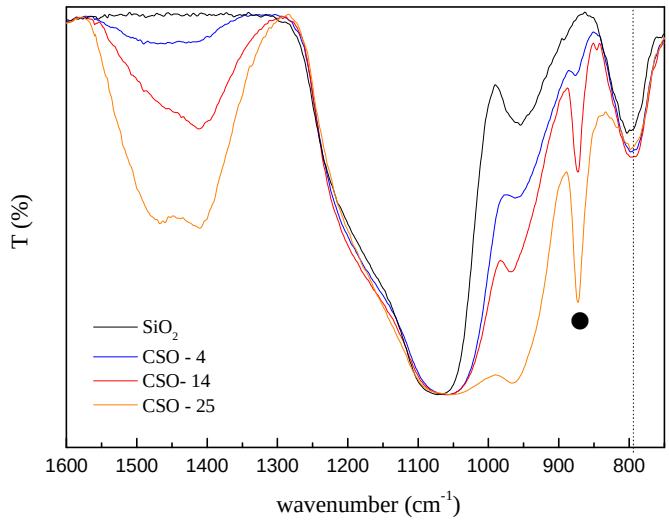


Figure 5.6. ATR-FTIR spectra of $SiO_2$ (—), CSO-4 (—), CSO-14 (—) and CSO-25 (—).

The ATR-FTIR analysis of the MSO-8 sample showed, as in the sample CSO-14, a broadening and shifting of Si-O-Si asymmetric and symmetric stretch (1072 $cm^{-1}$ and 804 $cm^{-1}$) to lower energy1055 $cm^{-1}$ and 793 $cm^{-1}$ respectively. Moreover, the sample given a signal at 880 $cm^{-1}$ in figure 5.7 (●), attributed to the $Mg(OH)_2$ phase. Otherwise, the Si-OH stretching vibration become a shoulder in agreement with a partial substitution of the silanol groups with a Si-O-Mg covalent bound, as seen in the Si-O-Zn bond (paragraph 3.3.4.), without any evidence of the incorporation of the magnesium as confirmed by the absence of Si-O-NBO group signals [20]. That proved the higher perturbative nature of the $Ca^{2+}$ ionsinserted in the silica structure compared to the $Mg^{2+}$.

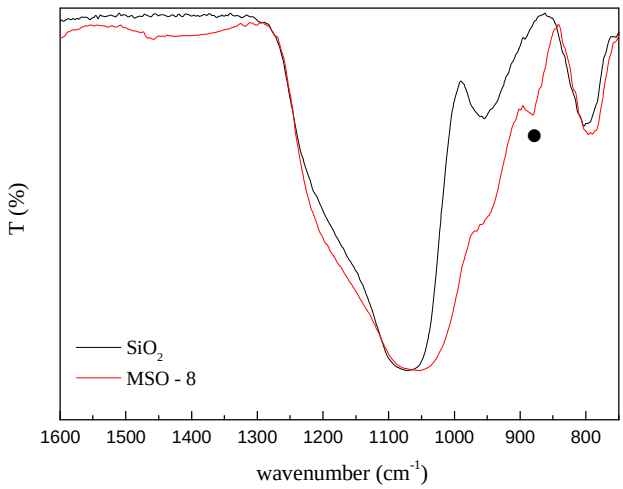


Figure 5.7. The ATR-FTIR spectra of $SiO_2$ (—) and MSO-8 (—).

## 5.3. Mechanical characterization of the CSO-X/IR and MSO-8/IR nanocomposite

Cured nanocomposites containing $CaO/SiO_2$ and $MgO/SiO_2$ were prepared following a procedure similar to that reported in paragraph 4.2.2 for $ZnO/SiO_2$.

Nanocomposites were labelled CSO-W/IR, where W indicates the amount of CSO-73 or CSO-14 NPs and MSO-Z/IR, where Z indicates indicate the number of MSO-8 NPs. The samples were compared with M-YCaO-IR composites, where Y indicates the microcrystalline CaO content expressed in phr, prepared by using macrocrystalline CaO as reported in Table 5.3.

| **Composite** | **IR** | **$SiO_2$** | **CSO-73** | **CaO** |
|---|---|---|---|---|
| CSO – 4,6/IR | 100 | 38.5 | 6,2 | - |
| | | | **CSO-14** | |
| CSO – 1,0/IR | 100 | 33,5 | 7,8 | - |
| CSO – 0,5/IR | 100 | 37,0 | 3,4 | - |
| CSO – 0,3/IR | 100 | 38,1 | 1,9 | |
| | | | **MSO-8** | |
| MSO – 1,0/IR | 100 | 28,4 | 12,6 | - |
| MSO – 0,3/IR | 100 | 36,3 | 4 | - |
| M-1,0CaO-IR | 100 | 40.0 | - | 1 |
| M-0,5CaO-IR | 100 | 40.0 | - | 0,5 |

Table 5.3. Filler and MeO loading of MSO-X/IR, CSO-X/IR and M-XCaO-IR nanocomposites (in phr).

Figure 5.8. shows the comparison between M-0,5CaO-IR and M-1,0CaO-IR and CSO – 0,5/IR, and CSO – 1,0/IR, containing CSO-14 as curing agent and CSO – 4.6/IR with CSO-73, another composite without any activator of vulcanization, ZnO 0 phr, was also prepared.

The vulcanization curves of the CSO – X/IR nanocomposite show an increase of mechanical proprieties with the increase of CaO loading, corresponding to a decrease of $t_{MH}$ and similar or higher MH, in the case of highest calcium loading in comparison with the composite at zero phr of ZnO. In no case CSO – X/IR shows a higher MH or lower $t_{MH}$ compared to the reference M-XCaO-IR. This may actually be due to the high amount of inactive $CaCO_3$ phase, then to a lower release of the $Ca^{2+}$.

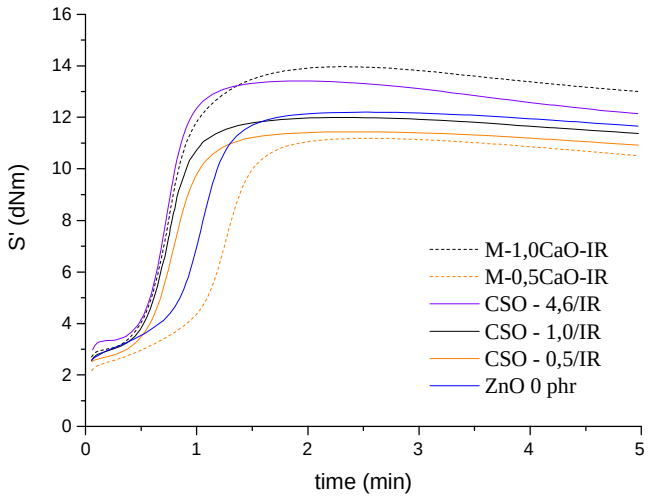


Figure 5.8. Vulcanization cures of M-1,0CaO-IR (---), M-0,5CaO-IR (---) and CSO-4,6/IR (—), CSO-1,0/IR (—), CSO-0,5/IR (—) and ZnO 0 phr (—).

The dynamic-mechanical analysis of the cured CSO-X/IR and M-XCaO-IR composites were carried out in order to study the effect of calcium as curing activator on the final proprieties of the material.

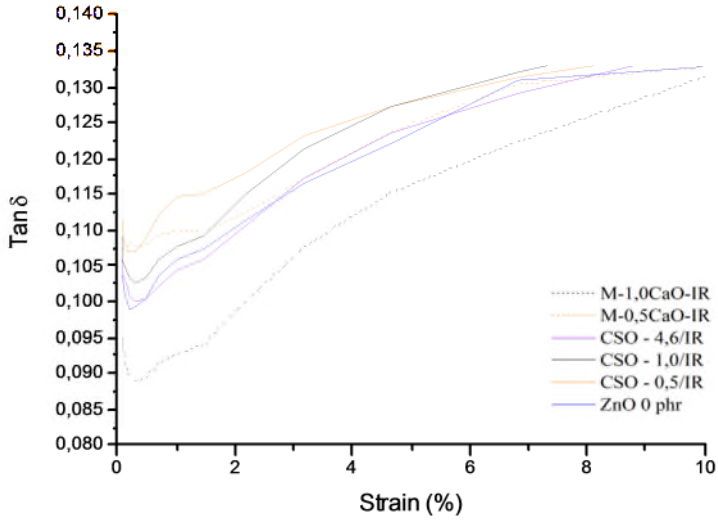


Figure 5.9. Storage modulus Tan δ vs strain of cured M-1,0CaO-IR (----), M-0,5CaO-IR (---) and CSO-4,6/IR (—), CSO-1,0/IR (—), CSO-0,5/IR and ZnO 0 phr (—).

The figure 5.9. shows, according to the vulcanization curves, a strain sweep (Tan δ vs strain, see Appendix A.4.2.) comparable with a sample without any activator of vulcanization (ZnO 0 phr) which leads to a high hysteresis of the composite and to poor mechanical proprieties, with low crosslinking density and a modest sulfur network.

The vulcanization curves of the nanocomposite cured with MSO-8 are show in figure 4.10, where MSO – 1,0/IR and MSO – 0,3/IR are compared, respectively, with CSO- 1,0/IR and CSO – 0,3/IR and with

ZnO 0 phr composites. All samples show mechanical proprieties similar to nanocomposite without activator of vulcanization. Anyway MSO – X/IR evidenced longer $t_{MH}$ than CSO – X/IR composite containing the same amount of activator and MSO – 1,0/IR composite shows the highest MH even if their catalytic activity is confirmed to be much lower than ZnO (see paragraph 4.3.1. figure 4.1).

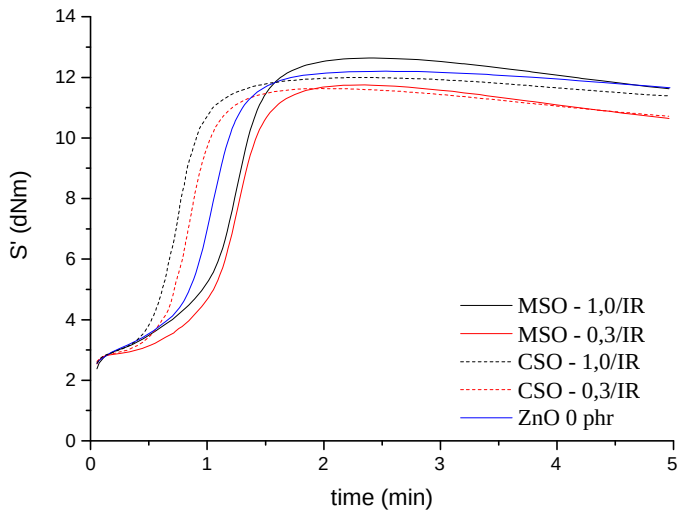


Figure 5.10. Vulcanization cures of MSO-1,0/IR (—), MSO-0,3/IR (—) and CSO-1,0/IR (---), CSO-0,3/IR (---) and ZnO 0 phr (—).

Besides nanocomposites cured with the MSO-8 gives a slight increase of the mechanical proprieties and proportional to the MgO loaded.

The DMA of the cured MSO-X/IR and CSO – X/IR show a slight decrease in the hysteresis of the MSO – X/IR nanocomposite, with a downshift of the Tan δ curves proportional to the magnesium loading, confirmedthe more efficient role of the magnesium as crosslinking agent.

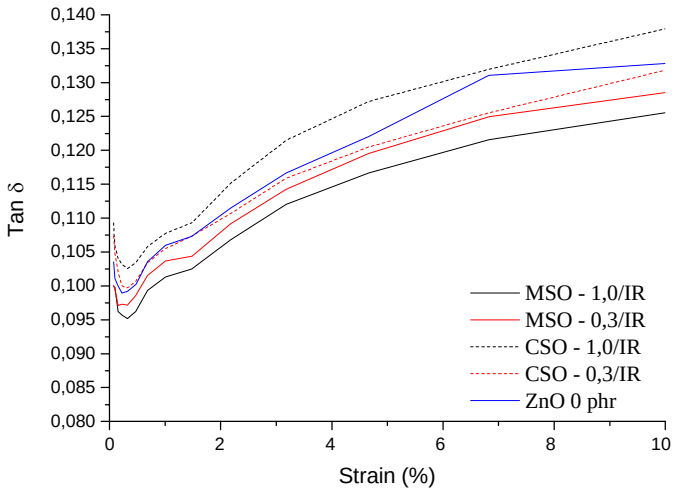


Figure 5.11. Storage modulus Tan δ vs strain of cured MSO-1,0/IR (—), MSO-0,3/IR (—) and CSO-1,0/IR (---), CSO-0,3/IR (---) and ZnO 0 phr (—).

The results show that the reinforcing effect of the MSO-8 in all the MSO-X/IR samples is higher than in the case of CSO-X/IR and the sample without any activator of vulcanization but containing the same amount of bare silica (40 phr). This demonstrates a slight role of the MgO as activator of vulcanization, the more efficiency of the magnesium compared to the calcium also at lower loading in the nanocomposite confirmed the easer ability of magnesium to give higher mechanical proprieties, may be due to similar charge/radius ratio between Mg and Zn dications.

### 5.3.2. Cross-linking density

The cross-link density of the cured nanocomposite was evaluated by swelling measurements according the Flory-Rehner equation (see Appendix A.4.1.).

The values for CSO-1,0/IR, M- 1,0CaO-IR, CaO-0,7/IR (discussed in paragraph 5.5.1.), MSO-1,0/IR, and MSO-0,3/IR nanocomposites are reported in figure 5.12.

The results confirm a lower crosslinking degree of all samples compared to ZSO-X (chapter IV, figure 5.3) as proved by the lower mechanical proprieties showed in the previous paragraph. Within error bar, calculated by three rapture measurements, they have a similar crosslinking for all the sample. In the case of calcium, the cross-linking density is independent ofthe activator loading, while for the magnesium a slightly higher crosslinking occurs with the increase of MgO. In any case, the alkaline earth metals confirm the low tendency to be a good vulcanization activator compared to ZnO.

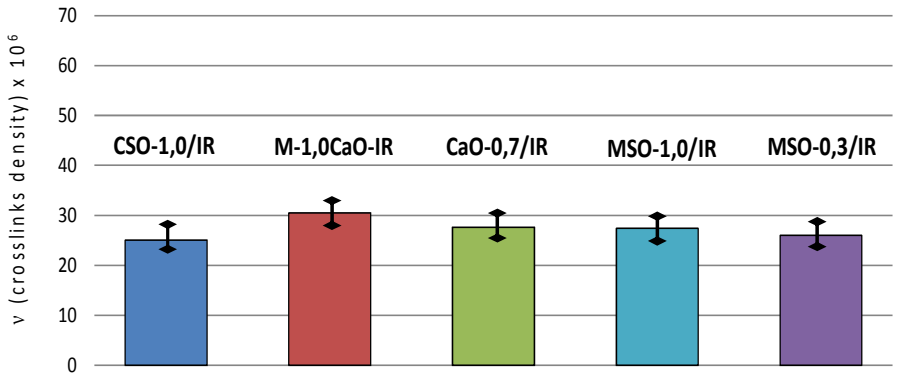


Figure 5.12. Cross-link density of cured CSO-1,0/IR (■), M- 1,0CaO-IR (■) CaO-0,7/IR (■) MSO-1,0/IR (■) and MSO-0,3/IR (■) nanocomposites.

## 5.4 Model compound vulcanization

The catalytic role of CaO and MgO NPs anchored on silica (CSO-14 and MSO-8sample) in the vulcanization process and in the formation

of the sulfur crosslinks, were investigated, as in paragraph 4.3.4, by the MCV and analyzing the products by LC-MS. The results were compared with those obtained for ZSO-10 in the same reaction conditions.

The LC-MS analysis of the products obtained for CSO-TME and MSO-TME at 120 °C after 20 minutes of reaction (the optimum curing reaction time) is reported in Figure 5.13. a) and b).

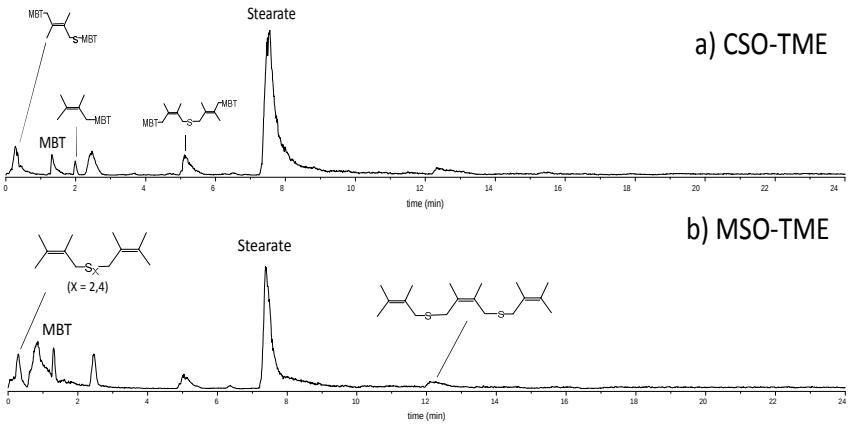


Figure 5.13.LC-MS chromatograms of a) CSO-TME and b) MSO-TME curing products after 20 minutes of reaction at 120°C.

The chromatogram in the figure 5.13. a) mainly showed at 7.5 minutes the presence of unreacted stearic acid peak, this indicates that the metal-stearate complex hardly formed in the MCV of CSO-TME, consequently giving a low level of crosslinking. No crosslinker precursors were detected, except a monosulfur crosslinker bond with two molecules of mercaptobenzothiazole revealed at 5.2 minutes. Otherwise in the chromatogram a group of peaks ascribable to subproducts correlated to an inefficient vulcanization are present, whichdo not giveany reinforcement of the composites.

Also in MSO-TME (figure 5.13. b.) the peak of the stearate anion is present, but in this case is possible to recognize at 0.3 minutes also the crosslinked products TME-Sx-TME (X = 2,4) and at 12 minute the crosslinked TME structure TME-S-TME-S-TME. In any case, MSO-8 gives just a partial crosslinking without any crosslinking distribution or crosslinker precursors. This allows to consider also the magnesium a poor curing activator.

## 5.5. Morphological and structural characterization of the CaO NPs

The curing efficiency of the alkaline earth metals in the vulcanization were further tested by using primary CaO nanoparticle not supported on silica.

In order to investigate the CaO NPs activity prevent the negative effect of the Ca dication incorporation into the silica structure during the synthesis process (see paragraph 5.4.3.)

CaO particles with a specific surface of 75 $m^2/g$ (calculated by BET) was synthetized by the same experimental route of the CSO-X and MSO-X, and structural and morphological characterized the used as curing activator in the nanocomposite.

The CaO NPs purity was carry on also in this case by TGA analysis (figure 5.14).

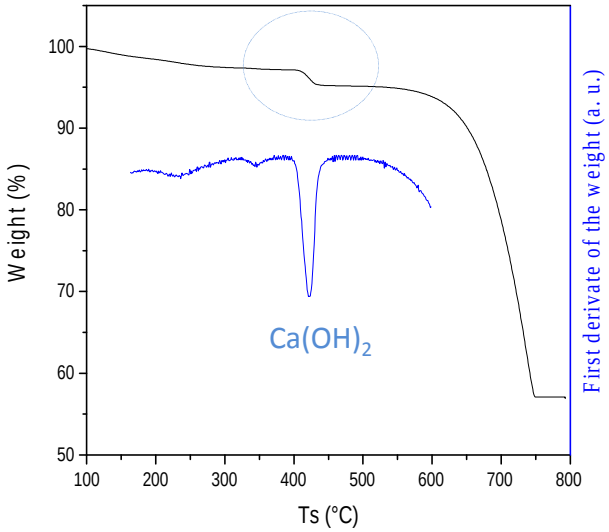


Figure 5.14. TGA (a) and first derivate of the TGA (b) analysis of the CaO NPs sample. The first derivate with the peak at 422 °C due to $Ca(OH)_2$dishydratation (2 wt%) and decarboxylation between 600 and 680 °C (37 wt%).

The first derivate of the TGA showed a calcium hydroxide phase at 422 °C, with a weight loss of 2%, and a main calcium carbonate phase with a weighting loss of 37%.

The XRD patterns of CaO NPs showed a main amorphous phase (figure 5.15), but was possible to observe bad definite peaks with a low signal/noise ratio due to calcium hydroxide phase, with the 2θ reflects at 18° and 33°, and carbonate phase with the characteristic peak at 28° for the plane (100) [17]. This was also confirmed by Fast Filter Transformation filter that help to discriminated the peak positions (figure 5.15, red line).

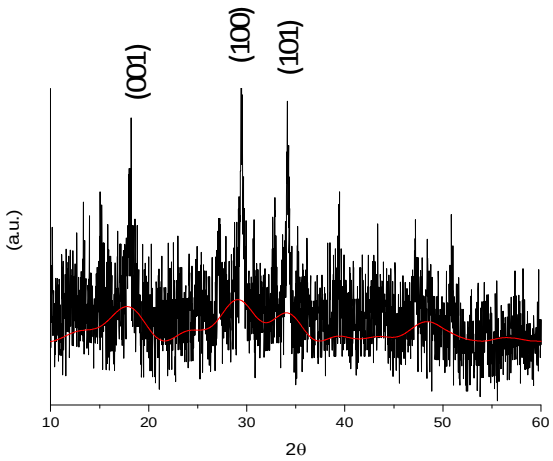


Figure 5.15. The XRD patterns of the amorphous CaO NPs sample.

### 5.5.1. Mechanical characterization of the CaO-X/IR nanocomposite

The vulcanization of the nanocomposite was obtained by the CaO NPs at different loading (Table 5.4), CaO-X/IR, where X refers to the actual amount of CaO, and the equivalent vulcanization curves was presented in figure 5.16 and compared with M-1.0CaO-IR and ZnO 0 phr.

| **Composite** | **IR** | **$SiO_2$** | **CaO NPs** |
|---|---|---|---|
| CaO-4.7/IR | 100 | 40.0 | 4,7 |
| CaO-1.4/IR | 100 | 40.0 | 1,4 |
| CaO-0.7/IR | 100 | 40.0 | 0,7 |

Table 5.4. Filler and loading of CaO NPs in Ca-4.7/IR, CaO-1.4/IR and CaO-0.7/IR.

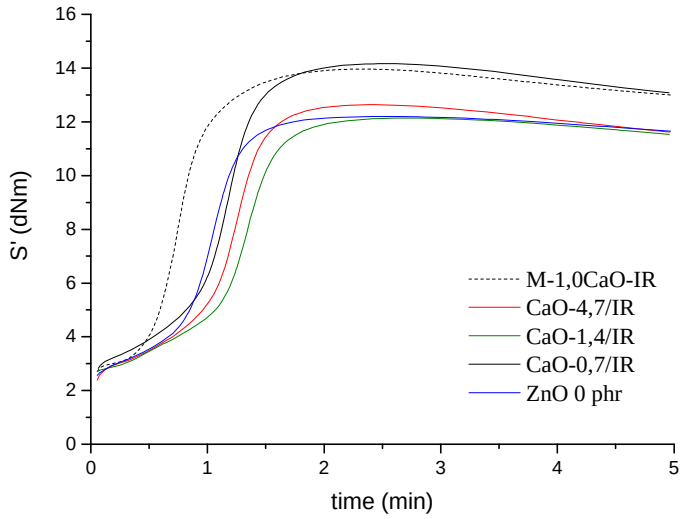


Figure 5.16. Vulcanization cures of M-1,0CaO-IR (---), CaO-4,7/IR (—) and CaO-1,4/IR (—), CaO-0,7/IR (—) and ZnO 0 phr (—).

The CaO-X/IR vulcanization curves showed, (see figure 5.16), similar $t_{MH}$ longer than M-1,0CaO-IR and MH value similar to ZnO 0 phr. Thus, also in this case the CaO NPs didn't showed an activity similar to the ZnO as curing activator.

These results were also supported by the DMA analysis, (see figure 5.17), of the cured of the CaO-X/IR that didn't given any particular enhancement in the decrease of the Tan δ valour and the loading of CaO NPs appear independent on the mechanical proprieties.

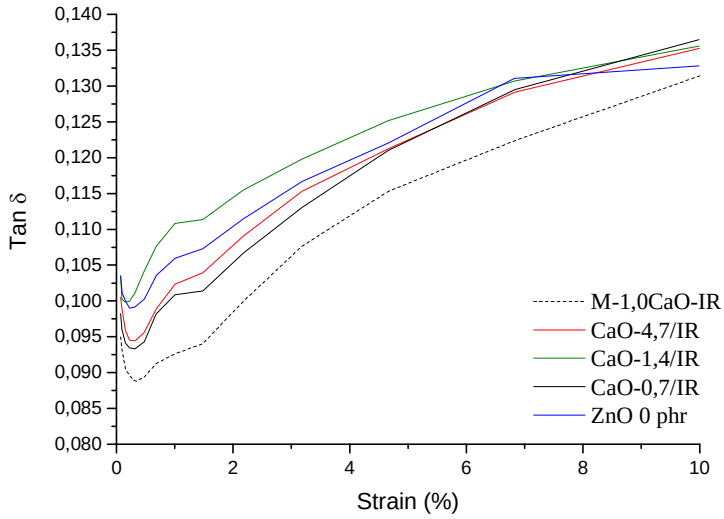


Figure 5.17. Storage modulus G' vs strain of cured of M-1,0CaO-IR (---), CaO-4,7/IR (—) and CaO-1,4/IR (—), CaO-0,7/IR (—) and ZnO 0 phr (—).

The curing of isoprene rubber by CaO NPs was inefficient and not calcium loading dependent.

## 5.6. Conclusions

The chapter reports the use of $MeO/SiO_2$ NPs (Me = Ca, Mg) and CaO NPs as curing activator in isoprene rubber. The nanoparticles have been synthesized in supersaturation condition by hot-injection approach at different loading of alkaline earth metal grown on bare silica. The amorphous $CaO/SiO_2$ NPs powder showed a main calcium carbonate (5-10 wt %) and minority calcium hydroxide phase (1-3 wt %). Similar results were obtained for single amorphous $Ca(OH)_2$ NPs with a coexistence of carbonate and hydroxide phases.

Otherwise, the amorphous MSO-8 NPs led to a single $Mg(OH)_2$ phase (5 wt %) and an amorphous structure. The Ca and Mg reacts with the surface silanol group leading to a preferential formation of Me-O-Si hetero-bond. Where CSO-X showed a partial substitution of siloxane bond with a Ca-O-Si covalent bond and incorporation of calcium atoms into the silica structure.

The nanocomposites cured with CSO-X or MSO-X were compared with a composite cured without any activator of vulcanization. CSO-X showed a faster kinetic and higher MH, at relevant loading of calcium, than curing process without vulcanization activator, but anyway without any considerable enhancement of mechanical proprieties and independent on calcium loading. Otherwise, the MSO-8 given slight improvement of the mechanicals proprieties, as proved also by the crosslinking density measurements. The low curing efficiency of CSO-X and MSO-8 were explained by their low ability to give a good crosslinking distribution, as investigated by MCV approach, that it is attributed to the low activity of the alkaline earth metals in the curing process. Similar results have been obtained for the $Ca(OH)_2$ NPs such as with low crosslinking density and, thus, inefficient mechanical proprieties of the vulcanizated composites.

[1] V. Ducháček, A. Kuta, P. Přibyl, Efficiency of metal activators of accelerated sulfur vulcanization, J. Appl. Polym. Sci. 47 (1993) 743-746.
[2] H. Irving, Irving, R.J.P. Williams, 637. The stability of transition-metal complexes, Journal of the Chemical Society (1953) 3192-3210.
[3] B.V. M. Guzman, N. Agullo, U. Giese, S. Borros, Zinc Oxide Versusus Magnesium Oxide Revisited. Part I, Rubber Chem. Technol. 85 (2012) 38-55.
[4] M.R. Crimmin, M. Arrowsmith, A.G.M. Barrett, I.J. Casely, M.S. Hill, P.A. Procopiou, Intramolecular Hydroamination of Aminoalkenes by Calcium and Magnesium Complexes: A Synthetic and Mechanistic Study, Journal of the American Chemical Society 131 (2009) 9670-9685.
[5] I. Fedushkin, A. Skatova, V. Chudakova, G. Fukin, S. Dechert, H. Schumann, Monomeric Magnesium and Calcium Complexes Containing the Bidentate, Dianionic 1,2-Bis[(2,6-diisopropylphenyl)imino]acenaphthene Ligand, European journal of inorganic chemistry 2003 (2003) 3336-3346.
[6] M.E. Jung, G. Piizzi, gem-Disubstituent Effect: Theoretical Basis and Synthetic Applications, Chemical Reviews 105 (2005) 1735-1766.
[7] M. C. Chisholm, J. Gallucci, K. Phomphrai, Lactide polymerization by well-defined calcium coordination complexes:comparisons with related magnesium and zinc chemistry, CHEM. COMMUN. (2003) 48-49.
[8] Z. Sun, W. Zhang, M. Ji, R. Hartsock, K.J. Gaffney, Aqueous Mg2+ and Ca2+ Ligand Exchange Mechanisms Identified with 2DIR Spectroscopy, The Journal of Physical Chemistry B 117 (2013) 12268-12275.
[9] M. Guzman, G. Reyes, N. Agullo, S. Borros, Synthesis of Zn/Mg Oxide Nanoparticles and Its Influence on Sulfur Vulcanization, J. Appl. Polym. Sci. 119 (2011) 2048-2057.
[10] J. E. Huheey, E. A. Keiter, R.L. Keiter, Inorganic Chemistry: Principles of Structure and Reactivity, Harper-Collins (1993).
[11] S. Chadwick, U. Englich, B. Noll, K. Ruhlandt-Senge, Syntheses and Structure Determinations of Calcium Thiolates, Inorganic Chemistry 37 (1998) 4718-4725.
[12] X. Wang, L. Altmann, J. Stöver, V. Zielasek, M. Bäumer, K. Al-Shamery, H. Borchert, J. Parisi, J. Kolny-Olesiak, Pt/Sn Intermetallic, Core/Shell and Alloy Nanoparticles: Colloidal Synthesis and Structural Control, Chemistry of Materials 25 (2013) 1400-1407.
[13] I. McCue, J. Snyder, X. Li, Q. Chen, K. Sieradzki, J. Erlebacher, Apparent Inverse Gibbs-Thomson Effect in Dealloyed Nanoporous Nanoparticles, Phys. Rev. Lett. 108 (2012).
[14] K. Bishop, K.J.M. Bishop, C. Wilmer, S. Soh, B. Grzybowski, Nanoscale Forces and Their Uses in Self-Assembly, Small 5 (2009) 1600-1630.
[15] S.G.K.a.T. Hyeon, Formation Mechanisms of Uniform Nanocrystals via Hot-Injection and Heat-Up Methods, Small 19 (2011) 2685-2702.

[16] O. Cizer, C. R. Navarro, E. R. Agudo, J. Elsen, D. V. Gemert, K.V. Balen, Phase and morphology evolution of calcium carbonate precipitated by carbonation of hydrated lime, J. Mater. Sci. 47 (2012) 6151.
[17] S. Zhang, A new nano-sized calcium hydroxide photocatalytic material for the photodegradation of organic dyes, RSC Advances 4 (2014) 15835-15840.
[18] J. Park, D. Min, H. Song, FT-IR Spectroscopic Study on Structure of CaO-SiO2 and CaO-SiO2-CaF2 Slags, ISIJ International 42 (2002) 344-351.
[19] H. Aguiar, Aguiar, J. Serra, P. González, B. León, Structural study of sol–gel silicate glasses by IR and Raman spectroscopies, Journal of non-crystalline solids 355 (2009) 475-480.
[20] J. Ma, Ma, C.Z. Chen, D.G. Wang, J.Z. Shi, Textural and structural studies of sol–gel derived SiO2–CaO–P2O5–MgO glasses by substitution of MgO for CaO, Materials science & engineering. C, Biomimetic materials, sensors and systems 30 (2010) 886-890.

# Chapter 6

# Conclusions

In the present study a novel approach is reported, aimed at improving the efficiency of the rubber curing. It employs ZnO NPs anchored to silica filler nanoparticles, which simultaneously behave as curing agent and rubber reinforcing, significantly reducing the amount of the used ZnO activator.

ZSO-X NPs were prepared by hydrolysis and condensation of $Zn(CH_3COO)_2$ in ethanol solution of NaOH in the presence of $SiO_2$ particles, using very small amounts of the zinc precursor. By this way the hydrolyzed zinc species $Zn(OH)_n^{2-n}$ interact with the silanol groups at the surface of silica particles through Si-O-Zn bonds and induce the growth of ZnO NPs.

In particular, at lower loading of Zn precursor (<14%), ZnO particles have amorphous structure. This property guarantees an easier release of $Zn^{2+}$ ions than in crystalline ZnO NPs, favoring the reaction with stearic acid and the successive formation of the sulfuring zinc complex along the curing process. Moreover, the immobilization of ZnO NPs on the silica surface, due to the covalent Si-O-Zn bond, minimizes the Zn leaching, provides a homogeneous dispersion of zinc and increases the accessibility of curing reactants to $Zn^{2+}$ ions. On the contrary, at higher Zn precursor content the hydrolyzed $Zn(OH)_n^{2-n}$ units further condense giving larger and crystalline ZnO particles anchored to the silica surface, whose activity in curing is lower than that of the amorphous ones.

The catalytic activity of silica anchored ZnO, $ZnO/SiO_2$, as curing activator in the sulphur crosslinking of IR was investigated in comparison to that of conventional microcrystalline C-ZnO.

.

The high curing efficiency of $ZnO/SiO_2$ was explained by its ability to form sulfurating complexes at the beginning of reaction and the sulfur network in the final cured material. In fact, the values of the apparent activation energy $E_\alpha$ of the different steps of the vulcanization process, evaluated from differential thermal analysis measurements, demonstrated that in the induction period of curing the reaction of ZnO with the stearic acid and the successive reactions with the other curatives are kinetically favoured in the presence of $ZnO/SiO_2$ compared to C-ZnO.

Regarding the sulphur network formation, investigated by a MCV approach, short crosslinking sulfide chains are mainly obtained in the presence of $ZnO/SiO_2$ unlike with C-ZnO which gives longer polysulfide chains ($S_5$, $S_6$, $S_8$). This explains the higher crosslinking density, calculated by the Flory-Rehner equation, in the XZSO-IR composites and their better curing efficiency. Moreover, the highest $E_\alpha$ in the last step of curing, evidences that further reactions of the crosslinked rubber are more difficult in XZSO-IR than in YZnO-IR, probably due to the larger amount of more stable mono- and di-sulfide crosslinking chains.

FTIR analysis suggests that ZSO-7.7 NPs promote the formation of a stearate bridged bidentate zinc complex $(Zn_2(\mu\text{-}O_2CC_{17}H_{35})_2)^{2+}.4Y$ in the first step of the curing reaction. In the presence of C-ZnO only the distearate zinc complex was detected. The formation of $(Zn_2(\mu\text{-}O_2CC_{17}H_{35})_2)^{2+}.4Y$ in the presence of $ZnO/SiO_2$ was associated to the constraint of tetrahedral geometry around the Zn bound to silica. This species is highly reactive towards CBS and sulphur and seems to be play a key role in accelerating the cross-linking reaction.

Amorphous ZnO NPs anchored on the silica demonstrated better curing efficiency and improved dynamic mechanical properties in cured silica/rubber nanocomposites, compared to those obtained by using

higher amount of microcrystalline ZnO. These results suggest the proposed material could be considered as a promising system for the improvement of the curing efficacy and for the effective decrease of ZnO utilization in rubber compounding.

The use of $MeO/SiO_2$ NPs (Me = Ca, Mg) as curing activator in isoprene rubber was also investigated. $MeO/SiO_2$ NPs have been synthesized by hot-injection approach, in supersaturation condition, at different loading of alkaline earth metal particles anchored on silica. $CaO/SiO_2$ particles demonstrated similar curing efficiency and dynamic mechanical properties in cured silica/rubber nanocomposites, compared to those obtained without any kind of curing activator. The $MgO/SiO_2$ showed slight enhancement of the mechanical proprieties of the composite. This may be explain to the low activity of the alkaline earth metals in the curing process and carbonate phases present in the particles synthesized.

# Appendix A

# Characterization and Methods

The aim of this appendix is make a point about the synthesis of silica and to explain the methods of characterization and investigation employed in this work.

In the appendix are presented in a first part the spectroscopies and thermoanalyticals techniques of analysis of the double fillers function, the composite such as and of the model compound, thus it will explain the models used and the last part is dedicate to physic-mechanical proprieties of the composite.

### A.1.1. Silica synthesis, state of art

The silica nanoparticles is one of the most used filler for nanocomposite, it is produced with clean methods that offer an effective advantage respect the other filler such as the carbon black, that it is produced by furnaces that burn aromatic oil at high temperature.

The silica production comes from pyrogenic process to obtain the fumed silica, through the following reaction:

$$SiCl_4 + H_2 + O_2 \rightarrow SiO_2 + 4HCl$$

The silica used in the tyre has a high specific area and highly structured, it come from a series of precipitation reaction started from quartz sand:

$$SiO_2 \text{ (quartz)} + Na_2CO_3 \rightarrow (>1200\ °C, \text{melting})\ Na_2O{\cdot}SiO_2 + CO_2$$

$$Na_2O{\cdot}SiO_2 + H_2SO_4 \rightarrow SiO_2 + H_2O + Na_2SO_3$$

The process combined the quartz sand with sodium carbonate at 1500 °C to obtain amorphous $Na_2O{\cdot}SiO_2$ so called "cullet", the sodium silcate was dissolved in water at 150°C (pH ≈ 12), then the solution was mixed with

sulfuric acid so to obtain an suspension with a pH between 6 and 12 and 90 - 95 % of water, the solution was filter through a membrane so to obtain a silica cake (70 - 85 % of water). The last step was the important process of drying, the silica cake can be by spray dryer, spin flesh dryer or plate dryer to obtain a silica powder (1 - 100µm), the silica can compacted and crushed to have the granulated silica (500µm - a few mm), while the micro-pearls silica (50 - 300µm) was obtained by spry nozzle dryer.

The silica used in tyre industry is constitute by primary particles intra-linking chemical bound to give wide structure, the aggregate with size around sub-µm, which in turn they can interact to one each anther via hydrogen-bridge so called agglomerate.

The precipitation time and the drying process of silica are the parameters that define the silica structure, long precipitation time facilitate the aggregate growth and agglomeration domain. The aggregation of the particles will influence also the mechanical proprieties.

### A.2.1. Inductively Coupled Plasma (ICP)

The ICP analysis was used to determinate the amount of metal oxide (ZnO, CaO and MgO) present in the sample. The instrument used was the ICP-OES Optima 7000 DV Perkin Elmer.

The plasma source, constituted by a gas mixture electric conductor, has a charge close to zero. Inside the quartz tube there is a constant flux of argon between of 20 L/min that transport the sample vaporized.

In figure A.1. was represented the extremity of the torch is present a coil generating radiofrequency (40 MHz) that produce the ionization of the Argon with the production of a plasma at a temperature 8000 K.

The source exciting the electrons of the sample that emitted a characteristic wave detected by a CCD (Charged Coupled Device) camera, the detector measure the intensity of the radiation and was converted in electric signal by a photomoltiplicator.

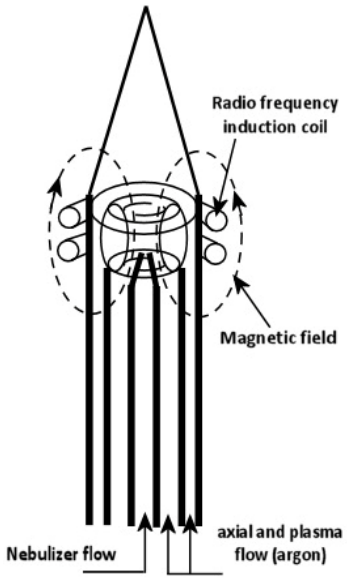


Figure A.1. Torch of the ICP (plasma source)

Specimens for the analysis were prepared by thinly grinding, 0.2 g of powdered samples and dissolving them in a Teflon beaker with 5 mL of HF 49%. Then the solution was dried and the residue rinsed five times with 3 mL of HCl 37%. Finally, the obtained solution was dried again, and the solid dissolved with MQ water and diluted in a 250 mL calibrated flask. Before analysis a further dilution 1:100 was carried out

### A.2.2. High-Resolution Transmission Electron Microscopy (HRTEM)

The High-Resolution Transmission Electron Microscopy (HRTEM) apparatus has a magnification of $10^6$ X.

The HRTEM (figure A.2.) is constituted by an electron beam source (Electron Gun) accelerated through a potential difference, their reaching a velocity comparable to the speed of light (up to 100KeV), thus the electron beam went through a pane wave and then they collided on the sample (specimen) and further an objective lens that operate a Fourier transform of the data, which they were converted by diffraction pattern into a 2D image by an inverse Fourier transform.

The TEM used in work is an Jeol 3010 High Resolution Transmission Electron Microscope operating at 300 kV with a high-resolution pole piece (0.17 nm point to point resolution) and equipped with a Gatan slow-scan 794 CCD camera.

The powders were suspended in isopropanol, and a 5 µL drop of this suspension was deposited on a holey carbon film supported on 3 mm copper grid for TEM investigation.

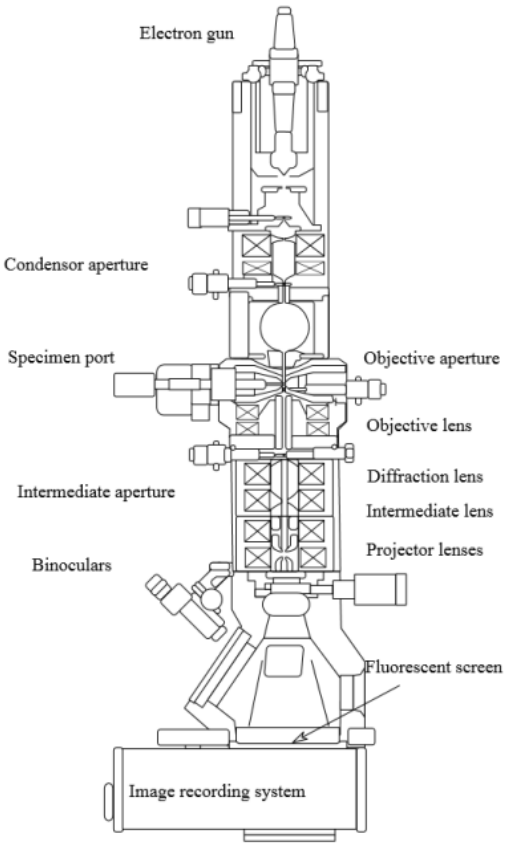


Figure A.2. High-Resolution Transmission Electron Microscopy (HRTEM) apparatus

### A.2.3. X-ray Diffraction (XRD)

The XRD technique is based on elastic scattering phenomena of a X-ray radiation collider an electronic shell of the atoms.

The atoms that constitute the materials are scattering centers, where the incident beam was scattered is special distributed in a regular way (if the sample is crystalline) with a wavelength of same energy of the wavelength incident ($\lambda$).

The analysis was performed by a Bruker D8 ADVANCE diffractometer, with an angular accuracy of 0.001° and an angular resolution lower than

0.01°. The incident radiation was CuKα, with a wavelength of 1.5406 Å. The diffratogram was scanning in Bragg-Brentano geometry, range 15°-50°, step of 0.03° and 7 second as time of acquisition for each step.

### A.2.4. Reflectance UV–Visible analysis

Reflectance UV–Visible analysis (range 400–200 nm) with an accuracy 0.08 nm was performed by a UV Lambda 900 Perkin Elmer spectrometer on powdered samples to determine the absorption edge energy of ZnO.

The light beam constituted by two radiation sources, a deuterium lamp and a halogen lamp, that in turn was reflected by a series of mirrors and monochromators to reach the sample fixed within a holder with a quartz window where the incident beam collider and then reflected to the detector that converted the signal in a current signal by photomoltiplicator.

The diffuse reflectance spectra obtained from the powdered nanostructures transformed using the Kubelka-Munk treatment, in accord with equation (1), so it was possible to extract their Eg unambiguously.

$$F(R) = \frac{(1-R)^2}{2R} \qquad (1)$$

The absorption onset can be obtained by plotting $\ln^2(I_t/I_0)$ vs. energy [1].

### A.2.5. Attenuated Total Reflectance Fourier Transform Infrafed Spectroscopy (ATR-FTIR)

The ATR-FTIR measurements were made in a part of Mid-Infrared range (400-4000 $cm^{-1}$, λ 25 – 2.5 μm) then in the range of Intramolecular fundamental vibration.

The ATR-FTIR was used in order to investigate the functional group of the molecules by vibrational spectroscopy.

The absorption of infrared radiation at different wavelengths is associated with the active IR vibrational modes of different bonds, so different chemical species have characteristics infrared absorption spectra.

The intensity of the absorption bands of a IR spectra depend of the being of the electric dipole moment produced by specific vibration involved in the absorbent process and then it is proportional to the amount of functional group detects.

Because of the difficulties of infrared light penetration in solid samples, the ATR device is used, and the radiation that comes to the detector is not transmitted through a bulky sample, but is many times reflected on it thanks to the ATR crystal (figure A.3). This contact is sufficient to allow absorption of IR radiation. The apparatus is made of: a sample holder that is pressurized by a steel piston (in order to maximize the contact area with the radiation), the ATR crystal, a source of IR radiation, and a detector. Since the radiation is passing through an interferometer before reaching the sample, Fourier Transform is applied to the detected signal in order to obtain a transmittance against wavelength spectrum from the interferogram.

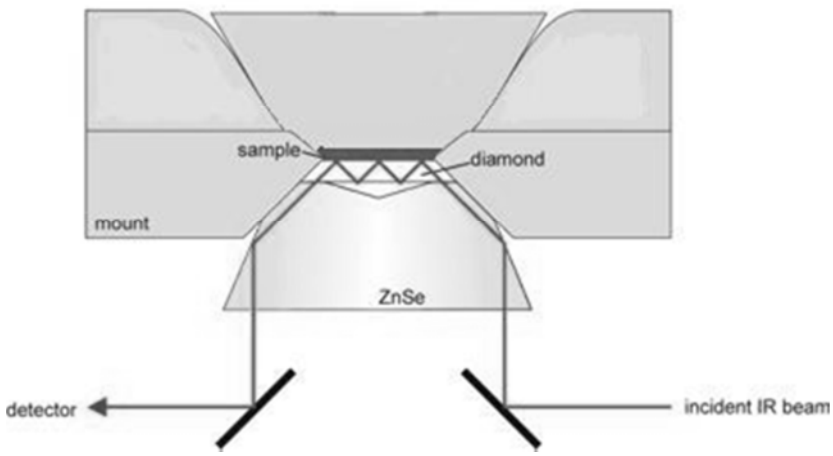


Figure A.3. Simple holder of the IR spectrometer apparatus structure.

The analysis was performed with a Perkin Elmer Spectrum 100 instrument by a single reflection Attenuated Total Reflection (ATR) method (1 $cm^{-1}$ resolution spectra, 650-4000 $cm^{-1}$ region, 16 scans).
The spectra were then analyzed further under subsequent actions of data Tune-up, ATR correction and Based line correction and finally Normalization modes for obtained the spectra presented in this thesis.

**A.2.6. Nuclear Magnetic Resonance (NMR)**

Solid state NMR analyses were carried out with a Bruker 400WB spectrometer operating at a proton frequency of 400.13 MHz and for the Model Compound Vulcanization liquid samples were used a NMR 500 MHz Bruker Avance wide bore.
Magic-Angle Spinning-NMR (MAS NMR) spectra were acquired with single pulse (SP) experiments and cross polarization (CP) pulse sequences under the following conditions. CP: $^{29}Si$ frequency: 79.48 MHz, p/2 pulse 3.9 µs, decoupling length 6.3 µs, recycle delay: 10 s, 5 k

scans. SP: p/4 pulse 3.9 µs, recycle delay 100 s, 2 k scans. Samples were packed in 4 mm zirconia rotors, which were spun at 6 kHz under air flow. Adamantane, Q8M8 and EtOH were used as external secondary references. Si units were labeled according to the usual NMR notation, $Q_n$ representing a tetrafunctional Si unit within bridging O atoms.

Solid state $^{29}Si$ SP MAS, $^{29}Si$ CP MAS and $^{1}H$ MAS NMR investigations were performed on ZSO-X samples.

The MCV samples was analyzed by $^{1}H$ NMR spectra were recorded at 500 MHz on samples dissolved in $CHCl_3$ (1:10 vol:vol). Chemical shifts were determined relative to the residual solvent peak ($CHCl_3$, δ 7.26 ppm).

### A.2.7. X-ray Photoelectron Spectroscopy (XPS)

The X-ray Photoelectron Spectroscopy, also known as Electron Spectroscopy for Chemical Analysis (ESCA), is a technique based on kinetic analysis of the photoelectron emitted by the superficial layer of a sample for irradiation by X-ray, the sample was fix in Ultra High Vacuum ($p \leq 10^{-7}$ Pa).

By this technique is possible to analysis on the atomic rate in function of depth and the chemical distribution of the sample surface.

The analysis in depth was made by sputtering, where the sample's layer was bombard by $Ar^+$ beam at low energy (≤ 3 KeV), then analyzed the peaks intensity at every wearing cycle.

It is possible to obtain a trend of the atomic rate in function of time and wearing cycles, at the same time correlate with the depth.

In this work the analysis was carried on by a Perkin-Elmer Φ 5600-ci spectrometer using non-monochromatized source at Al-Mg double anode.

Samples were mounted on steel holders and introduced directly into the fast-entry lock system of the XPS analytical chamber.

The analysis area was 800 μm in diameter and the working pressure was lower than 10–9 mbar. The spectrometer was calibrated by assuming the binding energy (BE) of the Au 4f7/2 line at 83.9 eV with respect to the Fermi level. The standard deviation for the BEs values was ±0.2 eV.

In the acquisition of data was used a standard source (Al Kα) with an energy of 1486.6 eV. It was acquired both survey scans were obtained in the 0-1350 eV range and detailed multiplex scans were recorded for the C1s, O1s, Na1s, Si2p and Zn2p regions. No further element was detected. Charging effects were corrected by assigning to the C1s peak associated with adventitious hydrocarbons a value of 284.8 eV [2]. The analysis involved Shirley-type background subtraction [3] non-linear least-squares curve fitting adopting Gaussian–Lorentzian peak shapes, and peak area determination by integration. The atomic compositions were evaluated from peak areas using sensitivity factors supplied by Perkin-Elmer, taking into account the geometric configuration of the apparatus. The experimental error on the reported atomic composition values did not exceed ±5%.

### A.2.8. Thermogravimetirc analysis (TGA)

The TGA analysis was performed to detect the amount of carbonate and hydroxide phase present in the alkaline earth matelas oxide in the chapter V. The instrument used was a TGA/DSC1 STARe SYSTEM (Mettler Toledo) at constant nitrogen flow (50 $cm^3$ $min^{-1}$). The temperature range of analysis was between 25-1100 °C and sample holder used was a pan of alumina with 75 μL of volume, the measurements were performed without lid.

The thermogravimetirc analysis permitted to analyze the sample weight loss by thermo-scale in function of the heating.

The thermogravimetirc curve is possible to observe the change in simple weight with inert atmospheric pressure as result of decomposition reactions, oxidation and physical process as vaporization and desorption.

In order to register the temperature inside the furnace is present a thermocouple, that offer the possibility to operate a different temperature rate and at isothermic condition.

### A.2.9. Apparent Activation Energy of curing process from Differential Thermal Analysis

The curing process for the IR compound was studied by kinetic approaches using the Differential Scanning Calorimetric (DSC) analysis performed on a DSC Mettler Toledo Stare Thermal Analysis System equipped with a $N_2$ cooling apparatus, at different heating rates: 5, 10 and 20 °C/min. In particular, the apparent activation energy $E_\alpha$ of the different steps of vulcanization was evaluated from the exothermic curing peak of the DSC thermograms (figure A.4. a.) according to the method developed by Kissinger [4] and the kinetic model proposed by Vyazovkin [5].

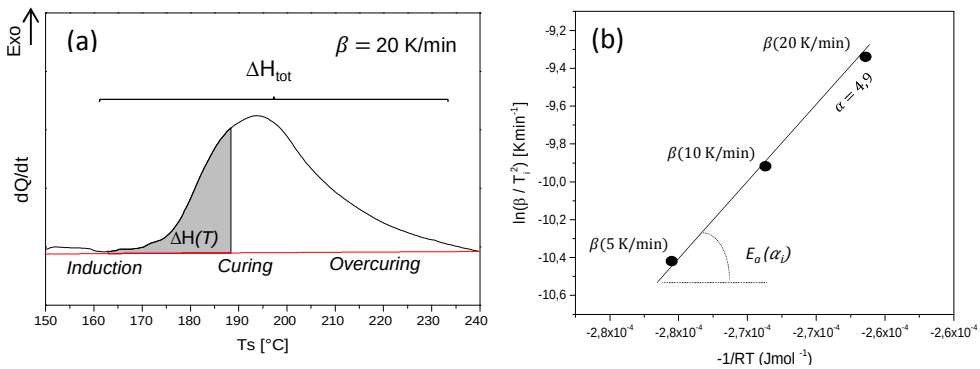

Figure A.4 a) Exothermic curing peak from DSC thermogram; b) Plot of ln $\beta/T_i^2$ *vs* $1/T_i$ for a selected value of conversion degree α; heating rates β and activation energy $E_\alpha$ calculated as slope are also indicated. (Examples related to sample 1.85 ZSO-IR).

The model is based on the assumptions that i) $E_\alpha$ depends on the conversion degree (α) of the reaction; ii) at fixed value of α, $E_\alpha$ is the same whatever the used heating rate (β).

According to this model, the value of α is:

$$\alpha = \frac{\Delta H(T)}{\Delta H_{tot}} \qquad (3)$$

Where *ΔH(T)* is the integral of the exothermic peak from the starting vulcanization temperature $T_o$ to the temperature T and $\Delta H_{tot}$ is the integral of the total vulcanization peak (figure 3.1. a). The kinetic equation of the vulcanization process is:

$$\frac{d\alpha}{dt} = k(T)f(\alpha) \qquad (4)$$

where *k(T)* is the constant rate and *f(α)* depends on the reaction mechanism. As β = dT/dt, equation (4) can be rewritten at constant β as:

$$\frac{d\alpha}{dT} = \beta^{-1}k(T)f(\alpha) \qquad (5)$$

Substituting *k(T)* in (5) according to the Arrhenius equation (A is the pre-exponential factor, R the gas constant) and integrating over T:

$$g(\alpha) = A\beta^{-1}\int_{T_0}^{T} e^{\left(-\frac{E_a}{RT}\right)}dT \qquad (6)$$

Where g(α)= $\int_0^\alpha d\alpha/f(\alpha)$.

Solving the integral (6) [6] at fixed values of α (iso-convertional or free-kinetics model [5, 7]), the following equation is obtained

$$ln\frac{\beta}{T^2} = ln\frac{RA}{E_a} - \frac{E_a}{RT} \qquad (7)$$

According to equation (7), for each value of α, the linear plot of ln ($\beta/T^2$) *vs* 1/T enables $E_\alpha$ to be determined from the slope (figure 3.1. b).

**A.2.10. The Liquid Chromatography-Mass Spectroscopy (LC/MS)**

The Liquid Chromatography-Mass Spectroscopy (LC/MS) technique combines the Liquid Chromatography, used to separate the reaction products, and the Mass Spectroscopy, used for the identification of the substance in an analytic. The LC/MS is used to investigate multiple reactions in several organic/inorganic systems permitting to detect the amount of different products in function of reaction time, This technique has obtained a large success in the composites materials field in particularly on the investigation of the vulcanization mechanism, both by sulfur and via epoxy group, and silanization process, this is due to the possibility to create low-molecular-weight model as substitutes for the polymeric rubber (insoluble) so to obtain the so called Model Compound Vulcanization (MCV).

LC/MS experiments were performed on a Bruker Daltonics LC-MS equipped with an Atmospheric Pressure Chemical Ionization (APCI) apparatus and a Nucleosil 100-5 C18 HD (reverse phase) column. Reaction products were diluted with acetonitrile (1:10 vol:vol) for the analysis. The experimental conditions were: mobile phase, acetronitrile (97%) and water (3%); flow rate 0.3 ml/min.

### A.3.1. Model compound vulcanization

The Model Compound Vulcanization (MCV) experiments were performed by curing tetramethylethylene (TME) as model compound in the presence of 18.5 phr of ZSO-7.7, corresponding to 1.85 phr of ZnO (sample ZSO-TME) or of 1.85 phr C-ZnO powder (sample C-ZnO-TME). The amounts of the other curatives are: 2 phr stearic acid, 1.6 phr CBS, 3 phr sulphur. CBS was purified by re-precipitation after solving it in acetone solution at 40°C.

Curing reactions were performed in a 5 ml closed conical vial, heated in an oil bath at 120 °C for different times (5, 15, 20, 30, 40 and 60 min). After the reaction, the vial was cooled down in a liquid nitrogen bath and the reaction mixture was filtered several time by using a 2 µm porous filter.

### A.4.1. Swelling experiments

Swelling experiments were performed on composites sample to evaluate the cross-linking degree after the vulcanization, thus has an estimation of network structure and ultimate mechanical proprieties of the cured materials.

Samples of 10 x 10 x 2 $mm^3$ (0.20 ± 0.02 g) were immersed in close vessels filled with 10 mL of toluene at 25 °C for three days in the dark to avoid photodegradation reactions. Toluene was replaced daily with fresh solvent to eliminate all the extracted fractions. Finally, the swollen mass was weighted and dried to constant mass in vacuum at 70°C for 12 h. The volumetric fraction of the swelled rubber $V_r$ was calculated according to the following equation [8]:

$$V_r = \frac{(m_d - f m_0)\cdot \rho_p^{-1}}{(m_d - f m_0)\cdot \rho_p^{-1} + m_{so}\cdot \rho_s^{-1}} \qquad (1)$$

where $m_0$ is the weight of the composite before swelling; $m_d$ the weight of the dried mass after swelling; $m_{so} = (m_{sw} - m_d)$ the weight of the solvent in the swollen mass; $m_{sw}$ the weight of the swollen mass; $\rho_p = 0.94$ g•cm$^{-3}$ is the IR density; $\rho_s = 0.87$ g•cm$^{-3}$ is the toluene density; $f$ is the fraction of the filler in the composites as determined by TGA. The cross-link density $v$, the number of network chains per gram bounded on both ends by crosslinks, was calculated according the Flory-Rehner equation [9];

$$v = \frac{[\ln(1 - V_r) + V_r + \chi V_r^2]}{-2\cdot \rho_p \cdot V_s \cdot (V_r)^{1/3}} \qquad (2)$$

where $V_s$=105.91 is the molar volume of toluene and $\chi$ is the Flory solvent-polymer interaction term [10], which is 0.43 for toluene-IR [11].

### A.4.2. Moving Die Rheometry (MDR) and curing kinetics

Rheological measurements are the main techniques to evaluate dynamo-mechanical performances of rubber nanocomposites. This measure is make *insitu* during the vucanization process, so to see the formation of chemical crosslinks in function of time at given temperature.

In particular, a moving die rheometers oscillating at a constant frequency and strain amplitude. The crude material is placed all around the die, and the whole system is enclosed in a pressurized thermostated chamber, as represented schematically in figure A.5. (b).

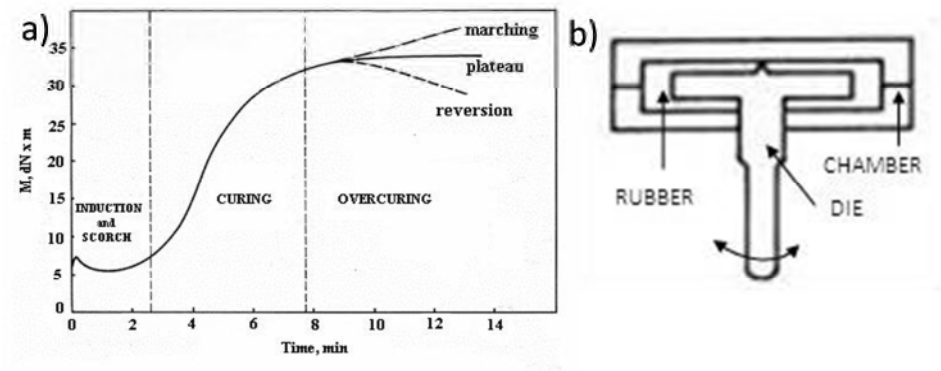


Figure A.5. a) vulcanization curve profile b) representation of rheometer chamber.

Upon heating at a chosen vulcanization temperature, the vulcanization process starts, and it can be followed by the increase of the torque acting on the moving die, which is a consequence of the increase of elasticity that is occurring in the material. A typical curve of a vulcanizing system is reported in figure A.5. (a): in the first part (induction), we observe a materials softening due to the heating, and a subsequent increase (also referred to as scorch) due to the starting of the vulcanization reaction; in a second time, the curve increase rapidly, as a consequence of the curing reaction, reaching a plateau, corresponding to the end of the vulcanization. Overheating may cause a reversion of the vulcanization process, represented by the third part of the curve that is deleterious for the final material properties. The main result from the curve is the optimal curing time at which the material can be completely vulcanized avoiding overcuring reaction to take place.

Dynamic mechanical characterization of the composites were performed by Rubber Process Analyzer (RPA2000, Alpha Technologies) under the following conditions for the curing profiles: ± 1° oscillation angle, 170°C temperature, 4.3 bar pressure and 5 min running time.

The strain sweep tests were carried out at 70 °C and 10 Hz and 10 min running time. Specimens were cut by using a Constant Volume Rubber Sample Cutter (CUTTER 2000, Alpha Technologies); the dimensions were 3.5 cm diameter and ≈ 0.2 cm thick; the weight 4.5 ± 0.3 g. Two measurements were carried out for each sample, and the average value was reported.

---


[1] R.T. S. Monticone, A. V. Kanaev, Complex Nature of the UV and Visible Fluorescience of Colloidal ZnO Nanoparticles, J. Phys. Chem. B 102 (1998) 2854-2862.

[2] D. Briggs, M. Seah, Practical Surface Analysis, Wiley, Chichester (1990).

[3] D.A. Shirley, High-Resolution X-Ray Photoemission Spectrum of the Valence Bands of Gold, Physical Review B 5 (1972) 4709-4714.

[4] H.E. Kissinger, Reaction Kinetic in Differencial Thermal Analysis, Anal. Chem. 29 (1957) 1702-1705.

[5] S.V. Vyazokin, V.I. Goryachko, A.I. Lesnikovich, An approach to the solution of the inverse kinetic problem in the case of complex processes: Part III Parallel indipendent reactions, Thermochim. Acta 197 (1992) 41-45.

[6] B.V. M. Guzman, N. Agullo, U. Giese, S. Borros, Zinc Oxide Versusus Magnesium Oxide Revisited. Part I, Rubber Chem. Technol. 85 (2012) 38-55.

[7] J. Flynn, L. Wall, General treatment of the thermogravimetry of polymers, J. Res. Nat. Bur. Stand.. Section A. Physics and chemistry 70 (1966) 487-523.

[8] B.W. Ellis, G. N., Estimation, from Swelling, of the Structural Contribution of Chemical Reactions to the Vulcanization of Natural Rubber.Part II. Estimation of Equilibrium Degree of Swelling, Rubber Chem. Technol. 37 (1964) 571-575.

[9] P.J. Flory, J. Rehner, Statistical Mechanics of Cross–Linked Polymer Networks II. Swelling., J. Chem. Phys. 11 (1943) 521-526.

[10] P.J. Flory, J. Rehner, Thermodynamics of High Polymer Solutions, J. Chem. Phys. 10 (1942) 51-61.

[11] R. Orwoll, P. Arnold, Polymer–Solvent Interaction Parameter χ, in: J. Mark (Ed.) Physical Properties of Polymers Handbook, Springer New York 2007, pp. 233-257.